Democratic and Popular Republic of Algeria
Ministry of Higher Education and Scientific Research
Echahid Cheikh Larbi Tebessi University,Tebessa
Faculty of Exact Sciences and Sciences of Life and Nature
Department of Matter Sciences

MASTER'S THESIS
Field: Matter Sciences
Discipline: Physics
Option: Condensed Matter Physics

Theme:

Investigating the Impact of Strained Graphene on Hydrogen Storage Capability

Presented by:

Ali Grib

Board of Examiners:

Chair:	Mohamed Amine TAG	**MCA**	TebessaUniversity
Supervisor:	Abid BOUDIAR	**MCA**	TebessaUniversity
Examiner:	Izzeddine SAOUANE	**MCB**	Tebessa University

Date : 15/06/2023

Note: ..... **Mention: .....**

Dedication

I would like to dedicate this master's thesis to my loving family, whose unwavering support and encouragement have been the foundation of my academic journey. Their constant belief in my abilities and their sacrifices have made it possible for me to pursue this endeavor. This achievement is as much theirs as it is mine, and I am forever grateful for their love and encouragement.

I extend my deepest gratitude to my esteemed professors, whose guidance, expertise, and mentorship have been invaluable throughout the course of my research. Their dedication to teaching and their commitment to pushing the boundaries of knowledge have inspired me to strive for excellence. I am thankful for their patience, insightful feedback, and unwavering belief in my potential.

To my colleagues and friends, thank you for the countless hours of stimulating discussions, collaboration, and mutual support. Your friendship and camaraderie have provided me with the motivation and resilience to overcome challenges and grow both personally and professionally. I am grateful for the shared experiences, laughter, and encouragement that have made this journey memorable and enjoyable.

Lastly, I want to express my appreciation to all the participants who generously contributed their time and insights to this study. Without their cooperation and willingness to participate, this research would not have been possible.

To my family, professors, colleagues, and all those who have supported me along this path, I offer my heartfelt thanks. Your belief in me and your unwavering support have been instrumental in making this master's thesis a reality. I am truly fortunate to have you in my life.

Content

Chapter 2 :Hydrogen storage in strained Graphene

Chapter 3 :Simulation and calculation of hydrogen storage in strained graphene.

List of tables

List of figures

Figure(8.1)	shows the energy spectrum of graphene obtained from equation (1.15), as well as the energy spectrum for low energies near the Dirac point obtained from equation (1.16). The conductivity of graphene is quantized, and the minimum conductivity value, denoted by σ_{min}, is equal to $4e^2/h$ at the Dirac point [39]. This quantization arises from the confinement of electrons in a two-dimensional system [40]. In graphene, electrons behave as Dirac fermions with a 1/2 spin and effectively zero mass, resulting in high carrier mobility μ. Further details regarding the mobility of charge carriers in graphene are discussed in the section on Graphene Transistors [126].	15
Figure(9.1)	(a) Schematic of a graphene sealed microchamber.(Inset) optic image of a single infinitesimal subcaste graphene drumhead on 440 nm of SiO_2. The confines of the microchamber are4.75 x4.75 μm x 380 nm.(b) Side view schematic of the graphene sealed microchamber.(c) Tapping mode infinitesimal force microscope(AFM) image of a 9 nm thick numerous subcaste graphene drumhead with $\Delta p > 0$. The confines of the square microchamber are4.75 x4.75 μm. The upward deviation at the center of the membrane is 90 nm.(d) AFM image of the graphene sealed microchamber with Δ p-93 kPa across it. The minimal dip in the z direction is 175 nm.(e) AFM line traces taken through the center of the graphene membrane of(a). The images were taken continuously over a span of71.3 h and in ambient conditions.(Inset) deviation at the center of the graphene membrane vs time. The first deviation dimension(z) 175 nm is taken 40 min after removing the microchamber from vacuum. From Ref.[65].	19
Figure(10.1)	illustrates the formation of strong pseudo-magnetic fields in largely strained graphene. Panel (a) shows the Raman spectra of unstrained (black) and strained (red) graphene. The symbols in the figure represent dimension data, while the angles represent fitting data. The inset in panel (a) presents the two-dimensional Raman mapping data, plotting the 2D peak frequency of a simulated graphene nanopillar array with dimensions of 3 × 2. (b) displays the topographic image of a reconstructed strained graphene nanopillar array, specifically a 3 × 1 configuration. The top panel of this image corresponds to the topographic profile, where the brightest and darkest regions indicate heights of 300 nm and 0 nm, respectively. The middle and bottom panels represent the original strain distributions along the x-direction (ϵ_{xx}) and y-direction (ϵ_{yy}), respectively. It is observed that the strain along ϵ_{yy} is almost absent, while ϵ_{xx} exhibits maximum strain, indicating a predominant uniaxial strain in the strained graphene nanopillar.(c), a sampling of the strain profile is shown, demonstrating the original infinitesimal strain for ϵ_{xx} (black solid line) and ϵ_{yy} (red dashed line). Additionally, a sophisticated strain distribution (blue solid line) is depicted, obtained through convolution techniques. This realistic strain distribution takes into account the diffraction-limited laser spot size and is deduced from atomic-scale simulations.(d) presents the distribution of pseudo-magnetic fields in the simulated graphene nanopillar array [127]. The pseudo-magnetic fields exhibit significant magnitudes, reaching approximately 100 T, particularly near the sharp edges and corners where the deformation and strain	22

List of symbols

2D Two-dimensional Raman mapping data plotting

2d Two-dimensional

a_0 is the nearest carbon–carbon bond length (~0.14 nm)

a_1,a_2 and a_3 are the bond vectors

AFM Atomic force microscopy

B_S The spatial distribution of the pseudo-magnetic fields

BZ Brillouin zone

^oC Celsius

CcH2 cryogenically compressed hydrogen

CDG chemically derived graphene

CGH2 compressed gaseous hydrogen

CNT Carbon nanotube

CO Carbon monoxide

CO_2 Carbon dioxide

CVD Chemical vapour deposition

d is the depth of the microchamber

DFT Density Functional Theory

DLC Diamond-like carbon

DOE-US Department of Energy the United States

FET Field effect transistor

GO Graphene oxide

HOPG highly-oriented pyrolytic graphite

IUPAC International Union of Pure and Applied Chemistry

k the wave vector,

K Kelvin

k_x is the x component of the wave vector k

k_y is the y component of the wave vector k

L_0, original length

L_x and L_y are half the diagonal lengths ofprimitive cells

MEP minimum energy path

MLI multi-layer insulation

R is the universal gas constant (i.e. 8.314 J mol−1 K−1) and

RGO Reduced graphene oxide

SEM scanning electron microscope

SiC Silicon carbide

STM Scanning tunnelling microscopy

STP standard temperature and pressure (i.e. 1 bar and 273 K)

STS scanning tunneling spectroscopy

TB tight-binding

TFT thin film transistor

V is the volume

wt.% weight percentage

x, y and z the coordinates

μ. the mobility of charge carriers in graphene

ħ is the reduced Planck constant

β pseudo-magnetic field

γ is the shear strain

$\Delta k'_{Fx}$ and $\Delta k'_{Fy}$ are the corresponding components of $\Delta k'_F$

θ is the angle between the x-axis and the zigzag direction

υ is Poisson's ratio

$\nu_F \approx 10^6$ m/s the Fermi velocity of electrons in graphene.

$\rho(r)$ the electron density

ρ_H is the constant bulk density of H_2

σ Electrical conductivity

$\sigma_{min} = 4e^2/h$ the minimal conductivity at the Dirac point

$\vartheta_{XC}[\rho]$ The XC potential

ϵ is a 2×2 strain tensor

ϵ_{xx} middle panel

ϵ_{yy} bottom panel

ε_A is the corresponding uniaxial strains along the chair direction

ε_y is the uniaxial strain along the y-direction,

ε_Z is corresponding uniaxial strains along the zigzag direction

Abstract:

Graphene has sparked considerable scientific curiosity owing to its remarkable characteristics such as strength, flexibility, and electrical conductivity. This thesis delves into the influence of magnetic fields resulting from geometric deformations on graphene's surface on hydrogen storage capacity. Our simulations reveal a disruption in hydrogen absorption at an approximate concentration of 0.75 M, impacting its storage capacity. Notably, the x^2 - y^2 geometric deformation exhibited the highest hydrogen absorption rate of 62.5%.

Keywords: Graphene, magnetic fields, geometric deformations, hydrogen absorption, storage capacity.

Résumé :

Le graphène est une grande curiosité scientifique en raison de ses caractéristiques remarquables telles que sa résistance, ses souplesses et sa conductivité électrique. Celui-ci explore l'influence des champs magnétiques résultant des déformations des géométries à la surface du graphène sur la capacité de stockage de l'hydrogène. Nos simulations se réfèrent à une perturbation de l'absorption d'hydrogène à une concentration environnementale de 0,75 M, qui est sans impact sur sa capacité de stockage. Notamment, la déformation géométrique x^2 - y^2 a présenté le taux d'absorption d'hydrogène le plus élevé, soit 62.5%.

Mots-clies : Graphène, champs-magnétiques, déformations géométriques, absorption d'hydrogène, capacité de stockage.

ملخص:

أثار الغرافين اهتمامًا علميًا كبيرًا بسبب خصائصه المذهلة مثل القوة والمرونة والتوصيل الكهربائي. تتناول هذه الأطروحة تأثير الحقول المغناطيسية الناتجة عن التشوهات الهندسية على سطح الغرافين على سعة تخزين الهيدروجين. تظهر محاكاتنا انقطاعًا في امتصاص الهيدروجين عند تركيز تقريبي يبلغ 0.75 مولار ، مما يؤثر على سعة التخزين.،كما أظهر التشوه الهندسي $x^2 - y^2$ أعلى معدل امتصاص للهيدروجين بنسبة 62.5%.

الكلمات المفتاحية : الغرافين ، الحقول المغناطيسية ، التشوهات الهندسية ، امتصاص الهيدروجين ، سعة التخزين.

General introduction:

Graphene, a remarkable material of our time, possesses unparalleled properties that set it apart from other materials. It exhibits incredible strength surpassing that of steel while maintaining remarkable flexibility. Additionally, graphene showcases exceptional electrical conductivity, hundreds of times greater than copper.

These extraordinary characteristics have captivated the attention of scientists, leading to in-depth research and astonishing discoveries. One notable finding involves the ability to generate magnetic fields exceeding 300 Tesla through geometric distortions on the surface of graphene.

Based on this exciting field of study, the topic of this graduation thesis focuses on investigating the impact of such magnetic fields on hydrogen storage capacity. Hydrogen, a clean and vital energy source suitable for the environment, interacts with the magnetic moment of hydrogen and the magnetic field generated by geometric distortions on the graphene surface. This interaction energy can either stabilize hydrogen molecules or cause them to move away from the graphene surface.

To address this topic, the graduation thesis is divided into three chapters:

1. General Introduction to Graphene:

The first chapter provides an overview of graphene, discussing its mechanical and chemical properties, as well as its production methods. It also explores the electronic properties resulting from the Dirac equation, considering relativistic treatment due to the high speed of electrons. Additionally, the chapter delves into the energy band shape near the Fermi points, often referred to as the Fermi cone. Furthermore, successful methods for studying the electronic properties of graphene, such as Density Functional Theory (DFT), are discussed. The chapter concludes by highlighting various industrial applications of graphene, including flexible screens, sensors, and water filtration.

2. Hydrogen Storage:

The second chapter focuses on traditional hydrogen storage methods relying on high pressures, as well as unconventional approaches. It explores the challenges and advancements in hydrogen storage techniques, presenting a comprehensive overview of the subject.

3. Simulation and analysis:

The third chapter is dedicated to the simulation process for different forms of geometric deformations on graphene. It discusses the methodology employed and provides a detailed analysis and interpretation of the obtained results.

The thesis culminates with an inclusive overview, summarizing the primary discoveries and their implications within the realm of hydrogen storage concerning the generation of magnetic fields on graphene.

We sincerely hope that the findings and insights presented in our graduation thesis will serve as a valuable contribution to the ongoing research in this field. By investigating the interplay between graphene's magnetic fields and hydrogen storage capacity, we aim to expand the existing knowledge and deepen our understanding of this intriguing phenomenon.

I.1. Introduction :

Peierls[1] and Landau et al. [2] argued more than 75 years ago that strictly two-dimensional crystals are theoretically impossible, since thermal fluctuations disrupt crystal order over long distances. Subsequent experimental observations showed that as the thickness of the layers decreased (up to several tens of atomic layers), the melting point of the layers also decreased, causing their instability due to segregation or island decay. [3]

Although atomic monolayers have always been considered an integral part of larger three-dimensional structures, it was thought that two-dimensional materials could not exist without such a three-dimensional basis. This hypothesis was confirmed with the isolation of 2D graphene in 2004[4] and other materials[5] by Prof. Dr.Andre Geim and Prof. Kostya Novoselov from the University of Manchester, UK. [6] However, these new 2D materials do not violate Peierls's calculations, as they either form a coating on bulk material or generate a wave when freely suspended. [7 , 8],

I.2. Synthesis of Graphene:

There are four main approaches to synthesizing graphene. These are mechanical exfoliation, liquid phase exfoliation of graphite, epitaxial growth and chemical synthesis methods.

I.2.1. Mechanical exfoliation of graphite (tape method):

The mechanical exfoliation method, commonly known as the tape method, was initially employed by Heinrich Kurz et al. in 1990 to obtain ultrathin layers of highly oriented pyrolytic graphite (HOPG) [9]. This method involves the extraction of graphite with an interlayer spacing of less than 1°. However, it was in 2004 that Novoselov and Geim successfully utilized this technique to isolate and identify monolayer graphene [10].

The process starts by attaching a piece of HOPG to a sticky tape. The tape is then folded, causing the graphite layers to break into smaller crystals (see Figure 1.1). Subsequently, by tearing off the tape, the graphite flakes are divided into two individual pieces. This division process can be repeated several times to obtain thinner slices of graphene. Finally, the tape containing the graphene pieces is attached to a silicon wafer coated with a layer of silicon dioxide. The tape is then carefully peeled off, leaving the graphene flakes on the silicon wafer. These graphene flakes can be observed with the naked eye due to their distinct optical contrast.

The mechanical exfoliation (tape) method allows for the production of high-quality graphene with exceptional properties, such as high electrical conductivity and mechanical strength. However, this method is limited in terms of scalability and is primarily used for research purposes. It is difficult to control the size and shape of the graphene flakes obtained through this method.

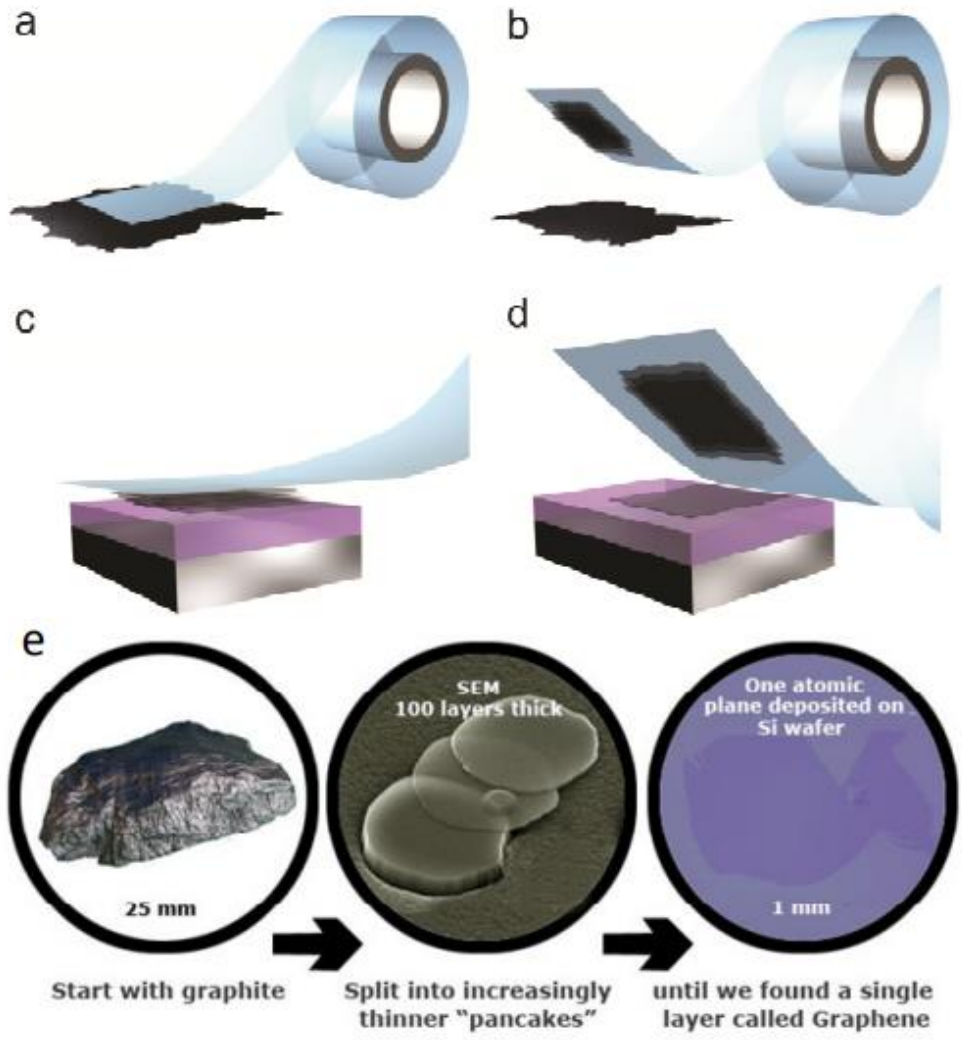

Figure (1.1): Gradual formation of graphene using the tape method (a to d) and an overview of the process using this method (e) [11]

Despite the simplicity of the process, it is unlikely to be produced in large quantities. Using this technique, Chen J. et al. recently reported a study titled "Continuous Mechanical Exfoliation of Graphene Sheets with a Three-Roller Mill" that proposes a scale-up process for the efficient fabrication of polymer/graphene nanocomposites (from one to many layers) [12].

I.2.2. Liquid-phase exfoliation of graphite :

Hernandez et al. [13] typically dispersed the graphite in N-methylpyrrolidone (NMP) followed by sonication to separate the unexfoliated graphite. Graphene dispersions with concentrations down to 0.01 mg ml-1 reached. The reason behind the production of graphene flakes is the solvent-graphene interaction. The energy required for exfoliation is balanced by this interaction for solvents when surface energies match those of graphene [13]. In addition,

Mariani et al. improved the concentration of graphene in the NMP (2.1 mg/ml) by exfoliation of polymer-graphite composite [14] and further improved (5.33 mg/ml) by exfoliation of graphite in ionic liquids [15]. Although the advantage of this technique is low cost and scalability, graphene flakes tend to stack and coil easily.

I.2.3. Epitaxial growth:

I.2.3.1. Epitaxial growth of SiC:

Walt de Heer and colleagues at Georgia Institute of Technology initiated the growth of graphene using the epitaxial growth method of silicon carbide (SiC) substrates [16]. This process involves the thermal desorption of silicon at high temperatures (>1250 °C) and low pressures (~10^{-6} Torr), leading to the formation of carbon-rich surfaces, which are subsequently graphitized as carbon islands (see Figure (2.1)a). STM analysis showed that graphene was successfully grown epitaxially from SiC with long-range order and low defect density (see Figure (2.1)b).

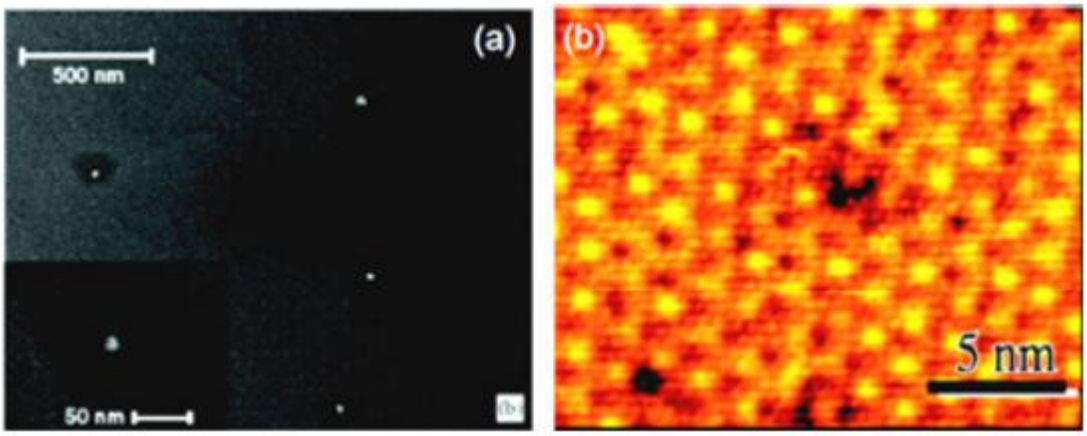

Figure (2.1): a) SEM image showing small hexagonal crystallites after the epitaxial growth process on a SiC substrate (b) STM image of epitaxial graphene with long-range order and low defect density [17].

In addition, the method has recently been optimized to obtain single or multilayer graphene [18]. The epitaxial growth of graphene from SiC has been achieved at specific locations that allow electronic devices to be fabricated using graphene. This process is more controllable and scalable than the exfoliation process, but is prohibitively expensive due to the high cost of the SiC substrate and the need for high processing temperatures.

Also, compared to exfoliation process graphene, the more brittle and defective grapheme tends to form due to the large lattice mismatch between SiC and graphene during the epitaxial process.

I.2.3.2. Epitaxial Growth on transition metals or transition metal deposited substrates :

Epitaxial growth of thin graphitic films on metal substrates such as Ru, Rh by Grant in 1970 and Ni by Blakely et al in 1970 has been already known for nearly half century [19] . After explosion of the interest in graphene by 2004, this method was extensively studied again to get controllable deposition of graphene. Chemical vapor deposition (CVD) of hydrocarbons at elevated temperatures is catalyzed by metal and indeed results in the growth of graphene. Carbon isotope labeling experiments clarify that the mechanism of graphene formation is dependent on carbon solubility of metal and CVD growth conditions [20]. Graphene is formed via adsorption on a metal surface of Cu in which carbon solubility is too low (0.008 wt% C at 1084ºC) during CVD process. On the other hand, graphene is produced on Ni surfaces where the carbon solubility is higher (0.6 wt % C at 1326 ºC). Graphene is formed during cooling step in the CVD process via surface segregation-precipitation of carbon from a metastable carbon–metal solid solution [21] (see Figure (3.1)).

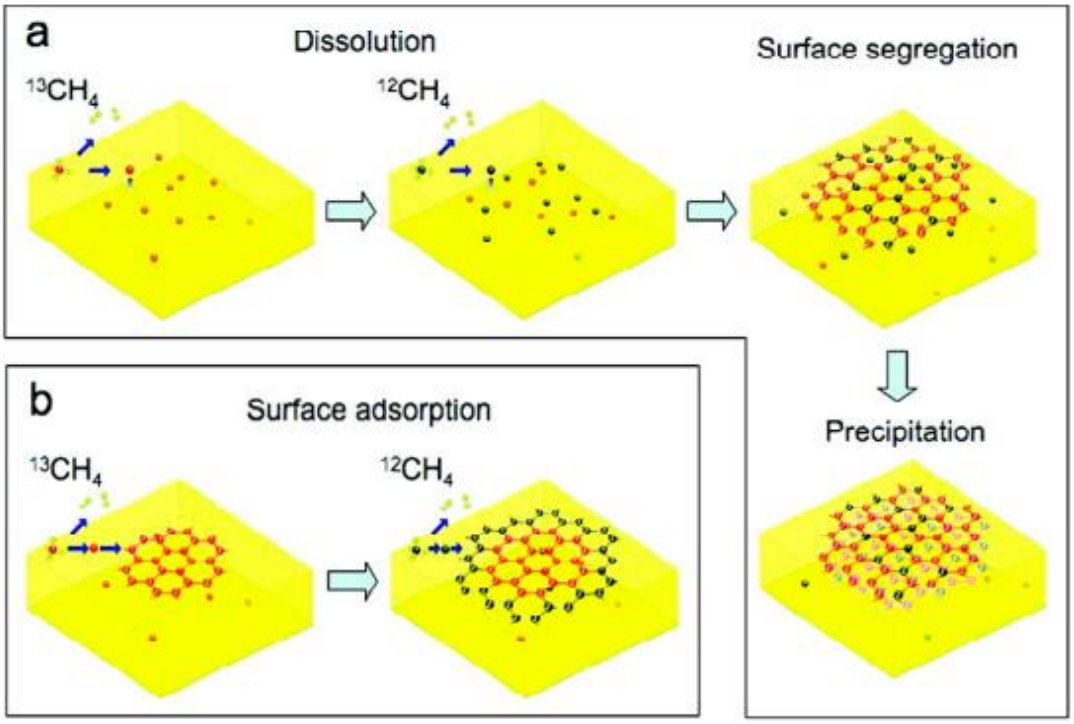

Figure (3.1): Graphs showing carbon isotope labeling experiments on (a)Ni, graphs with randomly mixed isotopes due to surface segregation and/or precipitation mechanism. (b) Cu, graphene with isotopes separated by a surface adsorption mechanism [20].

I.2.4.Chemical synthesis:

The fabrication methods mentioned earlier focus on synthesizing graphene with minimal defects and functional groups. However, in certain applications, the presence of defects or functional groups can be beneficial. For example, defects can act as anchoring sites for

nanoparticles, enabling the formation of graphene-nanoparticle hybrids. Additionally, while continuous graphene layers are required for transparent displays, gram-scale graphene is necessary for catalytic or battery applications.

Chemical synthesis techniques offer the ability to mass-produce graphene, even with a higher number of defects. These methods involve oxidation and reduction steps. In a typical process, graphite is oxidized to graphite oxide (GO) using strong oxidizing agents such as $KClO_3$, HNO_3, H_2SO_4, H_3PO_4, or $KMnO_4$. This oxidation step leads to an increase in interlayer distances due to the insertion of functional groups onto the carbon layers. As the degree of oxidation increases, the probability of obtaining high-quality graphene also increases, as graphene can be formed by reducing oxidized graphite.

Over time, different methods of oxidation have been developed, including the Brodie, Staudenmaier, Hummers, Improved Hummers, and Tour methods. Tour's method, for instance, yields GO with a higher degree of oxidation, as indicated by a higher interlayer distance value of 9.5 Å (Table 1.1). For a comprehensive overview of the various synthesis procedures for chemically derived graphene, please refer to Table (1.1).

Methods	Brodie	Staudenmaier	Hummers	Modified Hummers		Tour
Year	1859	1898	1958	1999	2004	2010
Oxidants	$KClO_3$ HNO_3	$KClO_3$ or $NaClO_3$ HNO_3 H_2SO_4	$NaNO_3$ $KMnO_4$ H_2SO_4	$K_2S_2O_6$ P2O5 $KMnO_4$ H_2SO_4	$NaNO_3$ $KMnO_4$ H_2SO_4	H_2SO_4 H_3PO_4 $KMnO_4$
C :O ratio	2.28	1.85	2.25	1.3	1.8	..
Reaction time	3_4 days	1_2 days	2_10 h	8 h	5 days	12h
Intersheet spacing (Å)	5.95	6.23	6.67	6.9	8.3	9.5

table(1.1): Synthesis of graphite oxide from graphite[22]

The introduction of polar oxygen functional groups imparts hydrophilicity to graphene oxide (GO), making it easily dispersible in many solvents, particularly water. The incorporation of oxygen functionalities into the GO structure weakens the van der Waals cohesion, leading to partial degradation of the sp^2 lattice to sp^2-sp^3 hybridized sheets with poor π-π stacking ability (Fig. (3.1)B). As a result, GO becomes non-conducting due to the absence of a continuous conducting graphite network. Chemical reduction of GO to chemically derived graphene (CDG), for example, using hydrazine hydrate, or thermal reduction through annealing at 1000°C under an argon current, can be employed to restore the conductive graphite network by removing functional groups through a reduction process (Fig. (4.1)) [23].

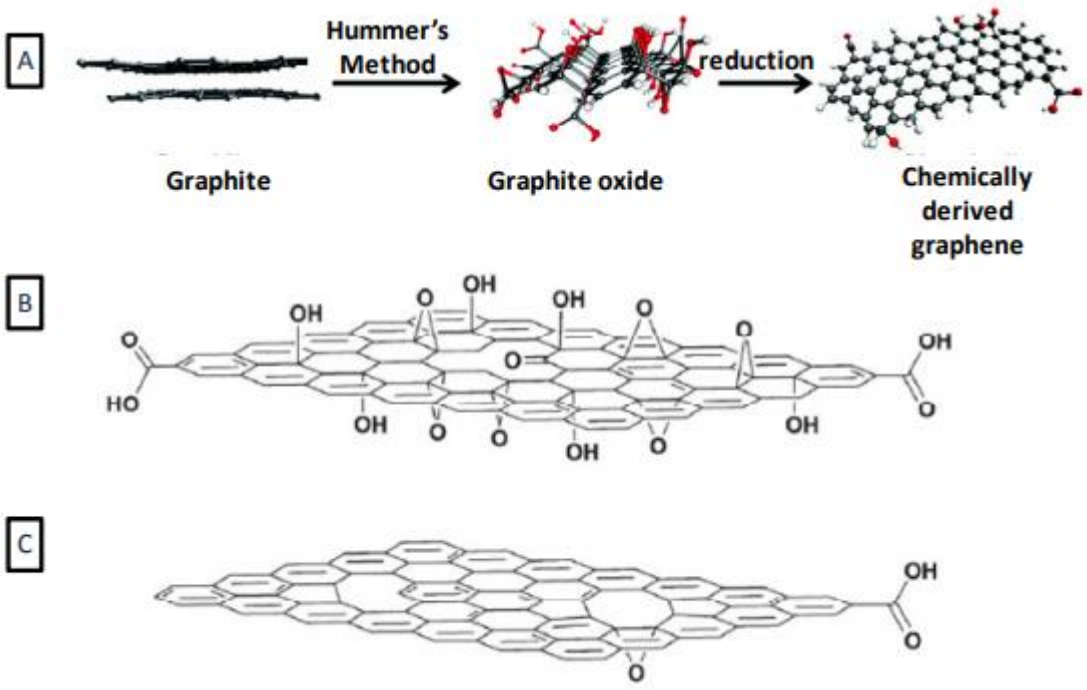

Figure (4.1):A. A molecular model showing the oxidation and reduction process of graphite to chemically derived graphene (CDG) [24]. B. graphite oxide (GO) and C. CDG [22]

To summarize, there are various methods available for the synthesis of graphene, including micromechanical cleaving, chemical exfoliation, and epitaxial growth by chemical vapor deposition (CVD) [10] [25] [26]. These methods have demonstrated the ability to produce high-quality monolayers of graphene over large areas. Among them, mechanical cleavage of highly oriented pyrolytic graphite (HOPG) [10] and decomposition of SiC [17] are known to yield graphene with exceptional defect-free monolayer structures. However, both approaches face challenges when it comes to scalability.

Alternative techniques, such as combined chemical exfoliation and reduction methods, offer scalability advantages but often encounter issues related to the aggregation of graphene sheets caused by strong π-π stacking and van der Waals forces. Consequently, achieving graphene with fewer layers becomes problematic in such cases. However, by utilizing high-purity and high-quality metal substrates like Ir[26], Ru[28], Ni[26], Cu[29] in the CVD process and implementing precise control over synthesis temperature, cooling rate, and substrate quality, it is possible to prevent the agglomeration of graphene layers. This enables the formation of graphene films with controllable thickness, even down to the monolayer level.

I.3. TB modeling of the electronic structure of graphene:

The unique electronic structure of graphene is a result of its hexagonal lattice structure, and the behavior of electrons in graphene follows the principles of massless relativistic fermions, which satisfy the Dirac equation [30]. The presence of in-plane stress in the graphene layers leads to a significant modification of the band structure near the Fermi level, breaking the

inversion symmetry [31]. Theoretical studies investigating the impact of strain on the band structure of graphene and graphene nanoribbons have extensively employed both the tight-binding (TB) model and the ab initio approach [32, 33].

In this study, we focus on exploring the electronic structure of graphene foils under various in-plane stress distributions. We employ quantum mechanical calculations and the Hückel TB model [34, 35] to investigate the effects. Additionally, we examine the flexoelectric effect in graphene sheets with non-centrosymmetric pores, with a specific focus on cases where the breaking of inversion symmetry is confirmed for certain in-plane strain distributions. To facilitate our analysis, we define the x-direction along the undistorted graphene axis, while the horizontal direction is denoted as y, as illustrated in Figure (5.1).

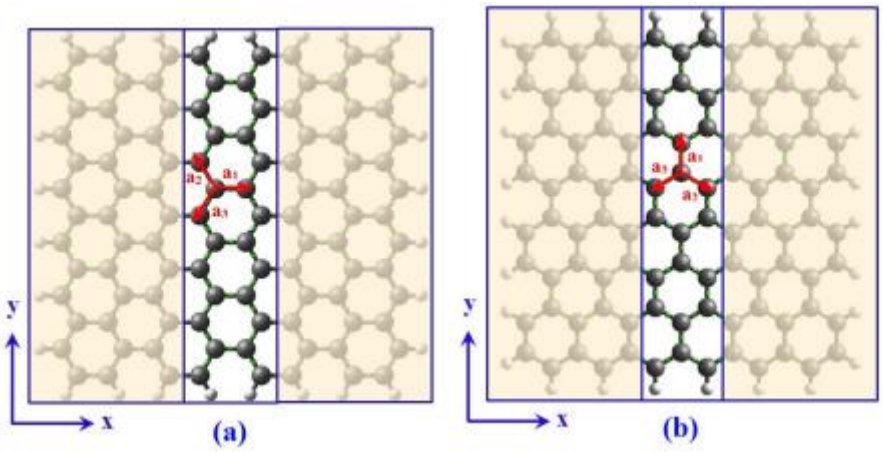

Figure (5.1) depicts the unit cell of (a) a chair graphene sheet and (b) a zigzag graphene sheet. The vectors a_1, a_2, and a_3 represent the combined vectors that define the unit cell structure [125].

When a graphene sheet undergoes uniaxial or shear strain, the x-component of the i^{th} atomic coordinate undergoes the following changes:

$$\begin{Bmatrix} x_i \to (1+\varepsilon_A)x_i \\ x_i \to (1+\varepsilon_Z)x_i \end{Bmatrix} \quad \text{Uniaxial strain} \tag{1.1.a}$$

$$x_i \to x_i + \gamma y_i \quad \text{Shear strain} \tag{1.1.b}$$

The strain experienced by a graphene sheet can be characterized by two components: uniaxial strains along the chair (ε_A) and zigzag (ε_Z) directions, and a shear strain (γ). These strains

collectively define the strain tensor that describes the uniform deformation in the graphene sheet.

$$\varepsilon=\begin{bmatrix}\varepsilon_A & \gamma \\ 0 & \varepsilon_Z\end{bmatrix} \quad (1.2)$$

In the deformed graphene layer, the real space vectors are

$$r=(I+\varepsilon)r_0 \quad (1.3)$$

the strain tensor is represented by I = $(\delta_{ij})2x2$, with δ_{ij} being the Kronecker delta. The subscript "0" indicates the state of the graphene layer before deformation. As a consequence of the deformation, the Brillouin zone (BZ) corresponding to the reciprocal vector k in the deformed space deviates from its original regular hexagonal shape and is altered [32].

Enter a new quantity

$$\mathbf{k}'=(I+\varepsilon)^T\mathbf{k} \quad (1.4)$$

The quantity **k**' can be treated as an undistorted inverse vector. BZ in space **k**' has become hexagonal again, because

$$kr=k(I+\varepsilon)r_0=(I+\varepsilon)^T kr_0=k'r_0 \quad (1.5)$$

This approach facilitates the analysis of electronic state changes near the Fermi point $\mathbf{k}_F$ with strains, and the Hückel-Hamilton operator TB becomes

$$H(k)=\sum_{i=1,2,3} t_i \exp(i\mathbf{k}a_i) = \sum_{i=1,2,3} t_i \exp(i\mathbf{k}'a_{i0}) \quad (1.6)$$

with Harrison's jump parameter, $t_i = t_0(a_0/a_i)^2$ [35]. This parameter considers the effect of deformation on the variation of ti. In the case of symmetrical strains, where $t_1 = t_2 = t_3$ (as shown in Figure (6.1)a), the Fermi point k'_F can be determined by solving $E(k_F) = |H(k_F)| = 0$. However, under uniaxial strains, t_1, t_2, and t_3 become asymmetric, as depicted in Figures (6.1)(b) and (6.1)(c), causing the Fermi points to deviate from K in the k-space.

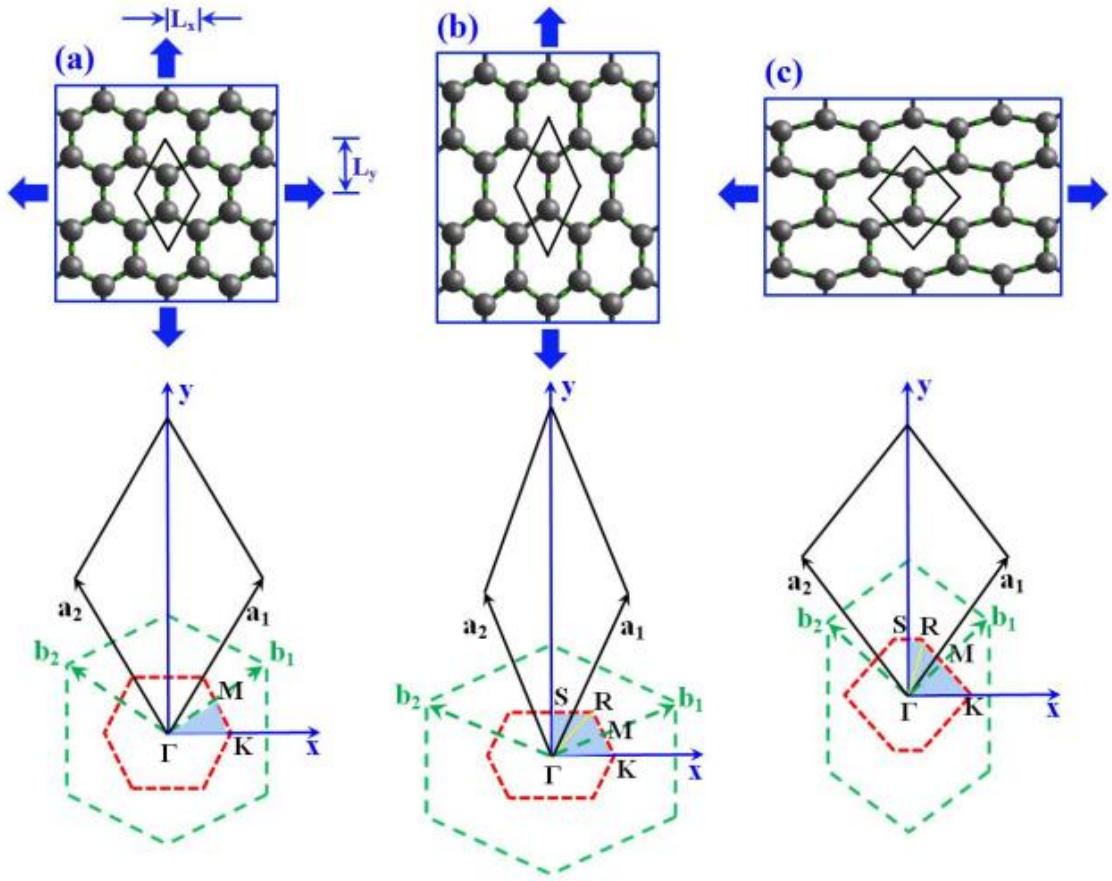

Figure (6.1) illustrates different types of graphene systems with strain distributions. In (a), symmetric strain distributions are shown for system graphs. In (b), chair graphs exhibit asymmetric strain distributions, and in (c), zigzag graphs also exhibit asymmetric strain distributions. The corresponding primitive cells are depicted in solid black, while the inverse lattices are represented by green dashed lines. The red dashed lines indicate the Brillouin zones (BZs), and the cyan regions represent the irreducible BZs. The maximum symmetry points, denoted by Γ, K, M, R, and S, are indicated on the figure. Additionally, Lx and Ly represent half the diagonal lengths of the primitive cells [125].

In a linear approximation, the deviation from $\Delta\mathbf{k}'_F=\mathbf{k}'_F-\mathbf{k}'_K$[34] is:

$$\Delta\mathbf{k}'_{Fx}\, a_0=C_t[\varepsilon_y(1+\upsilon)\cos3\theta+\gamma\sin3\theta] \quad (1.7.a)$$

$$\Delta\mathbf{k}'_{Fy}\, a_0=-C_t[\varepsilon_y(1+\upsilon)\cos3\theta+\gamma\sin3\theta] \quad (1.7.b)$$

$\Delta k'_{Fx}$ and $\Delta k'_{Fy}$ represent the components of $\Delta k'_F$. θ denotes the angle between the x-axis and the zigzag direction. ε_y refers to the uniaxial strain along the y-direction. υ represents Poisson's ratio, while a_0 represents the equivalent bond length. C_t is defined as follows:

$$C_t = -\frac{a}{2t}\frac{dt}{da}\Big|_{a=a_0} \quad (1.8)$$

The displacement of K' in k' space is opposite to that of K. The dispersion relation of the deformed graphene can be obtained by expanding E(k) around the Fermi points.

$$E(\mathbf{k}') = \pm\frac{3}{2} t_0 a_0 |\mathbf{k}' - \mathbf{k}'_F| \quad (1.9)$$

Therefore, the impact of small strain is observed as the movement of the energy cone in the k' space, as illustrated in Figure (7.1).

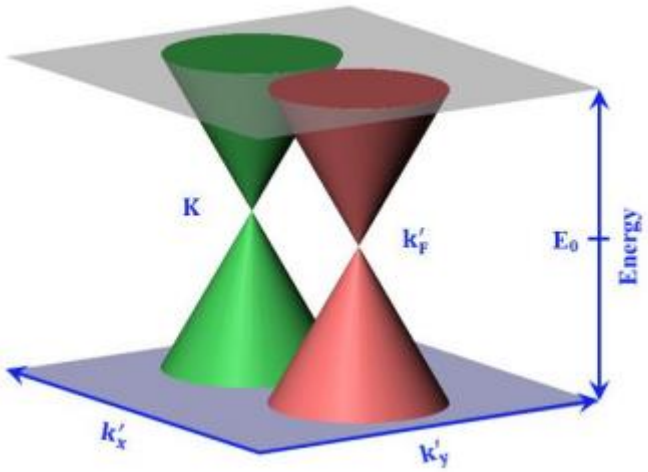

Figure (7.1) depicts a schematic representation illustrating the movement of the energy cone associated with the K points in the k' space. [125]

By combining equations (7) and (9), we obtain the following relationships for the pseudo deviation at the K and K' points in the k' space.

$$E_{gap}(k'_V) = 3t_0 S_t(1+\upsilon_A)\varepsilon_A \quad (1.10.a)$$

$$E_{gap}(k'_V) = 3t_0 S_t(1+\upsilon_Z)\varepsilon_Z \quad (1.10.b)$$

I.4. Calculations of Quantum Mechanics Density Functional Theory:

DFT is an interesting method compared to traditional wave function based methods because the electron wave function of an N electron system depends on 3N space coordinates while the electron density does not depend on only three coordinates (x, y and z).

In the DFT, the total electron energy E(ρ) is the sum of the kinetic energy of the electrons T(ρ), the energy of the electrons in the external field V(ρ), and the electron-electron interaction energy $V_{e-e}(\rho)$; knowledge.

$$E(\rho)=T(\rho)+V(\rho)+ Ve\text{-}e(\rho) \quad (1.11)$$

In 1964, Hohenberg and Kohn [36] showed that the energy and electronic properties of atoms and molecules can be determined using the electron density ρ(r)=ρ(x,y,z).

The electronic system can be characterized by functionals, i.e. location-dependent electron density. The Kohn-Sham equation in atomic Hartree units [37] has the form

$$\left[\frac{-\nabla^2}{2} + \vartheta_{ext}(r) + \vartheta_{Hartree}[\rho](r) + \vartheta_{XC}[\rho](r)\right]\psi_i(r) = \psi_i(r) \quad (1.12)$$

The energy functional of the system can be expressed as a combination of three terms. The first term represents the kinetic energy of the electrons, the second term represents the external potential acting on the electrons, and the third term represents the Hartree potential, which accounts for the classical electrostatic repulsion between electrons.

The XC (exchange-correlation) potential, denoted as $\vartheta_{XC}[\rho]$, is given by the following expression:

$$\vartheta_{XC}[\rho](r) = \frac{\delta E_{XC}[\rho]}{\delta\rho(r)} \quad (1.13)$$

where $E_{XC}[\rho]$ is the energy functional XC related to the electron density ρ given by

$$\rho(r) = \sum_i^{Occupied} |\Psi_i(r)|^2 \quad (1.14)$$

where the sum runs through the occupied states.

I.5. Graphene properties:

Graphene is an infinitesimal subcaste of carbon tittles in sp^2 hybridization,where carbon tittles form a hexagonal(honeycomb) crystal clear structure. Graphene was originally prepared in 2004 by mechanical exfoliation from largely- acquainted pyrolytic graphite(HOPG). For trials proving exceptional parcels of graphene([38]) its discoverers Andre Geim and Konstantinov Novoselov were awarded the Noble prize in 2010. Until that time, graphene was the first successfully insulated two- dimensional(2D) demitasse. The fact that the consistence of graphene is just one- atom(roughly0.35 nm) results in a whole range of extraordinary parcels.

The electronic band structure of graphene is fully unique(Figure (8.1)). Graphene is a semimetal with a bandgap energy Eg = 0 eV. Edges of valence and conduction bands touch at so called Dirac points. As charge carriers, there are both electrons and holes present in the graphene(ambipolar field- effect). Graphene evinces direct dissipation of electrons and holes at low powers. The dissipation relation is given by equation (1.15), where γ_0 is the so- called hopping parameter, whose value is2.8 eV for graphene, k_y and k_x are the y- and xcomponents of the surge vector k, and a = 0.142 nm is the distance of nearest neighbor carbon tittles in graphene. Equation (1.15) could be, in the vicinity of the Dirac points(for low powers), simplified to equation (1.16), where ħ is the reduced Planck constant and $\nu_F \approx 10^6$ m/ s the Fermi haste of electrons in graphene.

$$E(k)=\pm\gamma_0\sqrt{1+4cos^2k_y\frac{a}{2}+4cosk_y\frac{a}{2}+cosk_x\frac{\sqrt{3}a}{2}} \quad (1.15)$$

$$E(k)=\pm\hbar\nu_F|k|=\pm\hbar\nu_F\ \sqrt{k_x^2+k_y^2} \quad (1.16)$$

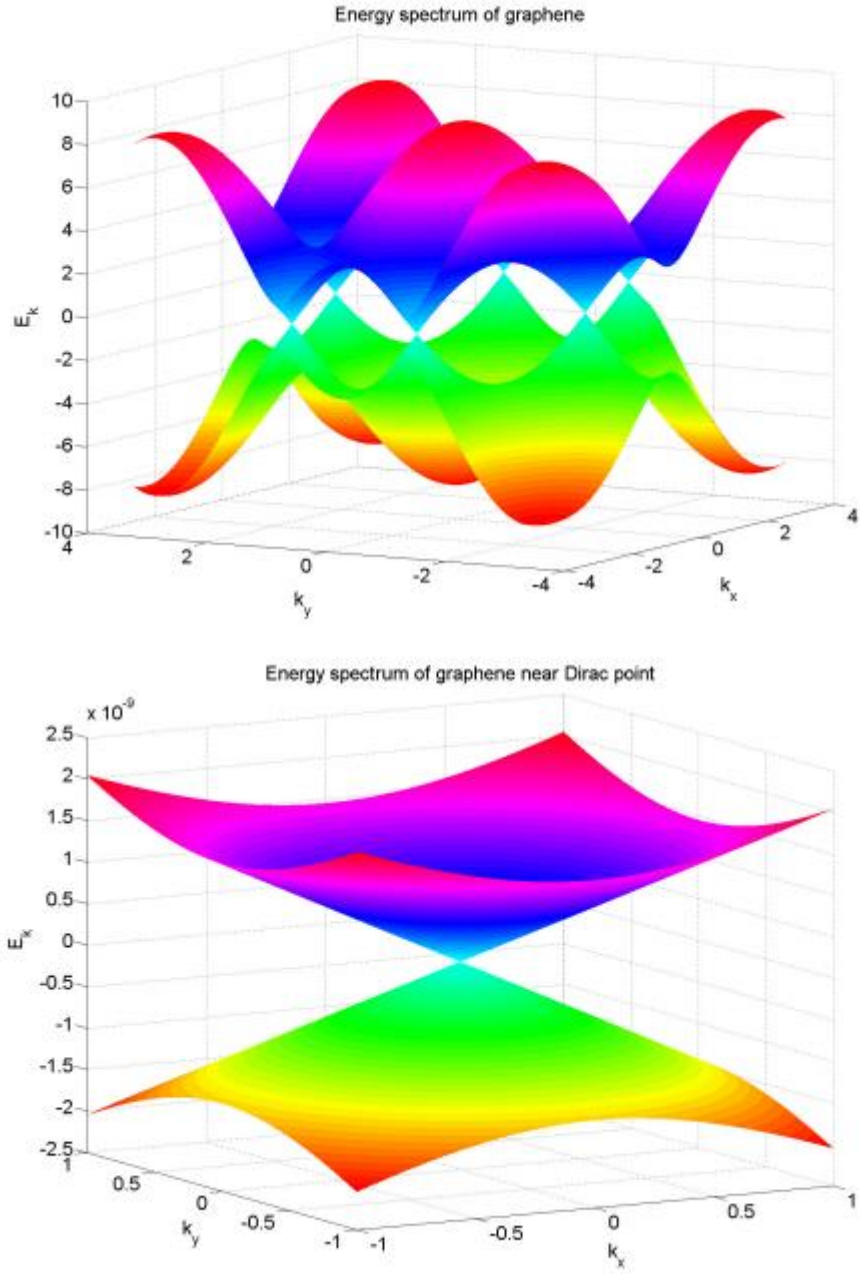

Figure (8.1) shows the energy spectrum of graphene obtained from equation (1.15), as well as the energy spectrum for low energies near the Dirac point obtained from equation (1.16). The conductivity of graphene is quantized, and the minimum conductivity value, denoted by σmin, is equal to 4e2/h at the Dirac point [39]. This quantization arises from the confinement of electrons in a two-dimensional system [40]. In graphene, electrons behave as Dirac fermions with a 1/2 spin and effectively zero mass, resulting in high carrier mobility μ. Further details regarding the mobility of charge carriers in graphene are discussed in the section on Graphene Transistors [126].

I.6. Applications of graphene :

I.6.1. Flexible electronics:

Flexible electronics is poised to become the ubiquitous platform for the electronics industry [41]. By achieving performance on par with rigid technologies but in lightweight, foldable, and flexible formats, it opens up numerous possibilities for new applications. The advent of truly conformal, reliable, and even transparent electronic devices becomes feasible. This development is crucial not only for flexible devices but also for compact, rigid systems requiring tight component assembly. Additionally, it can lead to cost reductions and high integration of electronic systems through innovative mass production methods like printed electronics, roll-to-roll processing, and lamination, which were previously inaccessible with traditional platforms using fragile materials and devices.

The flexibility of electronics not only allows for novel form factors and consumer appeal but also enhances reliability and enables the creation of new types of electrical systems [86]. Smaller, thinner, and more flexible devices [41,42] can be seamlessly integrated into our surroundings, offering unique benefits. For instance, improved flexible electronic solutions can offer miniaturized, cost-effective, and disposable sensors embedded in transparent and flexible surfaces. This breakthrough would facilitate the realization of ubiquitous, self-powered sensor networks for the long-awaited Internet of Things [43] and Everything Connected [44]. Such sensor networks have vast applications in smart homes, industrial processes, environmental monitoring, personal healthcare, and more.

I.6.2. Thin films, joint prostheses:

In certain medical applications, the need for hydrophobic materials with either a cell-free adhesive surface or an adhesive surface with cells arises. For instance, devices that come into contact with human blood, such as artificial heart valves, require a cell-free adhesive surface. On the other hand, joint prostheses in the friction zone necessitate an adhesive surface with cells to ensure complete tissue integration with the human body. Graphene presents a potential solution as a biocompatible coating, either alone or in combination with other carbon coatings like nanodiamond coatings or DLC [45][46].

To fully explore this potential, techniques for graphene ink deposition and growth on metals must be adapted to be competitive and capable of covering large and complex surfaces. Graphene coatings can be applied to medical instruments, although research in this area is still in its early stages and requires significant improvement [47][48]. Additionally, graphene can serve as a reinforcement for polymer and ceramic prostheses. Even small amounts of graphene or GO (graphene oxide) can enhance the elongation at break of polymers, resulting in stronger materials. These graphene-based polymer composites also exhibit favorable tribological properties, which can be advantageous in the fabrication of prostheses [49].

I.6.3. Magnetic sensors:

The detection of small magnetic fields, ranging from micro- to nano-Tesla levels, poses a significant challenge in various fields such as scanning probe magnetometry, biosensors, and magnetic storage. Existing technologies like Giant Magnetoresistance and Tunnel Magnetoresistance have limitations related to thermal magnetic noise and torque instability [50][51][52].

Embedded Hall sensors offer a wide range of applications, including automotive, computer, industrial control, and consumer devices, making up a substantial market worth around $870 billion and accounting for 90% of the magnetic sensor market [54][55]. Graphene-based Hall-effect sensors provide an alternative solution. These sensors can be fabricated in specific geometries, utilizing the Hall effect to measure and determine the strength of magnetic fields. They offer the capability to detect small magnetic particles or image magnetic fields with high spatial resolution when used as scanning probes [54].

By leveraging the unique properties of graphene, such as its high carrier mobility and sensitivity, graphene-based Hall-effect sensors hold promise for overcoming the limitations of current technologies in detecting small magnetic fields. Further advancements and research in this area can pave the way for improved scanning probe magnetometry, biosensing, and magnetic storage applications.

I.6.4. Chemical sensors:

The utilization of MoS_2 for gas sensing dates back to 1996, where devices incorporating thin MoS_2 films with embedded Pt catalysts demonstrated high selectivity and sensitivity towards hydrogen [56]. In recent years, advancements in manufacturing processes and the fabrication of single-layer devices, aided by graphene-related research, have sparked renewed interest in MoS2-based gas sensing [57].

A study referenced as [58] employed mechanically exfoliated MoS_2 to create solid-state field-effect transistor (FET) devices and successfully detected NO gas at concentrations as low as 0.8ppm. The research findings highlight that multi-layer MoS_2 exhibits stable and robust NO detection capabilities, while single-layer FETs showed less stability. Reference [59] provides insights into the enhanced performance of 2L-MoS_2 field sensors, attributing it partially to the lower charge transfer barrier observed in multilayer structures.

A highly sensitive MoS_2 thin-film transistor (TFT) was developed, utilizing reduced graphene oxide (RGO) as the contact layer. This MoS_2-TFT exhibited an impressive detection limit for NO gas, reaching as low as 2 parts per billion (ppb) [60]. The sensitivity of the device was further enhanced by a factor of 3 through the functionalization of Pt nanoparticles [60].

I.6.5. Strain sensors:

Single-walled carbon nanotubes (SWNTs) exhibit a significant change in relative resistance ($\Delta R/R$) per strain, denoted as ξ, which is determined by the length change (ΔL) relative to the original length (L_0) [61]. This change can reach values of approximately 10^3, depending on the SWNT chirality, and is primarily attributed to strain-induced modifications in the band gap.

Graphene, on the other hand, possesses remarkable mechanical properties, being able to endure high loads without suffering permanent damage, with a strain tolerance of up to 26% [62]. Furthermore, graphene exhibits relatively low fluctuations in electrical conductivity (σ) under mechanical strain, with variations of around 6% [62]. It should be noted that graphene's thickness factor, a measure of its mechanical robustness, has been reported as 6 [63], which is significantly lower than what can be achieved with SWNTs. Interestingly, when graphene grown through chemical vapor deposition (CVD) is transferred to polydimethylsiloxane (PDMS), a much higher thickness factor of approximately 151 has been observed [64].

I.7. Impermeability of Graphene:

In the study conducted by Bunch et al. [65], the permeability of various gases through a microchamber covered with a graphene foil was tested (Fig. 3.1). The experiment involved a graphene foil blister being pushed through a single-layer foil with a 2 x 2 μm2 opening under a negative pressure of -93 kPa. The system was then subjected to vacuum conditions (0.1 Pa) for 4 days, followed by releasing the system to atmospheric pressure while exposed to different gases. The leak rates were determined by measuring the change in pressure during the experiment.

$$\frac{dN}{dt} = \frac{V}{K_B T}\frac{dP}{dt} \qquad (1.17)$$

The leakage rate of helium (He) through the microchamber was measured to be between 10^5 and 10^6 atoms/sec. Interestingly, this leakage rate was found to be independent of the number of graphene layers in the foil. It is worth noting that the leakage rates observed for diffusion through silica microchambers were similar.

This suggests that the permeation occurs not through the graphene layer itself but rather through the walls of the microchamber.

Furthermore, Bunch et al. also calculated an upper bound for the probability of helium (He) atoms moving through graphene. They used the equation $\frac{dN}{dt}\frac{2d}{Nv}$ where d represents the depth of the microchamber and v is the velocity of the helium atoms.

The estimated upper bound probability was found to be 10^{-11}. By considering an estimated tunneling barrier of 8 eV (3.5 eV for the transient bond breaking 'window' mechanism), the probability of helium permeating through graphene is approximately ten orders of magnitude lower, specifically 10^{-335} (or 10^{-212}).

$$P=\exp\left(\frac{-2x\sqrt{2m(V-E)}}{h}\right) \quad (1.18)$$

The permeability of graphene is considered to be negligible for practical purposes, given that x = 0.3 nm, V is 8 eV (or 3.5 eV), and E is 25 meV (room temperature). Therefore, graphene is considered impermeable. However, the permeance of graphene can be influenced by the synthesis route, as it affects the presence of defects. For example, graphene synthesized via chemical vapor deposition (CVD) may have Stone-Wales defects, which can slightly reduce the barrier to helium diffusion. However, even with this reduction in barrier height (estimated to be between 6 and 9.2 eV), helium passage through graphene is not readily possible. Other types of defects, such as vacancy defects (e.g., 555777 divacancy, 858 divacancy, tetravacancy, hexavacancy, and decavancy), can significantly lower the barrier to helium penetration, with varying barrier heights ranging from around 0.05 eV to 8 eV. It is worth mentioning that the permeability of graphene can be controlled by creating fine pores in the material.

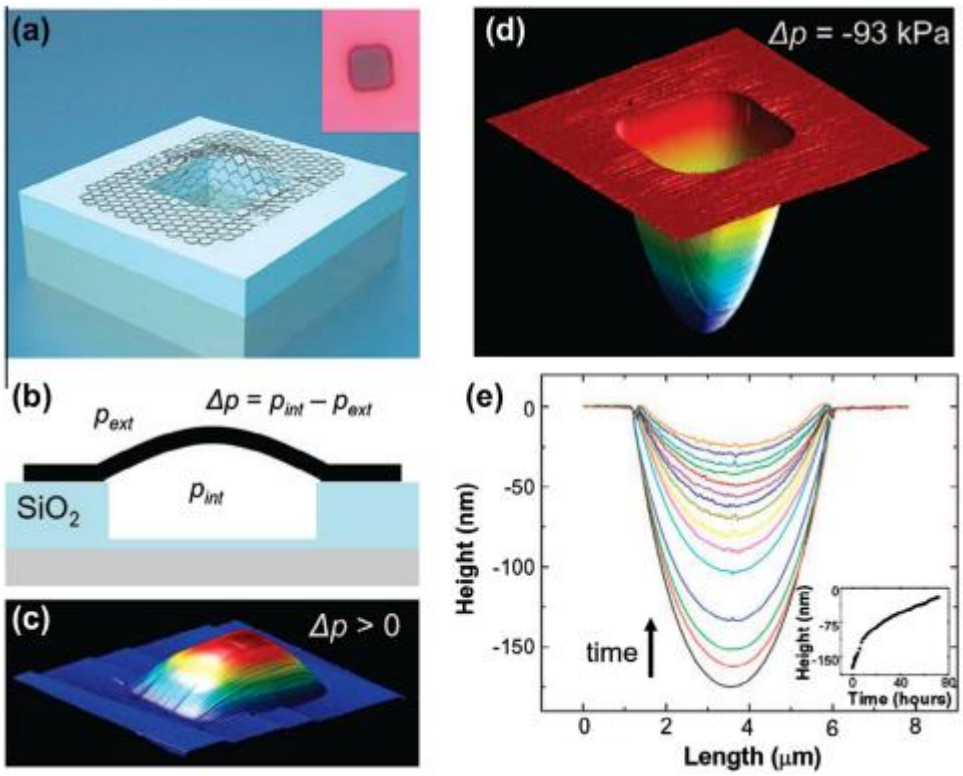

Fig. (9.1) – (a) Schematic of a graphene sealed microchamber.(Inset) optic image of a single infinitesimal subcaste graphene drumhead on 440 nm of SiO_2. The confines of the microchamber are4.75 x4.75 μm x 380 nm.(b) Side view schematic of the graphene sealed microchamber.(c) Tapping mode infinitesimal force microscope(AFM) image of a 9 nm thick numerous subcaste graphene drumhead with Δp> 0. The confines of the square microchamber are4.75 x4.75 μm. The upward deviation at the center of the membrane is 90 nm.(d) AFM image of the graphene sealed microchamber with Δ p-93 kPa across it. The minimal dip in the z direction is 175 nm.(e) AFM line traces taken through the center of the graphene membrane of(a). The images were taken continuously over a span of71.3 h and in ambient conditions.(Inset) deviation at the center of the graphene membrane vs time. The first deviation dimension(z) 175 nm is taken 40 min after removing the microchamber from vacuum. From Ref.[65].

I.8.Formation of pseudo-magnetic fields in strained graphene:

Formation of pseudo-magnetic fields in strained graphene investigates the characteristics of strained graphene on a nanopillar. The Raman spectrum analysis of strained graphene on the nanopillar (shown in Figure (10.1)a) is compared to the Raman spectrum of an unstrained control device. Two-dimensional Raman mapping confirms the highly periodic nature of the strained nanopillar array (inset of Figure (10.1)a). The measured 2D Raman peak shift of approximately 85.2 cm^{-1} is larger than previously reported values for deformed graphene on nanostructured substrates, highlighting the effectiveness of their strain engineering platform [71-74].

The local strain distribution is determined based on the topographic information obtained experimentally (Figure (10.1)b). A reconstructed 3 × 1 strained graphene nanopillar array is utilized, where the brightest and darkest regions correspond to heights of 300 nm and 0 nm, respectively. Strong structural deformation near the sharp corners and edges of the nanopillars results in a significant tensile strain of up to approximately 3.5% at the atomic scale. The strain distribution is decomposed into the x and y directions, with ϵ_{xx} and ϵ_{yy} panels showing that ϵ_{yy} is nearly absent where ϵ_{xx} is maximum, indicating a predominantly uniaxial strain in the strained graphene nanopillar.

A maximum experimental strain value of 1.3% is derived from the measured Raman shift in Figure (10.1)a, using a strain shift coefficient and the strain-shift relationship explained in the Methods section. However, there is a discrepancy between the simulated and measured maximum strain values due to the inherent resolution limit of the Raman measurement with the diffraction-limited laser spot size. To account for this, a convolution is performed on the simulated atomic-scale strain distribution using a two-dimensional Gaussian corresponding to the laser beam's spot size. This convolution yields a realistic strain distribution that matches the optically measured strain on the nanopillar, resulting in a maximum strain value of 1.32% (Figure (10.1)c). A comparison between the measured strain from the Raman shift and the

convoluted strain obtained from atomic-scale simulations shows excellent quantitative agreement.

It is worth noting that a clear strain variation between the edges and central part of a single nanopillar can be observed as long as the nanopillar's size exceeds the theoretical spatial resolution limit (~361 nm) of the Raman system used. The spatial distribution of pseudo-magnetic fields (B_S) at the atomic scale is obtained using a well-developed method based on tight-binding simulation techniques [77-83]. This method couples the Dirac equation to the deformed graphene surface and establishes the relationship between strain fields and gauge fields, enabling the visualization of pseudo-magnetic fields (Figure (10.1)d).

$$A_{x=}\frac{\beta}{2a_0}\left(\epsilon_{xx}-\epsilon_{yy}\right) \quad (1.19.a)$$

$$A_{y=}\frac{\beta}{2a_0}\left(-2\epsilon_{xy}\right) \quad (1.19.b)$$

The simulation method used to calculate the pseudo-magnetic fields in strained graphene is based on the tight-binding approach, where the Dirac equation is coupled to the deformed graphene surface. This method incorporates the strain tensor ϵ, with a constant β (approximately 3) and the nearest carbon-carbon bond length a_0 (approximately 0.14 nm), to determine the relationship between strain fields and gauge fields. The reliability of this simulation method is confirmed by its successful replication of the atomic-scale experimental pseudo-magnetic field distribution measured by scanning tunneling spectroscopy (STS) [81, 82, 84].

Figure (10.1)d shows the spatial distribution of the pseudo-magnetic fields, which can reach magnitudes of approximately 100 T near the sharp edges and corners of the strained graphene nanopillar. These regions exhibit the largest deformation and steepest strain gradient, as depicted in Figure (10.1)b. The observed pseudo-magnetic field distribution is in good agreement with a previous reference [85].

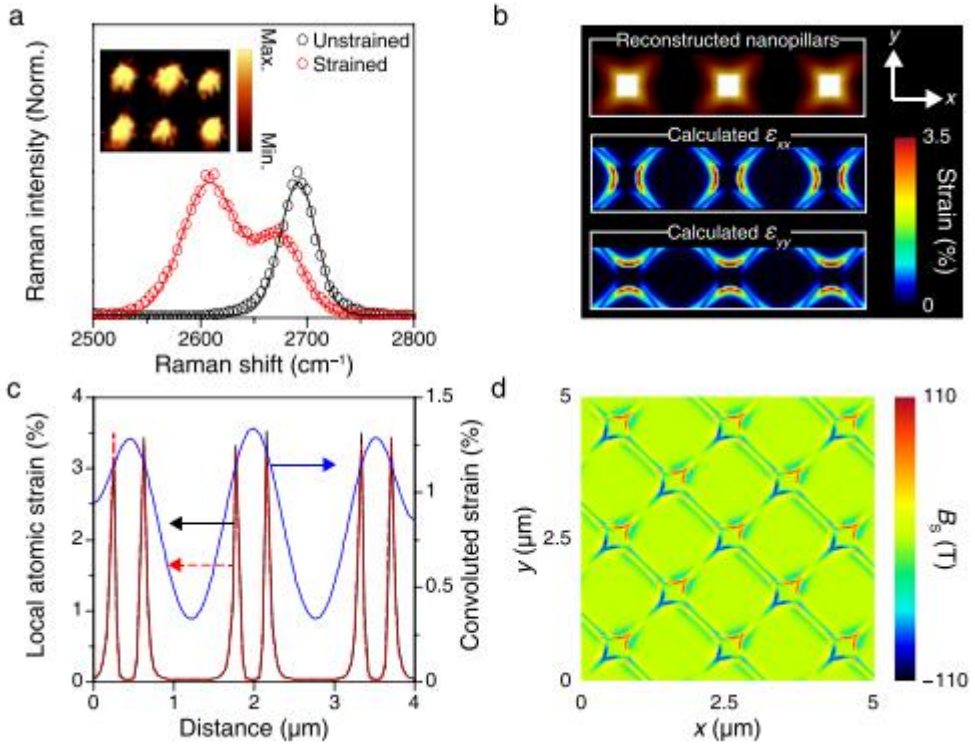

Figure (10.1) illustrates the formation of strong pseudo-magnetic fields in largely strained graphene. Panel (a) shows the Raman spectra of unstrained (black) and strained (red) graphene. The symbols in the figure represent dimension data, while the angles represent fitting data. The inset in panel (a) presents the two-dimensional Raman mapping data, plotting the 2D peak frequency of a simulated graphene nanopillar array with dimensions of 3 × 2. (b) displays the topographic image of a reconstructed strained graphene nanopillar array, specifically a 3 × 1 configuration. The top panel of this image corresponds to the topographic profile, where the brightest and darkest regions indicate heights of 300 nm and 0 nm, respectively. The middle and bottom panels represent the original strain distributions along the x-direction (ϵ_{xx}) and y-direction (ϵ_{yy}), respectively. It is observed that the strain along ϵ_{yy} is almost absent, while ϵ_{xx} exhibits maximum strain, indicating a predominant uniaxial strain in the strained graphene nanopillar.(c), a sampling of the strain profile is shown, demonstrating the original infinitesimal strain for ϵ_{xx} (black solid line) and ϵ_{yy} (red dashed line). Additionally, a sophisticated strain distribution (blue solid line) is depicted, obtained through convolution techniques. This realistic strain distribution takes into account the diffraction-limited laser spot size and is deduced from atomic-scale simulations.(d) presents the distribution of pseudo-magnetic fields in the simulated graphene nanopillar array [127]. The pseudo-magnetic fields exhibit significant magnitudes, reaching approximately 100 T, particularly near the sharp edges and corners where the deformation and strain gradient are most pronounced. This distribution of pseudo-magnetic fields aligns well with the findings of reference [85]

II.1. INTRODUCTION

Hydrogen energy is considered the most suitable alternative to fossil fuels due to its natural abundance, environmentally friendly combustion, and highest energy per unit mass [87–89]. The utilization of fossil fuels results in the emission of harmful gases like CO_2 and CO, posing risks to both human health and the environment [90,91]. To utilize hydrogen as a fuel, it is essential to ensure safe and compact storage methods that are also easily accessible [92].

Hydrogen storage can be achieved in gas, liquid, and solid forms, although gas and liquid storage methods are not recommended due to the need for large pressure vessels and high liquefaction costs. Solid storage, however, proves practical under certain conditions: the adsorption energy of H2 should range between -0.2 eV and -0.7 eV, and the hydrogen consumption of the system should exceed 6.5% following the guidelines of the United States Department of Energy (DOE-US) [93].

II.2. Properties of Hydrogen :

Hydrogen, being the lightest and most abundant chemical element in the known universe, constitutes approximately 74% of the total mass of chemical elements [94]. Figure (2.1) presents a comparison of the volumetric and gravimetric energy densities of various materials, indicating that while hydrogen exhibits the highest energy density (143 MJ/kg), its volumetric energy density in liquid form is relatively low (ranking 10th at 1 MJ/l). The challenge lies in the compression of hydrogen in liquid form due to its low critical temperature (32.79 K) and low liquid density (0.0708 kg/L at the melting point or 14.01 K). It is important to note that naturally pure hydrogen does not occur on Earth; instead, it is stored in compounds such as water and organic compounds.

When subjected to high pressure, hydrogen can infiltrate the interstitial sites of metal atoms, resulting in a phenomenon known as hydrogen embrittlement, which renders metals unsuitable for use as containers in high-pressure hydrogen equipment [95, 96].

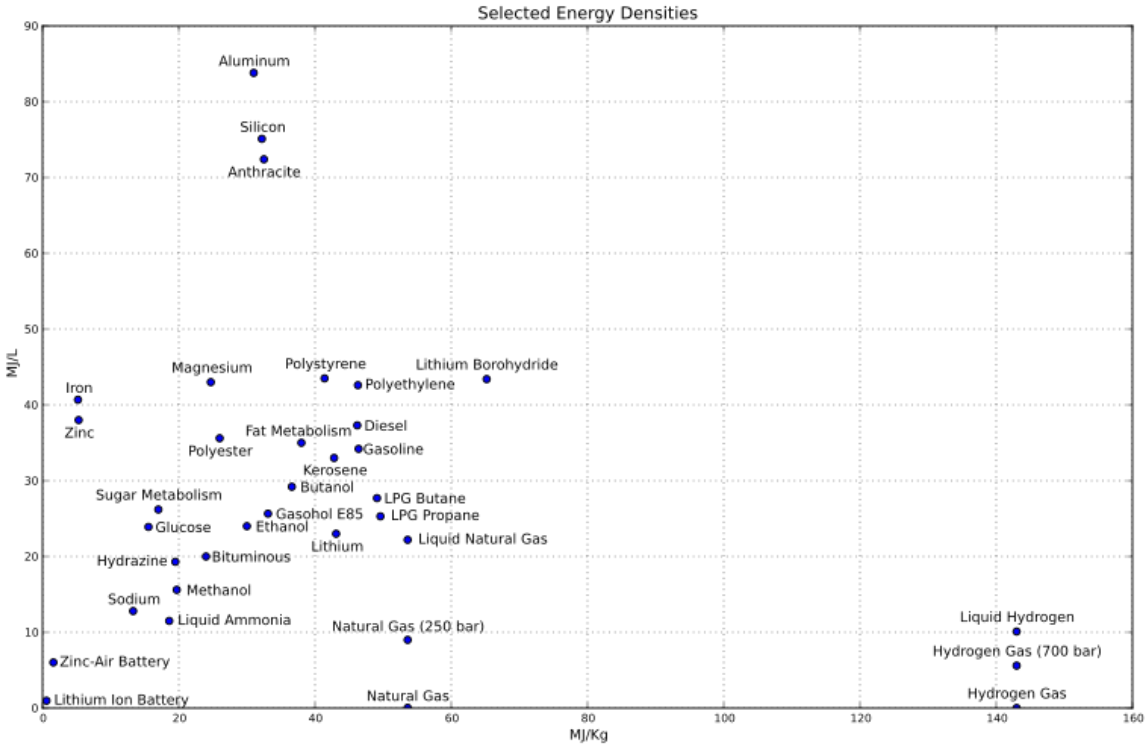

Figure (2.1), the image illustrates the energy densities of various materials [131].

Hydrides and other compounds offer significantly higher bulk densities of hydrogen compared to pure hydrogen [97, 98]. For instance, MgH2 has a density of 0.110 kg/l, LiH has a density of 0.099 kg/l, and LiBH4 has a density of 0.124 kg/l [99], whereas liquid hydrogen has a density of only 0.0708 kg/l (at 14.01 K). By utilizing hydride compounds, it becomes possible to store the same quantity of hydrogen in a much smaller volume, thereby enabling significant reductions in onboard storage volume for hydrogen use.

II.3. Physical storage of hydrogen :

II.3.1. Physiosorption :

(Physical adsorption) occurs when a gas (adsorbent) comes into contact with a solid surface (adsorbent). Adsorption in porous materials is governed by fluid-wall and fluid-fluid interactions, as well as the effect of limited pore space on the state and thermodynamic stability of liquids in narrow pores [100-102]. This is also reflected in the form or type of the adsorption isotherm.The IUPAC (International Union of Pure and Applied Chemistry) has published a classification of six types of adsorption isotherms and a pore classification based on their internal width (pore width defined as diameter in case of cylindrical and spherical pores and as distance between opposing pore walls in case of fission pores) [103]. Based on the diameter of the pores, they are divided into three groups: micropores with a width of less than 2 nm, mesopores with a width of 2–50 nm andmacropores with a width of more than 50

nm. These pore size classes are classified in the nanopore range , which defines pores down to 100 nm. In addition, the range of micropores is often divided into ultramicropores (pores smaller than 0.7 nm) and supermicropores (pores as small as 0.7 nm).from 7 to 2 nm). The pore size is commonly referred to as the internal pore size, although for mesopores it is common to refer to the pore radius (or pore diameter). Of course, these terms only have a precise meaning if the shape of the pores is well defined.

II.3.2. Hydrogen storage methods:

Hydrogen can be stored in various forms, including compressed hydrogen gas, liquid hydrogen, and cryogenic compressed hydrogen gas. Additionally, it can be stored through adsorption on materials with a large surface area under high pressure and low temperature, a process known as cryoadsorption. In the physical adsorption process, there is no chemical bond between hydrogen and the starting compounds (covalent and ionic interactions).

There are different types of physical hydrogen storage systems, some of which are as follows and will be discussed further:

1) CGH_2 (compressed gaseous hydrogen): Stored at 350-700 bar and room temperature.

2) LH_2 (liquid hydrogen): Stored at 1-10 bar and approximately -253°C.

3) CcH_2 (cryogenically compressed hydrogen): Stored at 250-350 bar and temperatures below -253°C.

4)Graphene.

II.3.2.1. Compressed gaseous hydrogen (CGH_2):

Offers a high gravimetric energy density (143 MJ/kg), but its volumetric energy density is relatively low (10.1 MJ/L). To achieve higher volumetric energy density, increasing the pressure and reducing the system volume are necessary. For a typical drive range of around 500 km for a passenger car, storing 5 to 6 kg of hydrogen onboard is required. Due to limited space in the vehicle, high pressure can be used to reduce the volume of the hydrogen tank. Currently, two widely used pressurized systems are 350 bar and 700 bar. At 700 bar, approximately 30% more hydrogen can be stored in the same volume compared to 350 bar. However, pressures exceeding 700 bar are not advantageous due to significant deviations from ideal gas behavior, making the increased demands on pressure containers unjustifiable considering the relatively small increase in hydrogen content.

To address the issue of metal embrittlement under high hydrogen pressure, the liner of CGH_2 containers is not made of metal. Instead, a high molecular weight polymer is used as a liner to act as a gas permeation barrier. A lightweight, high-strength carbon composite shell is applied to the outer polymer layer as a structural material, while metal is used as an impact-resistant outer shell to protect the inner layers (polymer and carbon composite). Additionally, an outer foam layer is incorporated for further impact protection. As an example, a typical 700 bar three-vessel carbon composite unit with 4.2 kg of hydrogen weighs 135 kg, while a similar

steel system would weigh 600 kg. Figure (2.2) provides a schematic drawing of a typical compressed hydrogen vessel design [104].

Concerns have been raised regarding the energy required to compress hydrogen from ambient conditions to high-pressure states. The practical mechanical energy used for compressing hydrogen to 700 bar and 350 bar is approximately 18 MJ/kg and 14.5 MJ/kg, respectively [105]. When comparing this energy with the energy stored in hydrogen (143 MJ/kg H2), the mechanical energy used for compression is still beneficial.

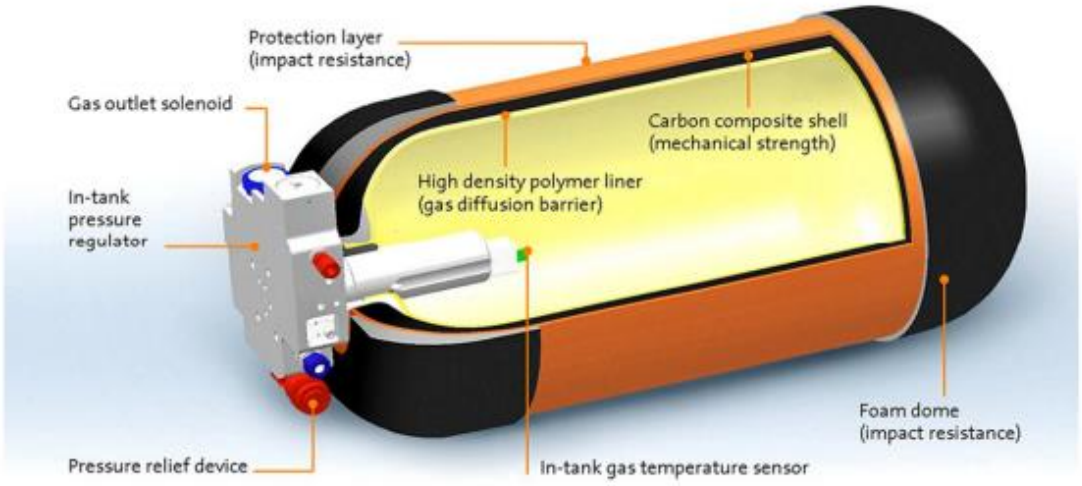

Figure (2.2) - Compressed hydrogen tank from Quantum Technologies, Inc., Irvine,USA[104]

The energy density for an optimal single-tank hydrogen tank is approx. 0.048 kg H_2 per kg tank weight and 0.048 kg H_2 per kg tank weight.023 kg H_2 per liter tank volume. The CGH_2 tank system offers the best overall technical performance and maturity for automotive applications to date. Thanks to the fast filling nozzle technology, an empty CGH_2 system can be fully filled in three minutes. Today, the 700 bar CGH_2 technology is the reference for all traditional and competitive alternative storage systems.

II.3.2.2.Liquid hydrogen:

Ambient heat to the LH_2.Thus, the pressure in the tank increases due to the vaporization of hydrogen and after some time when the pressure in the tank is higher than the maximum design pressure of the LH_2 system, the hydrogen has to be vented. The period of time between putting the vehicle into sleep or park mode and the release of the hydrogen gas is called the suspension period, which is typically around 3-5 days. Hydrogen released into the environment after this point is called vaporized gas. These losses are significant and should be minimized as much It is clear that converting gaseous hydrogen to liquid can increase its bulk density. As Figure (3.2) shows, the bulk density of liquid hydrogen (1 bar, 20 K) is about 80% higher than at 700 bar and at room temperature.

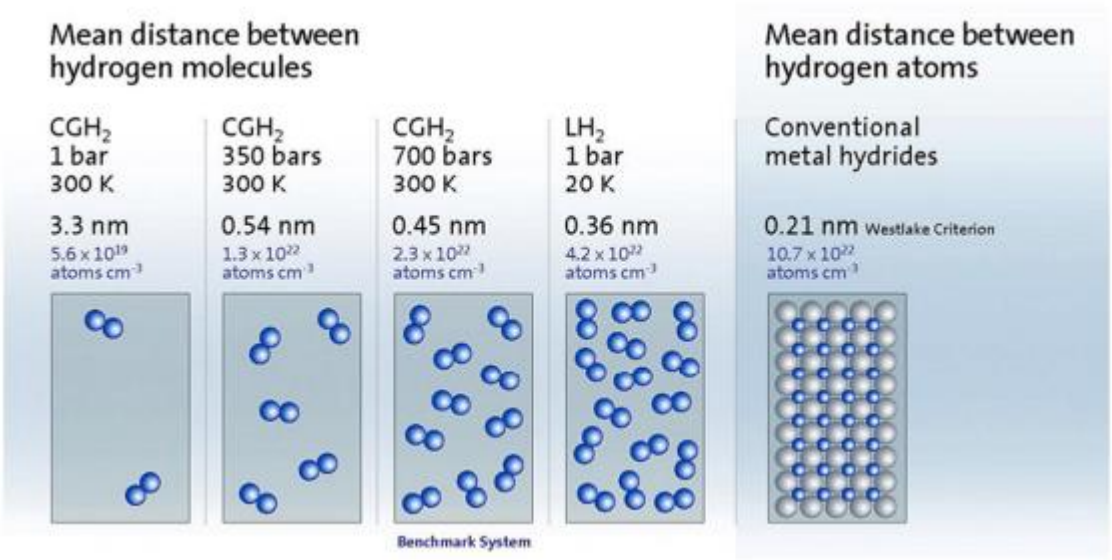

Figure (3.2) – Volume density of hydrogen depending on the material [106].

Since the critical temperature of hydrogen is very low (32.79 K), the LH_2 system must be kept at an even lower temperature, for example 20 K. Good thermal insulation is required due to the large temperature difference between the environment and the system necessary. Even with advanced engineering and materials, it is impossible to 100% prevent the transfer of as possible.

A cryogenic vessel requires a highly insulating material to minimize heat transfer.To minimize radiant heat transfer, multi-layer insulation (MLI), also known as super insulation, is often used. The MLI consists of 30-80 layers of Low-E radiation shielding. Considering the heat conduction effect of MLI, the optimal number of layers is around 40 [107]. Another important consideration in minimizing heat transfer is reducing the surface area to volume (S/V) ratio. Since the cryogenic tank is intended to be vehicle mounted, a folded shape is preferred to save space, but this would increase the S/V ratio of and cause thermal performance degradation.Figure (4.2) shows a typical LH_2 tank design.

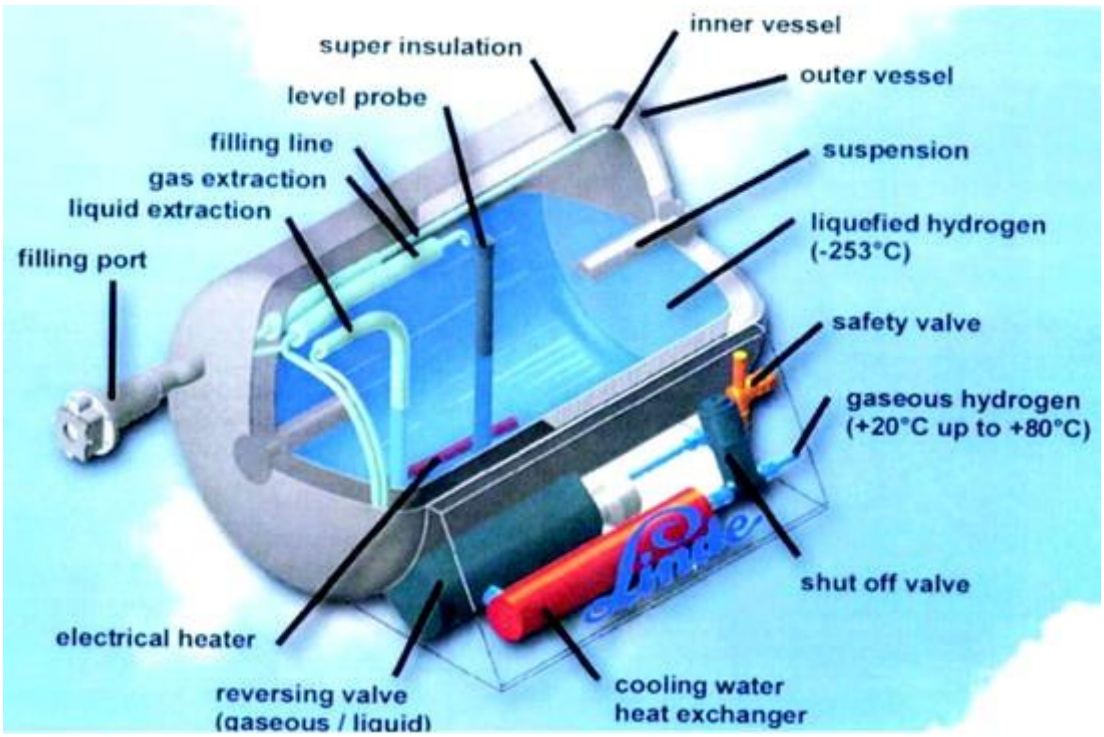

Figure (4.2) - Structure of a typical "Linde" LH_2 tank system. [132]

A well-insulated LH_2 tank can remain in a dormant state for an extended period. However, for the LH_2 system to function, it needs to be connected to other devices such as a filling device and a fuel cell that operate at room temperature. As a result, there are various channels and methods through which heat can transfer from the environment to the LH_2 tank, including heat conduction through pipes, cables, and fittings, convection, and heat radiation. Heat conduction and heat radiation are the dominant factors. The phase transition enthalpy of hydrogen between the liquid and gaseous states, which is about 0.45 MJ/kg, facilitates the vaporization process.

One drawback of the LH_2 system is the cooling losses that occur during the hydrogen filling process at a filling station. The entire transmission line between the fixed LH_2 tank and the vehicle's tank system needs to be maintained at a temperature of approximately 20 K, requiring significant energy and infrastructure. While current technologies can help minimize these losses, significant disadvantages still exist. Consequently, many automakers are showing less interest in the LH_2 system compared to the 700 bar CGH_2 system. One reason for this is the onboard hydrogen loss (evaporation) and the infrastructure complexity and cost associated with LH_2's cryogenic tanks. Another disadvantage is that approximately 30% of the chemical energy stored in hydrogen is required to liquefy it.

II.3.2.3.Cryo-compressed Hydrogen :

To overcome the drawbacks of LH_2 systems, one potential solution is to apply high pressure and maintain a low temperature. The Cryo-compressed Hydrogen System (CcH_2) was developed for storing hydrogen at high pressures (e.g., 350 bar) and cryogenic temperatures (above 20 K). The CcH_2 system allows for storing more hydrogen in the same volume with

significantly higher thermal resistance compared to the CGH_2 system. It also withstands longer dormant periods than the LH_2 system, resulting in reduced hydrogen loss. The CcH_2 system offers advantages such as extensive elimination of evaporation losses and easy transfer of hydrogen from filling stations to vehicles. Compared to cryoadsorption in large area material systems, the CcH_2 system eliminates the need for weight and additional costs associated with hydrogen adsorbing materials while achieving a similar volume and weight for the system.

Automobile manufacturer BMW [108] has developed second-generation cryogenic pressure vessels for automobiles, considering automotive requirements related to system performance, lifecycle, security, and costs (Figure 5.2). These cryogenic pressure vessels can operate using CGH_2, LH_2, or high-pressure supercritical cryogenic hydrogen (cryogenically compressed hydrogen).

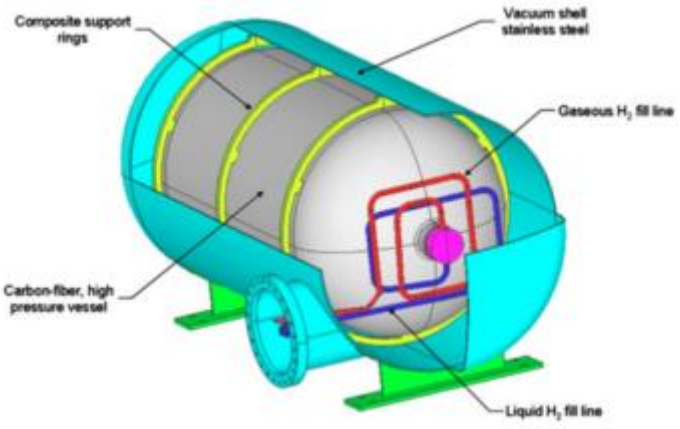

Figure(5.2) Structure of BMW generation 2 pressure vessel with cryogenic capacity [108].

In addition, the Lawrence Livermore National Laboratory in the United States built a third-generation system capable of storing 151 liters of hydrogen, with a total system volume of 235 liters and weighing 145 kg. It can store 10.7 kg of LH_2 at 1 bar or 2.8 kg CGH_2 at 4000 psi (275.8 bar) and 300 K. When loaded with LH_2 the system has a hydrogen density of 44.5 kg/m^3 (1.5 kWh/L) and a gravimetric density of 7.1% by weight .the cryogenic compressed storage system has the potential to meet the system's final 2015 gravity capacity target and the 2015 system volumetric capacity target. This system has a good chance of being commercialized in the future.

II.3.2.4. Graphene:

Graphene, a novel allotrope of carbon material, is currently being investigated for its potential in hydrogen storage. It is composed of a single layer of carbon atoms arranged in a densely packed honeycomb lattice structure, bonded together through sp2 bonds. Researchers such as Gosh et al. have reported a high graphene yield of 3 wt% at a temperature of 298 K and pressure of 100 bar [109]. Additionally, Eliasz et al. observed the hydrogenation of graphene in grapan, and fully hydrogenated graphene could potentially achieve a stoichiometry of CH with a storage capacity of 7.7 wt% [111, 112].

Simulations and calculations have indicated that the metallic surfaces of graphene (both sides) have the potential to achieve high weight percent (wt%) hydrogen adsorption. For instance, graphene coated with lithium has shown the ability to reach a weight percent of 12.8% [113], while aluminum-coated graphene has demonstrated the potential to achieve 13.79% by weight [114, 115]. However, it is important to note that these predictions still require experimental confirmation to validate their accuracy and feasibility.

II.4. Hydrogen storage measurements :

The techniques for H_2 adsorption can be classified into three main categories: (a) gravimetric techniques, which measure the amount of H_2 stored based on the added mass, (b) volumetric or manometric methods, which determine the amount of stored H_2 by measuring pressure changes in a known volume, and (c) temperature-programmed desorption techniques, which assess the amount of H_2 desorbed as a function of temperature [116]. In this study, the volumetric-manometric adsorption method was employed to quantify the adsorbed H_2 at both low pressures (0-1 bar) and high pressures (0-100 bar) across a wide temperature range (60-298 K).

In experimental measurements, the "excess" mass of H2 (m_{excess}) is determined. This value represents the difference between the total mass of H_2 (m_{total}) in the pore space and the mass of H_2 that would be present in the absence of adsorption.

$$m_{(exess)}=m_{(total)}- \rho_H.V_a \quad (2.1)$$

where ρ_H is the constant bulk density of H_2 and V_a is the volume of the absorbed phase. The amount of adsorbed H_2 in a solid is commonly quantified by its gravimetric capacity, which is calculated as the mass of adsorbed H_2 (adsorbate) divided by the combined mass of the adsorbent and adsorbate. This value is typically expressed as a percentage by weight.

$$\text{Capacity (wt.\%)} = \left[\frac{(Mass\ of\ abrorbed\ H_2)}{(Mass\ of\ host\ material)+(Mass\ of\ absorbed\ H_2)}.100\right]\% \quad (2.2)$$

II.4.1. Low-pressure hydrogen :

In this adsorption method, hydrogen gas (H_2) is used as the adsorptive gas. The adsorption measurements are conducted at a constant temperature ranging from 60 to 298 K, and the pressure is varied from vacuum to atmospheric pressure (~1 bar). The experimental setup includes using the same volumetric analysis gas as AUTOSORB 1-MP from Quantachrome Instruments and a two-stage closed-cycle cryocooler from Gifford-McMahon. Ultrahigh purity (99.9999%) H_2 gas is employed in the measurements.

During the adsorption process, the H_2 gas is gradually introduced to the solid surface, and the amount of gas adsorbed is recorded as the pressure increases from 0 to 1 bar at a temperature of 77.3 K. The reverse process, desorption, is also measured by gradually reducing the pressure. By the end of the measurement, isothermal H_2 adsorption/desorption curves are obtained, which represent the relationship between the quantity of adsorbed/desorbed H_2 gas and the equilibrium pressure at a constant temperature.

The resulting graph illustrates the amount of H_2 gas adsorbed as a function of pressure (P) in units of mbar. The adsorbed H_2 gas quantity can be expressed in various ways, such as the volume of H_2 adsorbed under standard temperature and pressure (STP) conditions (i.e., volume in cm^3/g), the moles of adsorbed H_2 relative to the sample mass (i.e., moles in mmol/g), or the total system capacity, which is the ratio of the mass of adsorbed H_2 to the sum of the masses of adsorbed H_2 and the degassed sample (i.e., weight %).

The sample preparation, degassing, and measurement procedures are similar to those described for N_2 adsorption. The samples undergo degassing in a high vacuum environment (10-6 mbar) by heating them at a constant temperature of 250°C for 24 hours.

II.4.2. High Pressure Hydrogen Adsorption :

In this method, hydrogen gas (H_2) is used as the adsorption gas at applied pressures ranging from vacuum to 100 bar. The measurements are conducted at two different constant temperatures: 77.3 K (achieved by using liquid nitrogen to cool the system) and 298 K (ambient temperature measured with a water bath).

The amount of H_2 gas adsorbed on the surface of the solid is recorded by gradually increasing the pressure between 0 and 100 bar at the specified temperatures. Conversely, the desorption process is measured by gradually reducing the pressure. Isothermal H_2 adsorption/desorption curves are obtained, representing the relationship between the quantity of adsorbed/desorbed H_2 gas and the equilibrium pressure at constant temperature.

The resulting graph, known as the equivalent diagram, depicts the gravimetric H_2 capacity of the system. This refers to the mass of adsorbed H_2 relative to the sum of the masses of adsorbed H_2 and the degassed sample, expressed in weight percent (%wt), as a function of pressure (P) in bar.

The instrument used for these measurements can be described using the Sivert apparatus, as shown in Figure (6.2). The apparatus consists of two tanks: one for H_2 gas and one for the sample. These tanks are connected by an isolation valve.

By opening the valve, a small dose of H_2 gas is introduced into the sample container, and an equilibrium pressure is established between the two containers. The pressure drop in the tank directly correlates with the adsorption of H_2 gas by the sample. The amount of gas adsorbed can be calculated using the real or non-ideal gas law if the initial gas pressures and the system volume are known.

$$P \cdot V = n \cdot Z \cdot R \cdot T \tag{2.3}$$

The compressibility factor (Z) of a gas is related to the error correction factor (α) where:

Z is the compressibility factor of the gas

P is the pressure

V is the volume

n is the number of moles

R is the universal gas constant (8.314 J mol^{-1} K^{-1})

T is the temperature

The compressibility factor accounts for the deviation of a real gas from ideal gas behavior. It takes into consideration factors such as intermolecular interactions and non-ideal behavior at high pressures and low temperatures.

The error correction factor (α) is a dimensionless quantity that corrects for the non-ideal behavior of the gas and is related to the compressibility factor.

$$\alpha=\frac{(Z-1)}{P} \tag{2.4}$$

The α-factor corrects for the non-ideal behavior of the gas in the adsorption process. The values you mentioned are as follows:

For H2 at 77 K: α = 2.2 × 10-6 torr-1

For H2 at 87 K: α = 1.2 × 10-6 torr-1

For H2 at 298 K: α = 0.1 × 10-6 torr-1

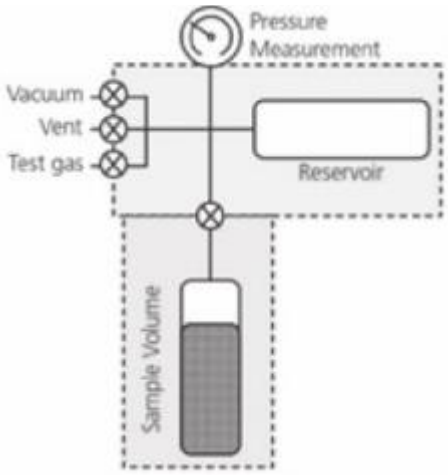

Figure(6.2): Functional principle of the Sivert apparatus [117].

The SETARAM Instrumentation Hy-Energy PCT Pro-2000 volumetric manual gas absorption system was used for measuring H_2 adsorption. Here are the key steps and procedures followed:

1. Sample Preparation: A 100-120 mg sample of each material was placed in a metallic face seal called a VCR®. The weight of the empty recorder and the sample was measured to determine the weight of the uncarbonated sample. A non-porous glass cylinder spacer was inserted into the VCR to minimize its volume.

2. Degassing: The samples were degassed under high vacuum (10^{-7} mbar) with constant heating at 250°C for 24 hours. This process helps remove any adsorbed gases or impurities from the sample.

3. Volume Calibration: Prior to H_2 adsorption measurements, volume calibration was performed using helium gas. This calibration procedure determines the free volumes within the cell and involves five helium adsorption/desorption cycles at three different temperatures: device operating temperature (303 K), room temperature (298 K), and liquid nitrogen boiling point (77 K).

4. H_2 Adsorption Measurements: The VCR containing the sample was immersed in a liquid nitrogen bath at 77.3 K or a water bath at 298 K, depending on the desired temperature. The HyData software allowed for configuring experimental parameters and monitoring the entire procedure.

- Dose Pressure and Equilibrium Time: The dose pressure was set to 2 bar, and the equilibrium time at each point was set to 5 minutes for measurements at 77 K and 7 minutes for measurements at 298 K.

- Pressure Range: The pressure applied during the experiments varied from vacuum (10^{-7} mbar) to approximately 100 bar.

- Venting: Four main venting steps occurred for each sample during the high-pressure experiments. The first evacuation took place after inserting the VCR into the instrument, the second after volume calibration, and the last two after each measurement at 77 K and 298 K.

5. Mass Measurement: At the end of the measurements, the sample was removed from the apparatus, and the degassed mass of the sample was weighed to determine any changes in mass due to adsorbed H_2.

6. Mathematical Corrections: Mathematical corrections were applied to the results to minimize experimental errors and ensure accurate measurements.

Figure(7.2): SETARAM Hy-Energy PCT Pro 2000 High Pressure Gas Absorption Analyzer [118].

II.5. Hydrogen storage in strained graphene :

II_5_1 Studies on H_2 storage in Graphene

The hydrogen adsorption properties of graphene using a 4x4x1 supercell structure with 32 carbon atoms.

After obtaining the relaxed structure of graphene, you proceeded to place the first H_2 molecule at different positions on the graphene surface for further investigation. These positions include:

Center of the Hexagon (C): The H_2 molecule is positioned directly above the center of a hexagon formed by the carbon atoms in the graphene lattice.

Center of the Bridge Edge (B): The H_2 molecule is placed over the center of the bridge edge, which connects two neighboring hexagons in the graphene lattice.

Top Carbon Atom (T): The H_2 molecule is positioned directly above the top carbon atom of the graphene structure. as shown in Figure(8.2) .

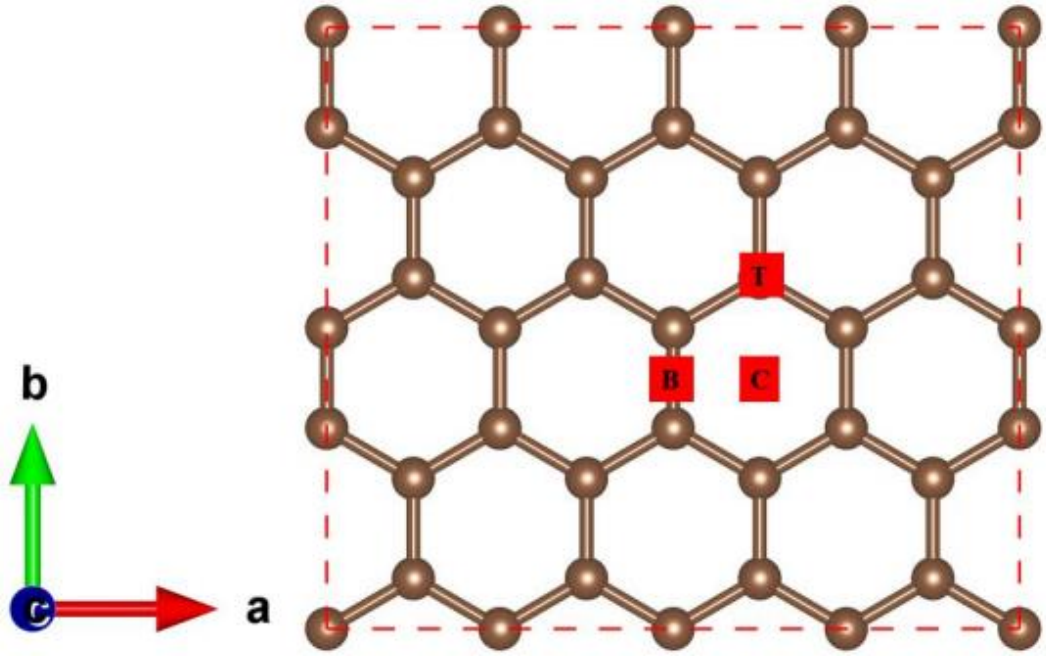

Figure(8.2) shows the optimized structure of a 4x4x1 graphene supercell. The vertices of the hexagons within the graphene lattice are represented by C, indicating the center of the hexagon. The edges of the bridge connecting two hexagons are represented by B, indicating the center of the bridge edge. The vertices of the carbon atoms within the graphene lattice are represented by T, indicating the top carbon atom of the graphene sites.[128]

The hydrogen molecule is held about 2 Å by the graphene sheet before relaxing. To account for the influence of weak van der Waals interactions, we improved the GGA exchange correlation level results by including Grimme's DFT-D2-type dispersion corrections. The adsorption energy of the first H2 contained in the C, B and T sites was found to be -0.11 eV, -0.10 eV and -0.or 10 eV. Because the binding energy of a hydrogen molecule bound to graphene does not meet the DOE-US criteria, pure graphene is not suitable for storing hydrogen under ambient conditions. Another notable point is that if we place one hydrogen molecule in front of the 4*4*1 graphene supercell and one hydrogen molecule behind, the system's hydrogen uptake would be 0.8%, which is well below 6.5%.Therefore we place a hydrogen molecule on each complete hexagon . Thus, 10 H_2 molecules can be stored on the

front of the graph and likewise 10 H_2 molecules can be stored on the back. The hydrogen consumption for such a system will be 9.4%, well above the DOE limit of 6.5%. We therefore calculated the average adsorption energy of 10 H_2 molecules located over the 10 hexagons of a 4*4*1 graphene monolayer. The average adsorption energy for 10 H_2 molecules was -0.09 eV/H_2 calculated using the theoretical level GGA+DFT-D2, which is not good enough for practical purposes since this adsorption energy corresponds to a desorption temperature lower than ambient temperature. Cabria and Lopez [119] reported that the average binding energy ofhydrogen molecules bound to graphene and a nanotube is 80–90 meV/H_2, which is very similar to our study.Constance et al. [120] reported a binding energy of 0.1 eV for an H_2 molecule attached to a pristine graphene surface, which accounts for scattering corrections using the DFT-D scheme.

To improve the mean H_2 adsorption energy, we systematically applied a biaxial compressive strain to a graphene supercell by reducing the graphene lattice parameters. At 5% biaxial compressive stress, we report that the mean adsorption energy is 10H_2 -0 .29 eV/H_2, while it is -0.42 eV/H_2 at 6% of biaxial compressive strain. The average desorption temperatures of the 10 H2 molecules attached to the graphene corresponding to binding energy -0.29 eV/H_2 and -0.42 eV/H_2, considering hydrogen molecules at ambient pressure, are found to be 371 K and 538 K, respectively.We used the Van't Hoff formula [121] to calculate the mean desorption temperature defined by the equation:

$$T_d = \left(\frac{E_b}{K_B}\right)\left(\frac{\Delta S}{R} - \ln P\right)^{-1} \quad (2.5)$$

Here, T_d and E_b are mean desorption temperature and adsorption energy, respectively. k_B, Δs, R and P are the Boltzmann constant, the entropy change for H_2 in the transition from the gaseous to the liquid phase [121], the gas constant and the atmospheric pressure.

This means that if we apply a compressive strain of 5% to 6% to single-layer graphene (4*4 supercells), the average adsorption energy of hydrogen molecules ranges from -0.2 eV/H_2 to -0.4 eV /H_2, suggesting the H_2 adsorption process is reversible.The gravimetric mass percent hydrogen for this composition is 9.4% as previously described. The optimized structure of graphene + 10 H_2 at 6% biaxial compressive stress is shown in Figure(9.2).

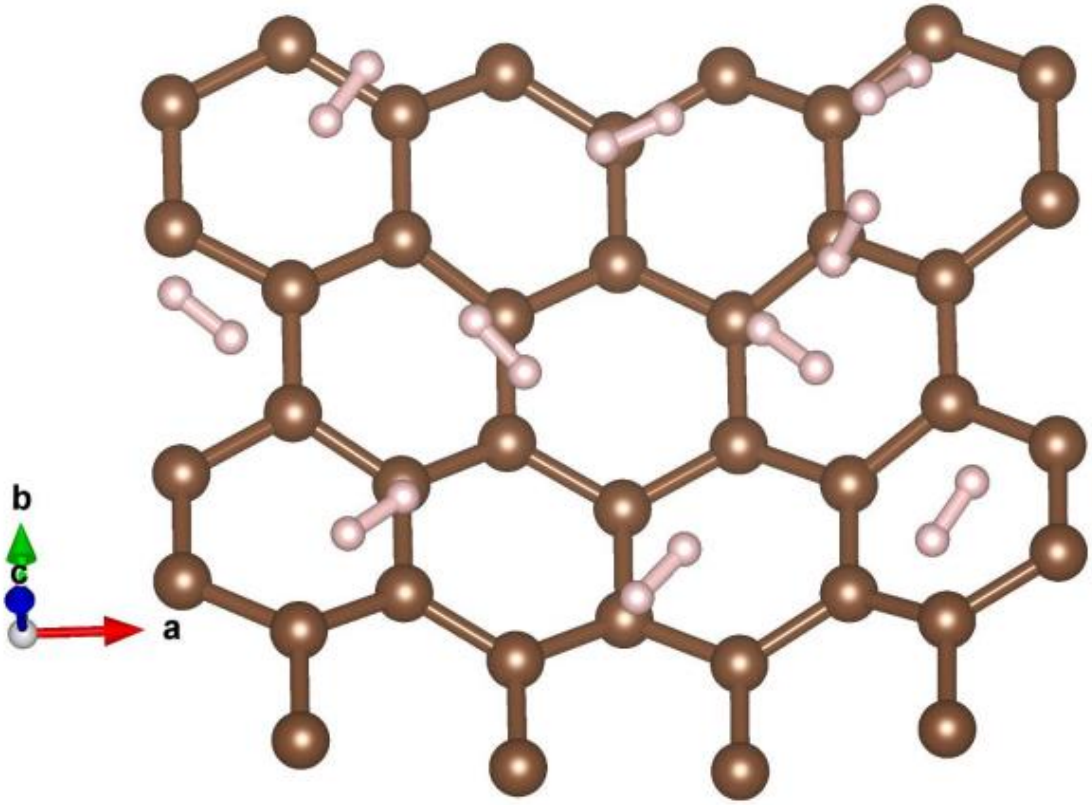

Figure(9.2) Optimized graphene structure + 10 H_2 at 6% biaxial compression[128]

The systematic improvement in the mean adsorption energy of H2 under biaxial compressive stress is shown in Table (1.2)

Biaxial comprehensive strain(%)	Average binding energy of H_2 (eV/H_2) GGA+DFT-D2
0	-0.09
2	-0.12
3	-0.13
4	-0.19
5	-0.29
6	-0.42

Table (1.2). The systematic improvement in the average adsorption energy of hydrogen molecules attached to a graphene monolayer by increasing the biaxial compression strain.[128]

Next, we studied the mechanism of orbital charge flow between the graphene monolayer and the attached H2 molecules by using the partial density of states of the C2(s and p) orbitals of graphene and the H1s + 10H_2 orbitals of graphene for unstressed graphene and graphene recorded at 6%. biaxial compressive stress, as shown in Figure(10.2) We find that there is some enhancement of the C2p orbital states near the Fermi level of the stretched graphene compared to the unstretched structure, as shown in Figure. (10.2).(a and b). Some depletion of the near-Fermi energy states of the H-1 orbit of stretched graphene relative to unstretched graphene is also observed, as shown in Fig.(10.2) (c and d). This means that in the graphene + 10 H_2 composition, there are higher charge transfers from the H-1s orbital to the C-2p orbitals of the graphene + 10 H_2 composition, which is responsible for the energetic strengthening of the bonding of hydrogen molecules bound to the graphene monolayer .

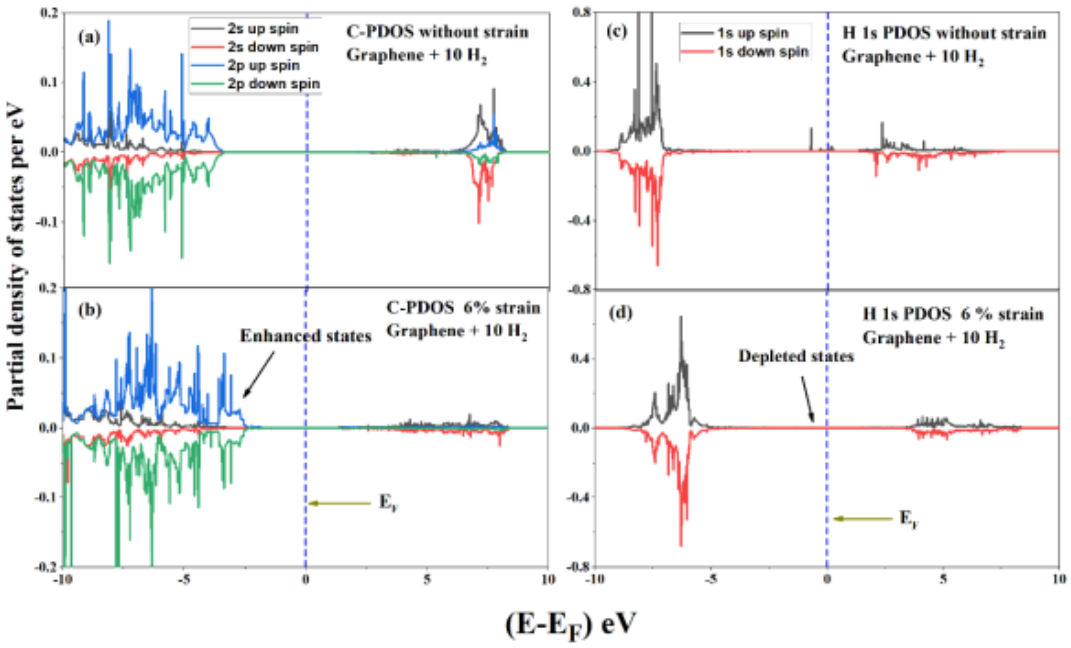

Figure(10.2) Partial density of states of (a) C-2 orbitals (s and p) for unstrained graphene + 10 H_2, (b) C-2 orbitals (s and p) of graphene + 10 H_2 at 6% biaxial compression strain, (c) H1 unstressed graphene orbital + 10 H_2, d) H-1 graphene orbital + 10 H_2 at 6% biaxial compressive stress.[128]

In order to verify the charge transfer process, we plotted the difference in surface charge density of graphene composition +10H_2 for virgin graphene and graphene strained at 6% compressive strain as in Fig. (11.2). Here Figure (11.2)a) shows the difference in of charge density between ρ(graphene + 10 H_2) – ρ(graphene) for unstressed graphene, while Figure (11.2)(b) shows the difference in charge density between ρ(graphene + 10 H_2) – ρ(graphene) for graphene with 6% biaxial Compressive stress of.These plots follow the B-G-R color scheme, with red around hydrogen molecules indicating an area of pressure drop, while green and blue around graphene carbon atoms indicate decreasing areas of pressure drop and load accumulation, respectively.

The isosurface value for Figure (11.2) (a and b) is 0.080e.

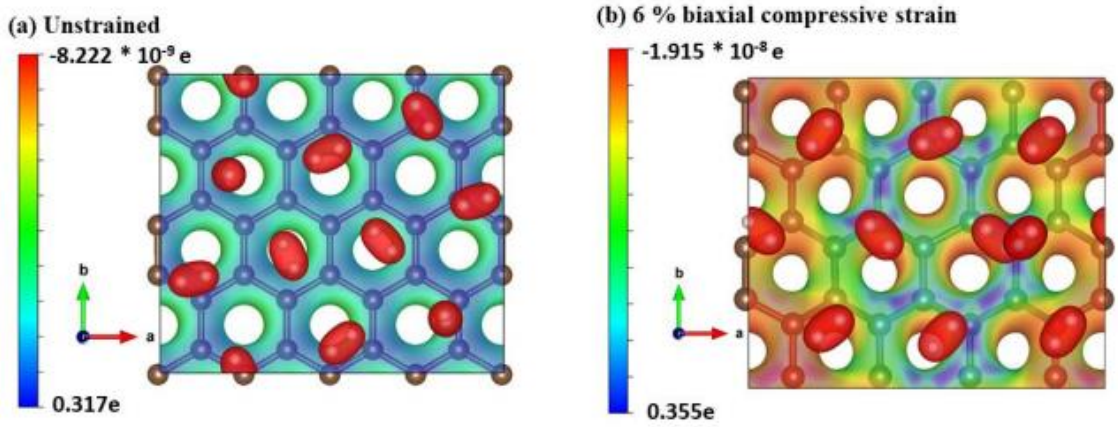

Figure(11.2) : Plots of surface charge density ρ(graphene + 10 H_2) - ρ(graphene) (a) for the unstressed composition (b) for the stretched composition with 6% elongation in biaxial compression. The graphs follow the B-G-R color model for the isoarea value 0.080e[128]

from Figure(11.2)a) shows that the charge was evenly distributed in the graphene monolayer when H_2 molecules were attached to the unstressed graphene framework, which redistributes between the graphene carbon atoms at 6% biaxial compressive stress, as shown in Figure(11.2) .

Furthermore, the blue colored region is more intense in the strained structure than in the unstressed structure, which means that the charge transfer from H_2 to the graphene increases with compression strain. This is one of the reasons for improving the binding energy of hydrogen molecules bound to the compressed graphene monolayer. Due to the systematic lowering of the lattice parameters with increasing biaxial compressive stress, the C-C bond lengths in graphene decrease and thus the electron density around the C-C bonds increases, which is also responsible for the strong binding of hydrogen molecules to dense singles. -Graphene layer.

II.5.2.Analysis of the quantum and classical pathways for hydrogen diffusion, recombination, and desorption :

Table(2.2) shows the high crossover temperature for amount tunnelling and the large effective hedge reduction due to deep tunnelling, showing that H prolixity and recombination processes are quantum mechanical in nature. Carbon tunnelling is also observed, albeit to a limited extent indeed in the deep tunnelling regime.

Figure(12.2) : shows the apparent deviations of the instantaneous traces from the MEP, indicating strong shear effects for the H recombination traces on graphs.

Figure(13.2) shows that strong angular shear effects also exist in graphene H scattering, but not so much in H desorption/adsorption processes.For the desorption process, there is no tunneling path below 0.79 eV, which corresponds to the energy difference between the initial and final states. Tunnel construction cannot violate the law of conservation of energy.

Figure(14.2) : shows that deep tunneling moments take narrower trajectories than MEPs, particularly for the ortho mechanism, which has the strongest corner cutting effect of the three. We also carefully verified that the orthopath was not

Table(2.2) . Characteristic quantities of quantum tunneling for the diffusion, recombination, and desorption processes of H_2 on graphene. Tc is the transition temperature [123, 124] for the quantum tunneling effect.ΔE_t is the effective reduction in activation energy by tunneling, defined by the ratio between the instantaneous velocity (k_{inst}) and the Eyring theory transient velocity (TST) (k_{TST}):[129]

$$\frac{1}{\beta} \ln \frac{k_{inst}}{k_{TST}} . (\beta = 1/ k_B T). \quad (2.6)$$

The values of ΔE_t presented here are calculated for the deep tunneling cases: at 150 K for the formation of ortho-H_2 and at 100 K for the other processes. The percentage of ΔE_t with respect to the classical potential barrier is given in brackets.

The tunneling distance ofcarbon atoms refers to the average distance that the C atoms (on which the H atoms are adsorbed) travel (in one direction) along the instantaneous path calculated for deep tunneling.

The brackets indicate the percentage of carbon tunnel distance compared to the calculated minimum energy path (MEP) distance.they have a classic "symmetrical" transition state in which the two H atoms move synchronously as if on an instantaneous orbit.

Our calculations of the climbing picture's flexband found no such path, although they made an initial "symmetrical" assumption. By taking the highest instantaneous energy for the 600K orthopath, where both H atoms are at the same height above the surface, and doing a frequency analysis, we found that this configuration has two imaginary frequencies [129]

In fact, the second imaginary mode (whose frequency is ~750i cm^{-1}) represents the asymmetric stretching of the two C-H bonds. A relaxation in this mode would "break the symmetry" and result in two H atoms at different heights.

Process	T_c(K)	ΔE_t(eV)	Carbon tunnelling distance(Å)
Ortho	607	1.550(77%)	0.15(20%)
Meta	413	0.250(49%)	0.09(13%)
Para	425	0.574(57%)	0.11(15%)
Diffusion	286	0.453(51%)	0.25(32%)
Desorption	199	0.085(12%)	0.13(25%)

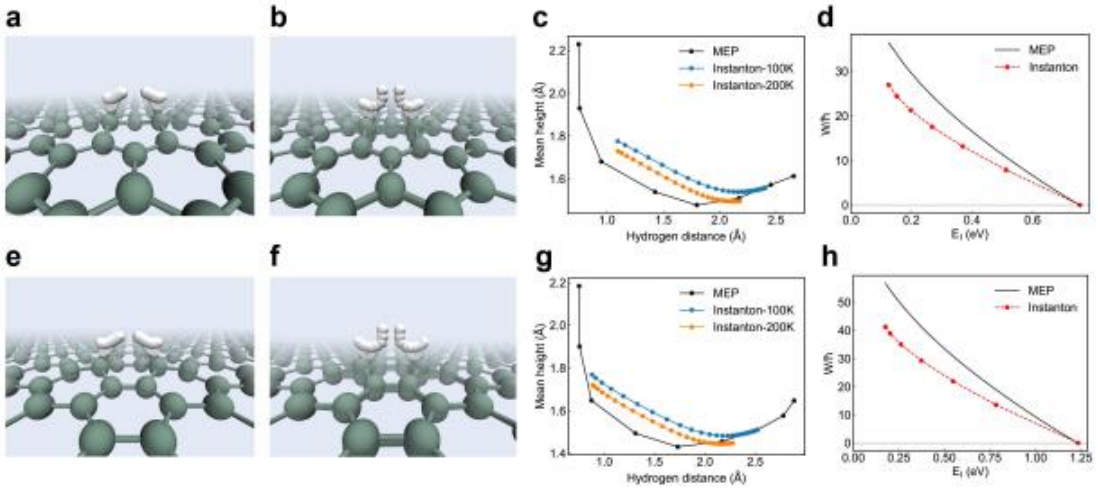

Figure (12.2) : Comparison of instantaneous and classical MEP trajectories for H2 formation in meta and para configurations. Instanton trajectory geometry at 100 K (a) and classical MEP (b) for the formation of H2 in metaconfiguration. (c) 2D representation (with the average height of the two H atoms and the distance between them) of the classical MEP and instanton pathways at different temperatures. (d) Short-term comparison calculated along the MEP trajectories and instantaneously at different energies. (e)-(h) are the same as (a)-(d) but for H2 evolution in the para configuration at 100 K [129]

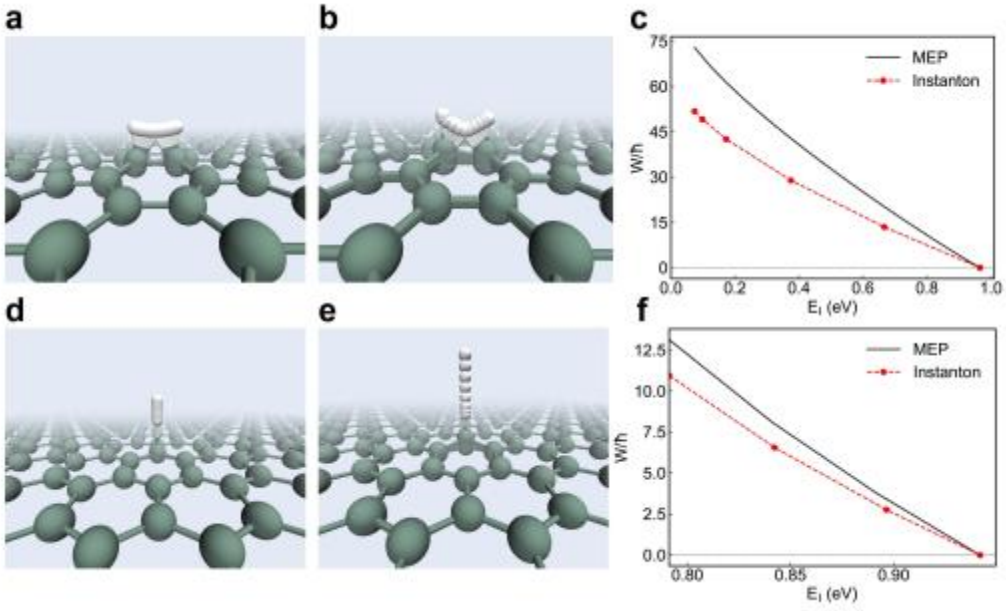

Figure(13.2) : Same as Figure(12.2)for H diffusion (a-c) and desorption (d-f) processes[129]

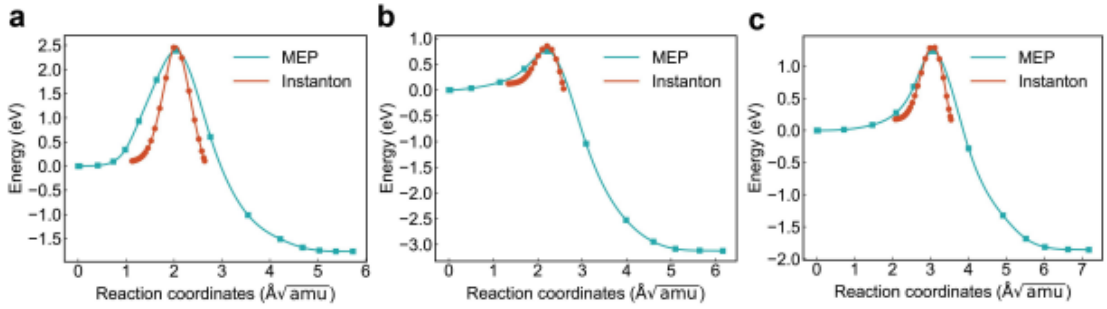

Figure (14.2) : Comparison of MEP and instanton plotted along their respective mass-weighted reaction coordinates for H2 formation in (a) ortho configuration at 150 K, (b) meta configuration at 100 K, and (c) para configuration at 100 K. The coordinated response for the moment is shifted to align with the highest MEP energy point[129]

III.1.Introduction

The magnetic field created by the geometric patterns on the graphene surface will affect hydrogen's magnetic properties. The energy involved in this interaction is crucial for stabilizing or storing hydrogen molecules. Conversely, when hydrogen molecules need to be released for use, the opposing energy comes into play. It's important to understand that the relationship between a magnetic moment and a magnetic field is determined by a constant factor. By studying the variations in the magnetic field caused by different geometric shapes, we can gain a better understanding of the necessary modifications that must be made to the graphene surface.

To investigate the interaction between different geometric shapes and the storage capacity of hydrogen, we utilized the Mathematica program to simulate this phenomenon. Our objective was to extract valuable insights regarding the specific geometry that enables the highest possible storage capacity.

III.2. The correlation between reaction energy and geometry:

The given equations represent the pseudomagnetic field components in polar coordinates. Let's calculate the pseudomagnetic field (Bs) using the provided expressions [130]:

- $A_r = \beta a\left(\frac{\partial u_r}{\partial r} - \frac{u_r}{r} - \left(\frac{1}{r}\right)\left(\frac{\partial u_\theta}{\partial \theta}\right)\right)\cos(3\theta) + [\left(-\frac{1}{r}\right)\left(\frac{\partial u_r}{\partial \theta}\right) + \frac{u_\theta}{r} - \left(\frac{\partial u_\theta}{\partial r}\right)]\sin(3\theta)$
- $A_\theta = \beta a\left[-\left(\frac{\partial u_\theta}{\partial r}\right) + \frac{u_\theta}{r} - \left(\frac{1}{r}\right)\left(\frac{\partial u_r}{\partial \theta}\right)\right)]\cos(3\theta) + [\,(1/r)(\partial u_\theta/\partial\theta) + u_r/r - (\partial u_r/\partial r)\sin(3\theta)]$

Now we'll differentiate A_θ with respect to r and A_r with respect to θ to obtain the derivatives:

- $\partial A_\theta/\partial r = \beta a\,[(\partial^2 u_\theta/\partial r^2) - (\partial u_\theta/\partial r)/r - (1/r)(\partial^2 u_r/\partial\theta\,\partial r)]\cos(3\theta) + [(1/r)(\partial^2 u_\theta/\partial\theta\,\partial r) + (\partial u_r/\partial\theta) - (\partial^2 u_\theta/\partial r^2)]\sin(3\theta)$
- $\partial A_r/\partial\theta = \beta a\,[-(\partial^2 u_r/\partial\theta^2) + (\partial u_r/\partial\theta)/r + (1/r)(\partial^2 u_\theta/\partial r\,\partial\theta)]\cos(3\theta) + [-(1/r)(\partial^2 u_r/\partial\theta^2) - (\partial u_\theta/\partial\theta) + (\partial^2 u_r/\partial r\,\partial\theta)]\sin(3\theta)$

- $B_s = (1/r)\,(\partial A_r/\partial\theta) - (\partial A_\theta/\partial r) - A_\theta/r$

Now, we can substitute these derivatives into the pseudomagnetic field expression. Substituting the derivatives we calculated earlier:

$$\begin{aligned} B_s = \beta a\,(1/r)\,\{&[(\partial^2 u_\theta/\partial r^2) - (\partial u_\theta/\partial r)/r - (1/r)(\partial^2 u_r/\partial\theta\,\partial r)] - [-(\partial^2 u_r/\partial\theta^2) \\ &+ (\partial u_r/\partial\theta)/r + (1/r)(\partial^2 u_\theta/\partial r\,\partial\theta)]\}\cos(3\theta) \\ &+ (1/r)\,\{[(1/r)(\partial^2 u_\theta/\partial\theta\,\partial r) + (\partial u_r/\partial\theta) - (\partial^2 u_\theta/\partial r^2)] \\ &- [-(1/r)(\partial^2 u_r/\partial\theta^2) - (\partial u_\theta/\partial\theta) + (\partial^2 u_r/\partial r\,\partial\theta)]\}\sin(3\theta) - A_\theta/r \end{aligned}$$

where:

• β and a are a constants,

• u_r is the velocity component in the radial direction,

• u_θ is the velocity component in the azimuthal direction,

• r is the radial distance from the origin,

$$\begin{aligned} B_s = {} & \beta a\,(1/r)\,\{[(\partial^2 u_\theta/\partial r^2) - (\partial u_\theta/\partial r)/r - (1/r)(\partial^2 u_r/\partial\theta\,\partial r) + (\partial^2 u_r ur/\partial\theta \\ & - (\partial u_r/\partial\theta)/r - (1/r)(\partial^2 u_\theta/\partial r\,\partial\theta)]\}\cos(3\theta) \\ & + (1/r)\,\{[(1/r)(\partial^2 u_\theta/\partial\theta\;\partial r) + (\partial u_r/\partial\theta) - (\partial^2 u_\theta/\partial r^2) \\ & + (1/r)(\partial^2 u_r/\partial\theta^2) + (\partial u_\theta/\partial\theta) - (\partial^2 u_r/\partial r\,\partial\theta)\,]\}\sin(3\theta) \\ & - \{\beta a\,[-(\partial^2 u_r/\partial\theta^2) + (\partial u_r/\partial\theta)/r + (1/r)(\partial^2 u_\theta/\partial r\,\partial\theta)]\cos(3\theta) \\ & + [-(1/r)(\partial^2 u_r/\partial\theta^2) - (\partial u_\theta/\partial\theta) + (\partial^2 u_r/\partial r\,\partial\theta)]\sin(3\theta)\}/r \end{aligned}$$

This expression represents the complete formula for the pseudomagnetic field Bs in terms of the given functions $u_\theta = f(r,\theta)$ and $u_r = g(r,\theta)$. To find functions $u_\theta = f(r,\theta)$ and $u_r = g(r,\theta)$ that minimize the pseudomagnetic field B_s, where $f(r,\theta)$ and $g(r,\theta)$ are not constants, we can utilize variational methods or optimization techniques. The goal is to find functions that satisfy the conditions for minimum values of B_s. Here's a general approach to finding such functions:

1. Define a functional $J(u_\theta, u_r)$ that represents the pseudomagnetic field B_s in terms of u_θ and u_r. This functional should incorporate the given expression for B_s.

2. Use optimization techniques such as the calculus of variations or numerical optimization methods to minimize the functional J. This involves finding the functions uθ and ur that minimize J subject to certain constraints, if any.

3. Apply the necessary boundary conditions or constraints to ensure the validity of the solutions.

It's important to note that finding the exact functions that yield the minimum values of B_s can be a complex task and may require advanced mathematical techniques. The specific approach and techniques used will depend on the nature of the problem and the constraints involved.

If you have a specific problem or constraints in mind, providing more details would allow for a more tailored and specific approach to finding the functions u_θ and u_r that minimize B_s.

To find functions $u_\theta = f(r,\theta)$ and $u_r = g(r,\theta)$ that minimize the pseudomagnetic field B_s, we can utilize variational methods. The goal is to find the functions that minimize a certain functional by varying them.

III.2.1. The variational approach:

1.Define the functional $J(u_\theta, u_r)$ that represents the pseudomagnetic field B_s in terms of u_θ and u_r. We already have the expression for B_s, so we can define J as:

$$J(u\theta, ur) = \int (Bs)^2 dA$$

Where dA represents the area element in polar coordinates.

2.Apply the variational principle by finding the stationary points of J. This means finding the functions $u_\theta(r,\theta)$ and $u_r(r,\theta)$ that make the functional J stationary (minimum or maximum). We can do this by varying u_θ and u_r and setting the variation of J to zero.

$$\delta J = 0$$

3.Calculate the variation of J. Take the variation of J with respect to u_θ and u_r, and set it equal to zero:

$$\delta J = \int 2(Bs)(\delta Bs)dA = 0$$

4.Express the variation of Bs in terms of the variations of u_θ and u_r. This requires expanding the expression for Bs and taking the variations of u_θ and u_r with respect to r and θ.

5.Apply integration by parts and use appropriate boundary conditions to simplify the variation expression.

6.Solve the resulting equations to find the functions $u_\theta(r,\theta)$ and $u_r(r,\theta)$ that satisfy the variation condition and minimize the pseudomagnetic field Bs.

Note that this variational approach can be mathematically involved and may require numerical methods or additional simplifications depending on the specific problem and boundary conditions. The exact solution will depend on the specific form of the functions $f(r,\theta)$ and $g(r,\theta)$ as well as the constraints and boundary conditions imposed on the system. If we have specific boundary conditions or constraints in mind, providing them would allow for a more detailed analysis and a more specific approach to finding the functions u_θ and u_r that minimize Bs.

III.3.Results :

In our study, we investigated the impact of certain geometric distortions on the surface of graphene using the following equations: $x+y$, x^2, x^2+y^2, x^2-y^2, and x^2-y^2. We successfully obtained satisfactory outcomes that describe the influence of the phenomenon generating powerful magnetic fields on the capacity of hydrogen storage.

III.3.1.Geometric distortion x^2:

The basic geometric distortion $\boldsymbol{x^2}$ is a controlled deformation that can be easily manipulated by humans. By analyzing the following illustrations, we can infer how the interaction energy is distributed across the surface of two-dimensional graphene as a result of this particular geometric deformation.

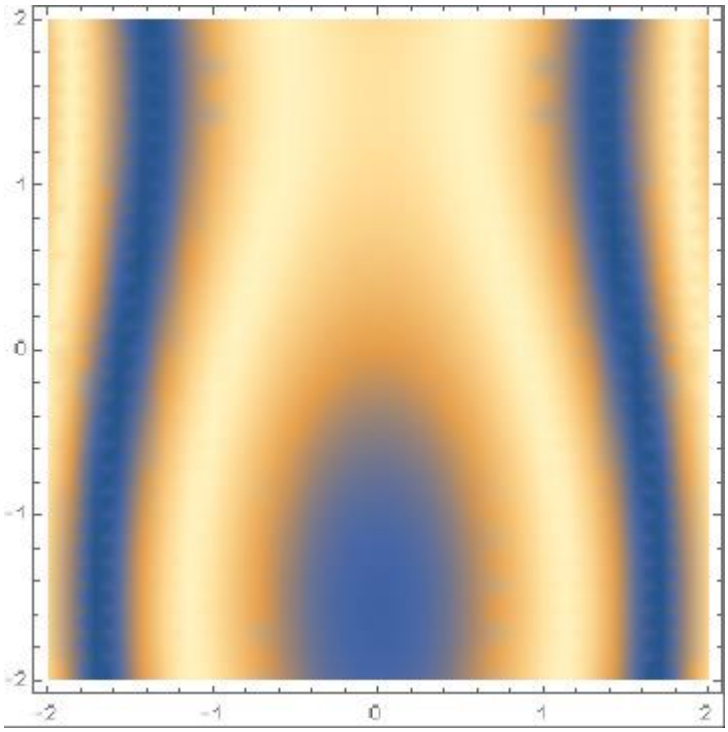

Figure (1.3): depict the alterations in energy distribution caused by the interaction between the magnetic moment of hydrogen atoms and the magnetic field generated due to the x^2 geometric deformation pattern

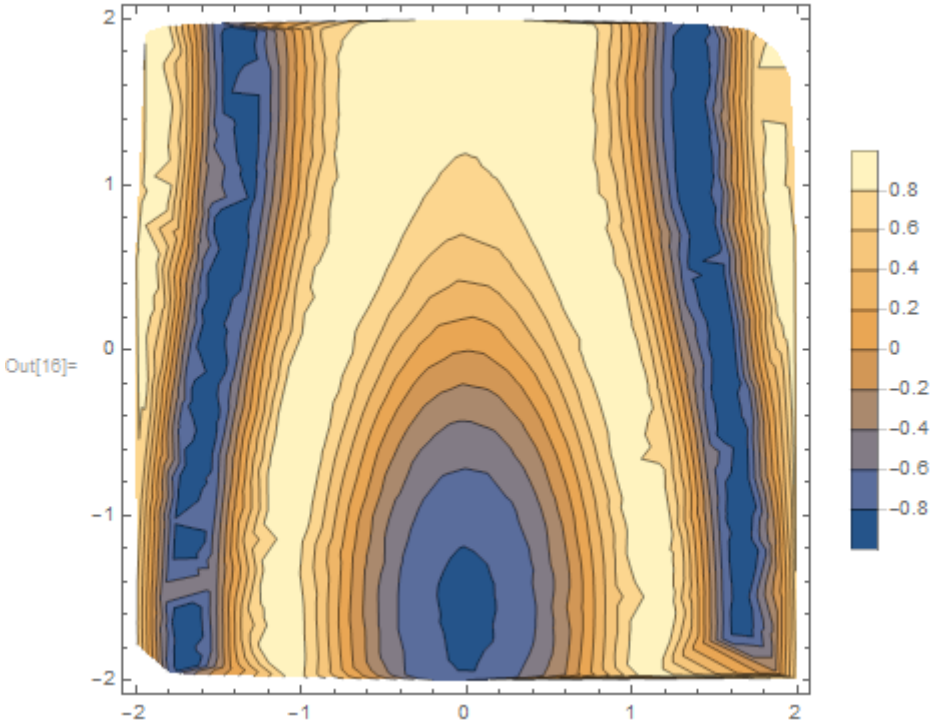

Figures (2-3) illustrate the variations in isoenergy lines arising from the interplay between the magnetic moment of hydrogen atoms and the magnetic field generated by the geometric deformation characterized by the x^2 pattern.

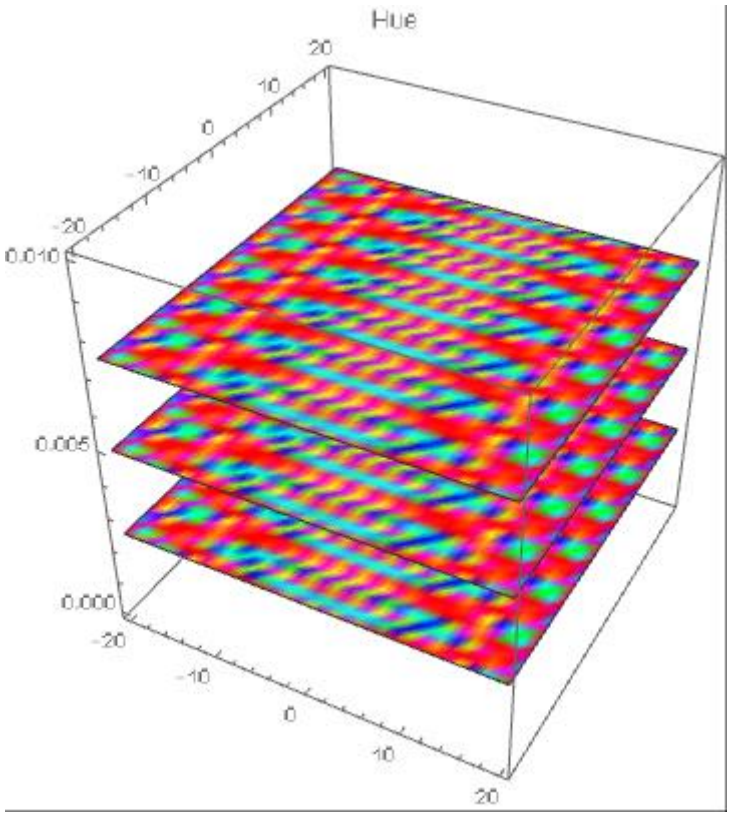

Figure (3-3) display three cross-sections demonstrating the systematic distribution of energy in specific confined regions. This distribution arises from the interplay between the magnetic moment of hydrogen atoms and the magnetic field generated due to the geometric deformation characterized by the x^2 pattern.

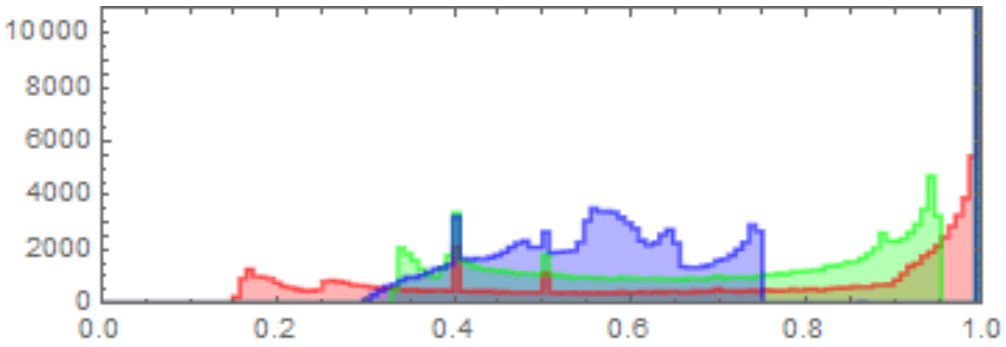

Figure (4-3) depict the distribution of 10000 hydrogen molecules on a surface consisting of a certain number of moles of graphene atoms. The blue regions represent hydrogen molecules that adhere to the surface, the green regions indicate semi-free hydrogen molecules, and the red regions indicate hydrogen molecules that exhibit strong interaction with the graphene surface.

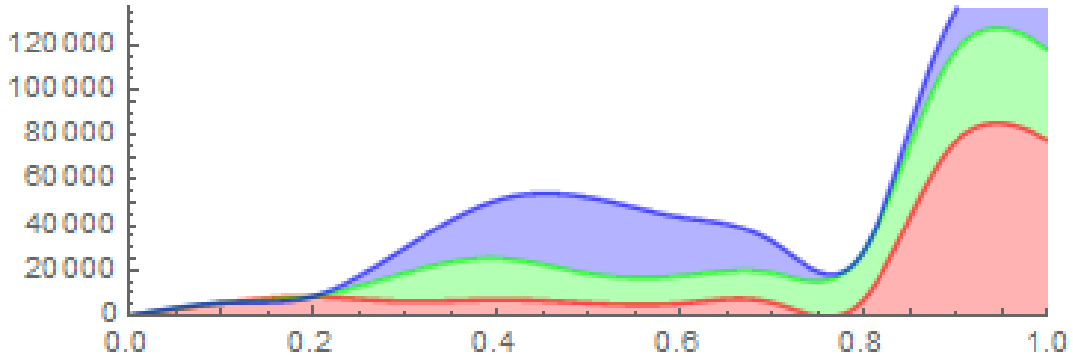

Figure (5-3) demonstrate the transformation of the preceding figure into a clearer representation when the number of hydrogen molecules is increased to 120,000 molecules.

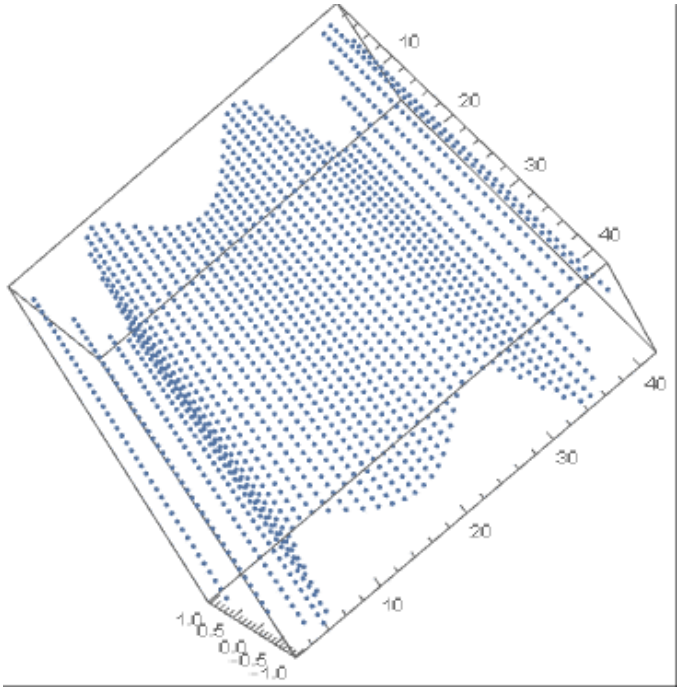

Figure (6-3) provide a simulated depiction of the distribution of hydrogen molecules across the surface of the geometric deformation.

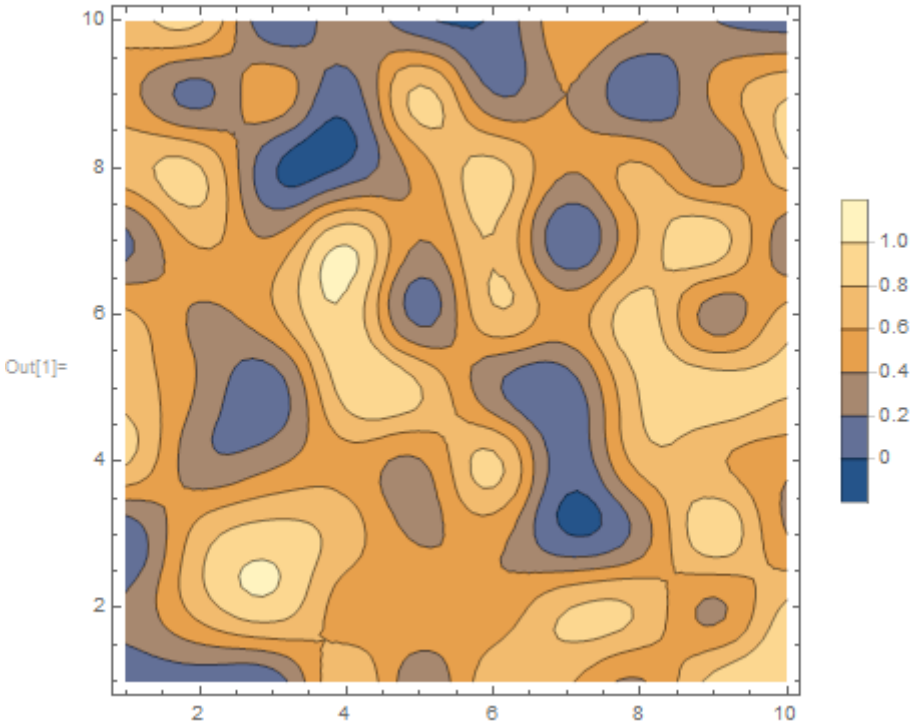

Figure (7-3) present a simulation illustrating the distribution of reciprocal pressure across the regions generated by geometric deformations. This distribution is calculated in terms of free units.

III.3.2. Geometric distortion$x^2 + y^2$:

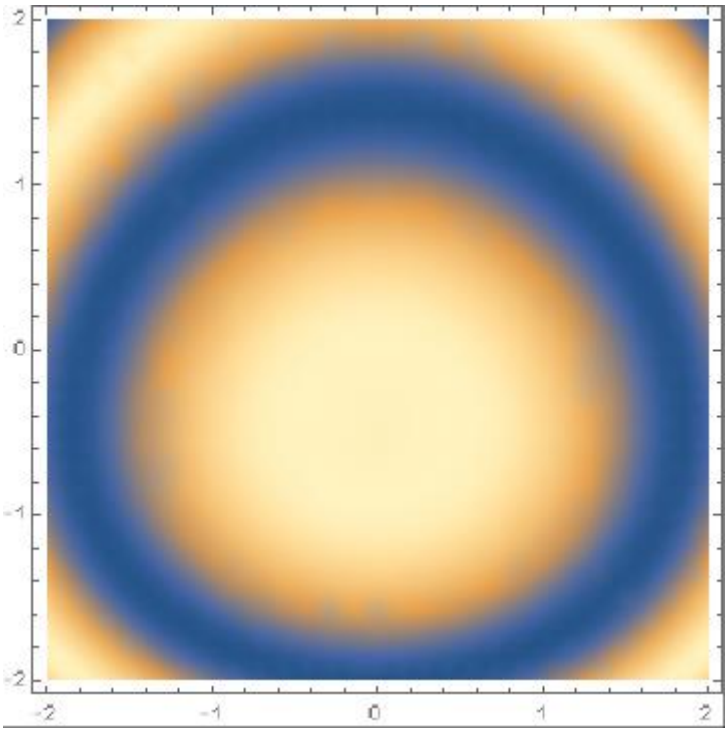

Figure (8.3): depict the alterations in energy distribution caused by the interaction between the magnetic moment of hydrogen atoms and the magnetic field generated due to the $x^2 + y^2$ geometric deformation pattern

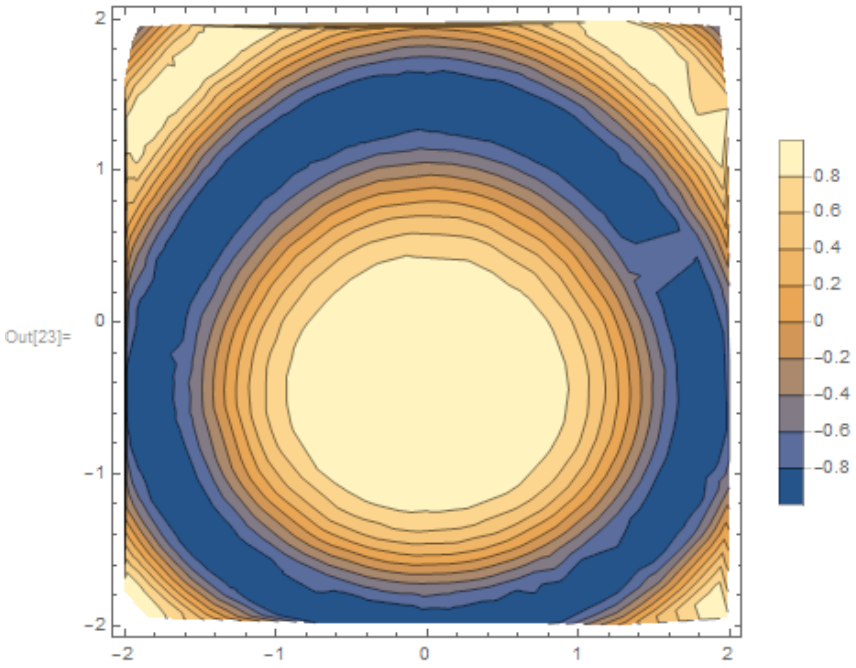

Figure (9-3) illustrate the variations in isoenergy lines arising from the interplay between the magnetic moment of hydrogen atoms and the magnetic field generated by the geometric deformation characterized by the $x^2 + y^2$pattern.

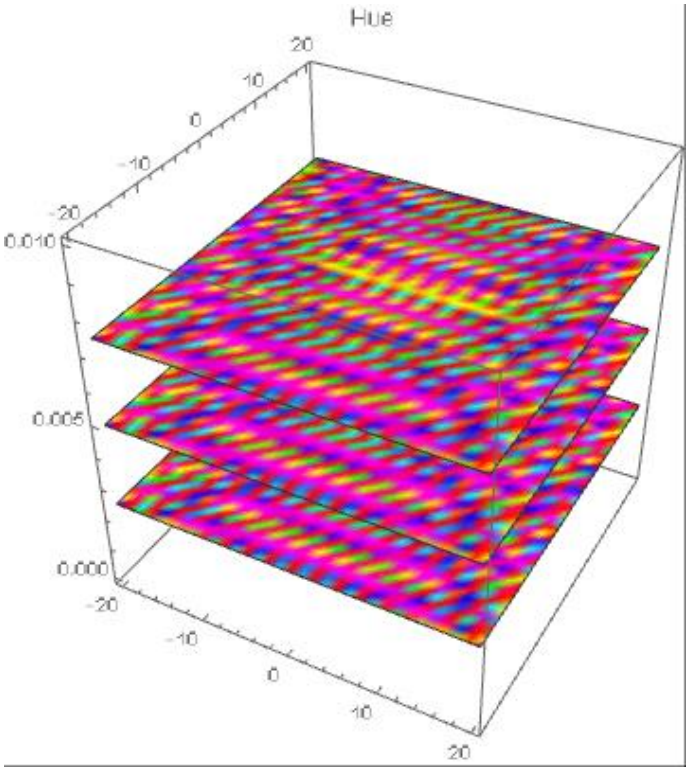

Figure (10-3) display three cross-sections demonstrating the systematic distribution of energy in specific confined regions. This distribution arises from the interplay between the magnetic

moment of hydrogen atoms and the magnetic field generated due to the geometric deformation characterized by the $x^2 + y^2$pattern.

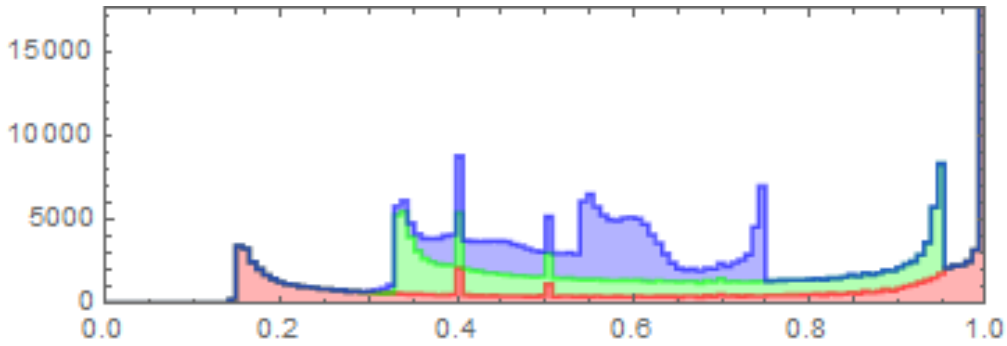

Figure (11-3) depict the distribution of 15000 hydrogen molecules on a surface consisting of a certain number of moles of graphene atoms. The blue regions represent hydrogen molecules that adhere to the surface, the green regions indicate semi-free hydrogen molecules, and the red regions indicate hydrogen molecules that exhibit strong interaction with the graphene surface.

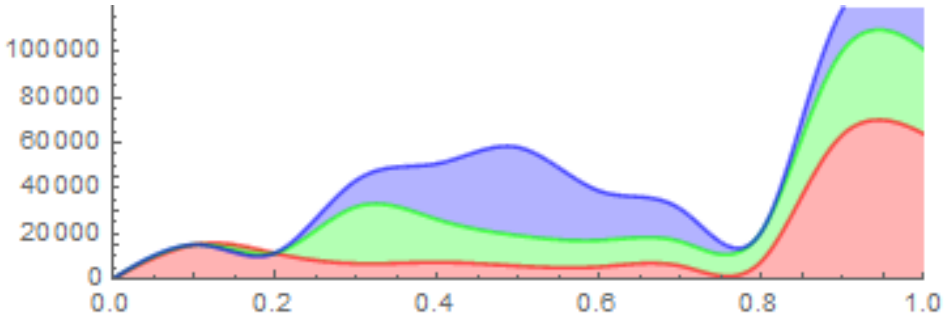

Figure (12-3) demonstrate the transformation of the preceding figure into a clearer representation when the number of hydrogen molecules is increased to 100,000 molecules.

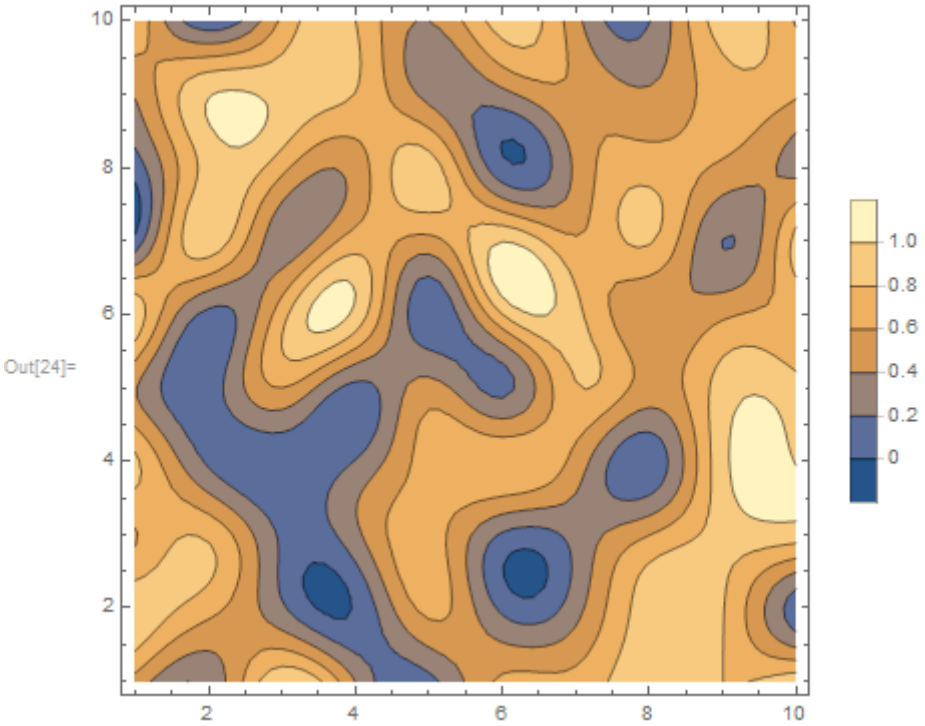

Figure (13-3) present a simulation illustrating the distribution of reciprocal pressure across the regions generated by geometric deformations. This distribution is calculated in terms of free units.

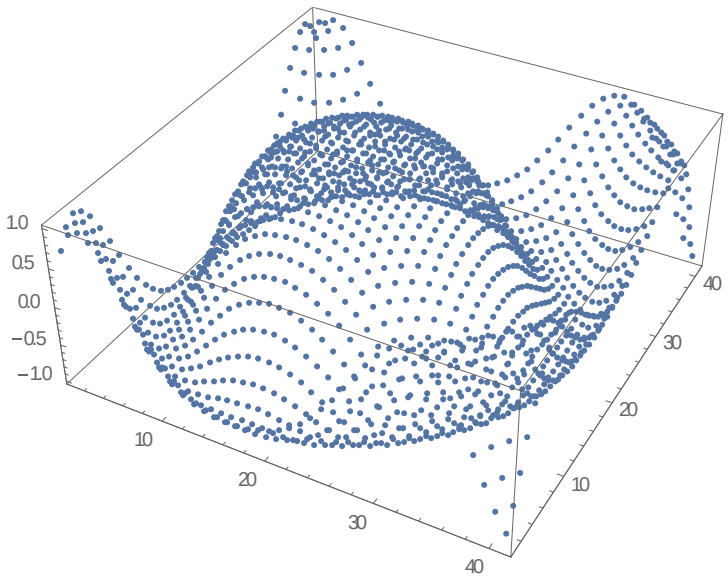

Figure (14-3) provide a simulated depiction of the distribution of hydrogen molecules across the surface of the geometric deformation.

III.3.3. Geometric distortion$x^2 - y^2$:

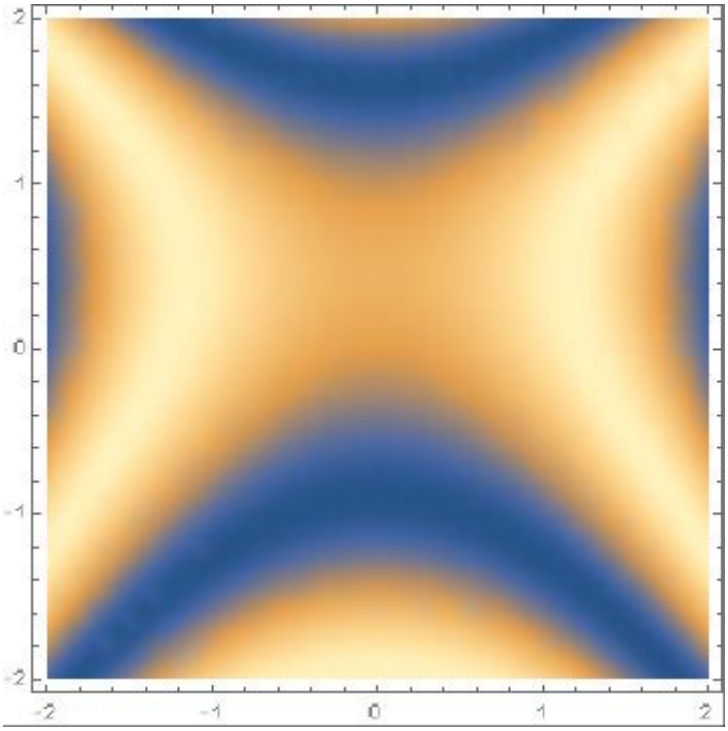

Figure (15.3): depict the alterations in energy distribution caused by the interaction between the magnetic moment of hydrogen atoms and the magnetic field generated due to the $x^2 - y^2$ geometric deformation pattern

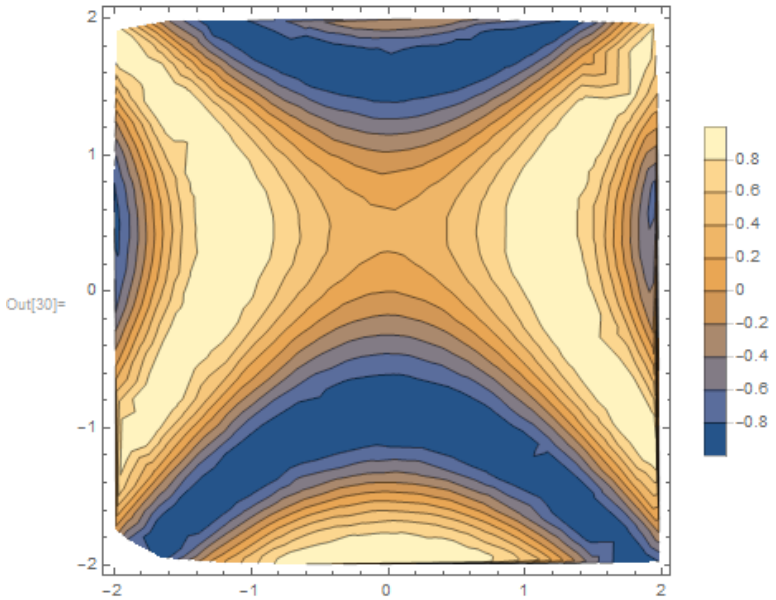

Figure (16-3) illustrate the variations in isoenergy lines arising from the interplay between the magnetic moment of hydrogen atoms and the magnetic field generated by the geometric deformation characterized by the $x^2 - y^2$ pattern.

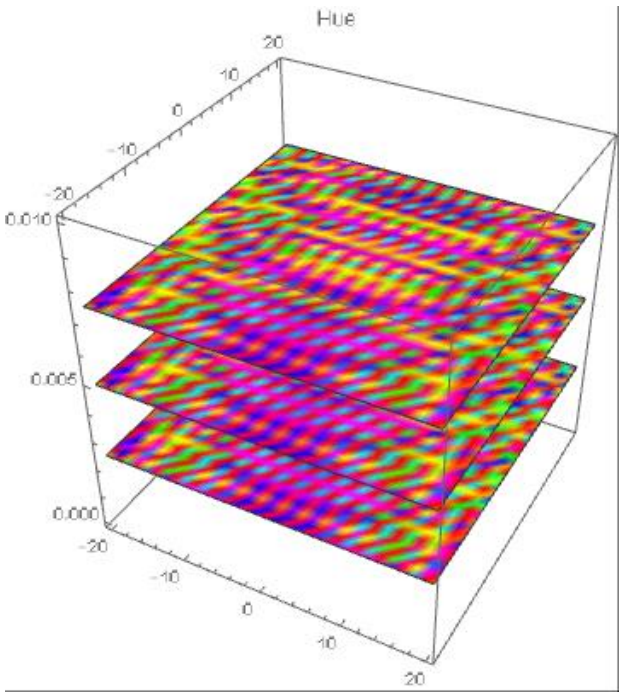

Figure (17-3) display three cross-sections demonstrating the systematic distribution of energy in specific confined regions. This distribution arises from the interplay between the magnetic moment of hydrogen atoms and the magnetic field generated due to the geometric deformation characterized by the $x^2 - y^2$ pattern.

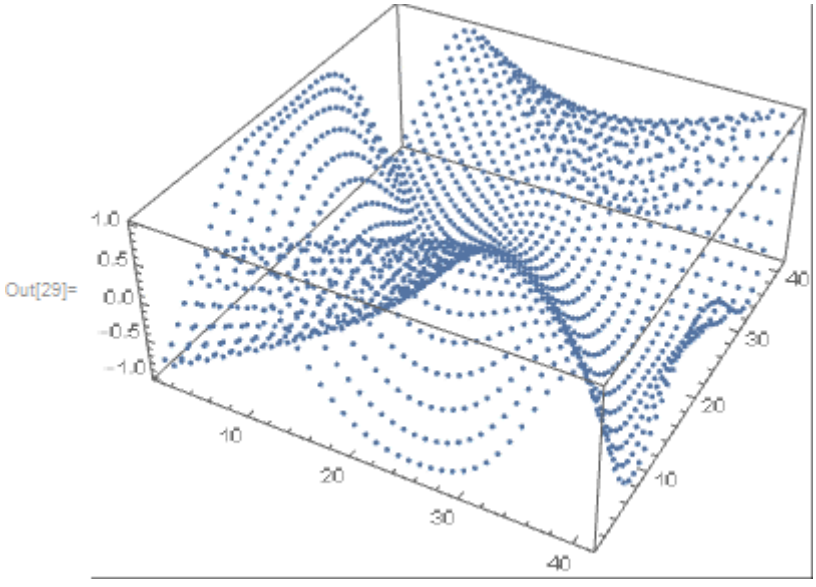

Figure (18-3) provide a simulated depiction of the distribution of hydrogen molecules across the surface of the geometric deformation.

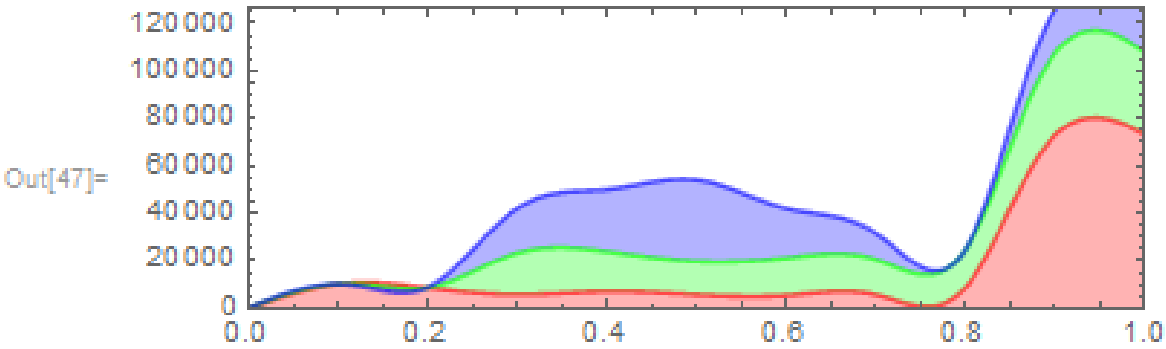

Figures (19-3) demonstrate the transformation of the preceding figure into a clearer representation when the number of hydrogen molecules is increased to 120,000 molecules.

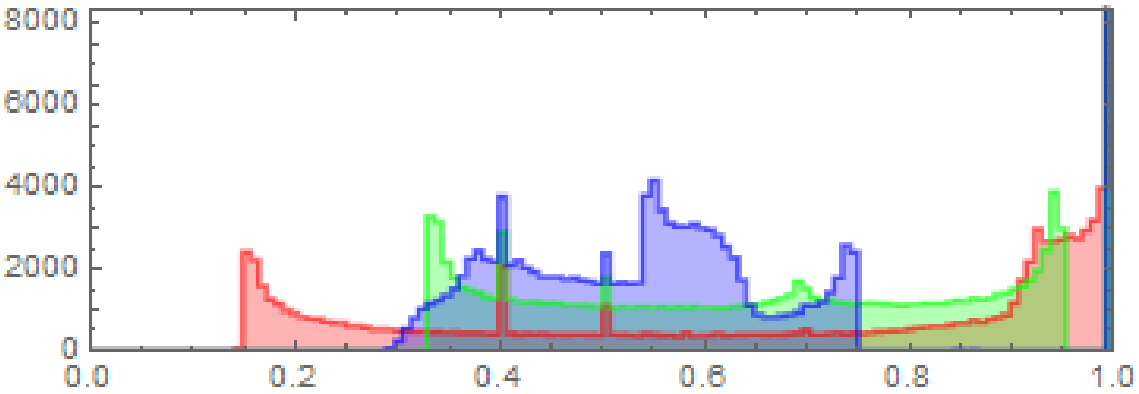

Figure (20-3) depict the distribution of 8000 hydrogen molecules on a surface consisting of a certain number of moles of graphene atoms. The blue regions represent hydrogen molecules that adhere to the surface, the green regions indicate semi-free hydrogen molecules, and the red regions indicate hydrogen molecules that exhibit strong interaction with the graphene surface.

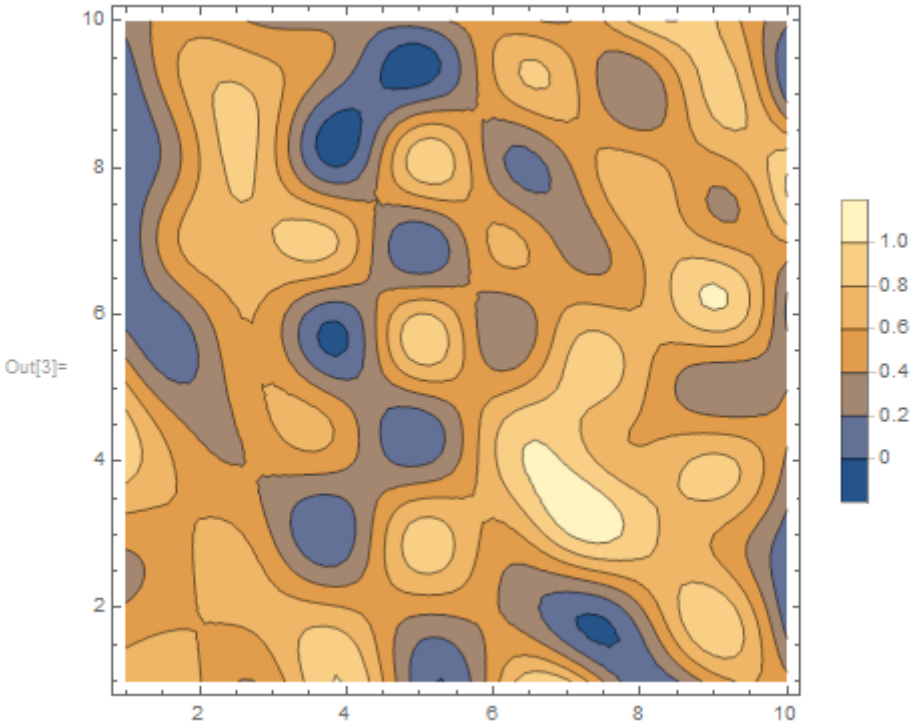

Figure (21-3) presents a simulation illustrating the distribution of reciprocal pressure across the regions generated by geometric deformations. This distribution is calculated in terms of free units.

III.3.4. Geometric distortionx^2y^2:

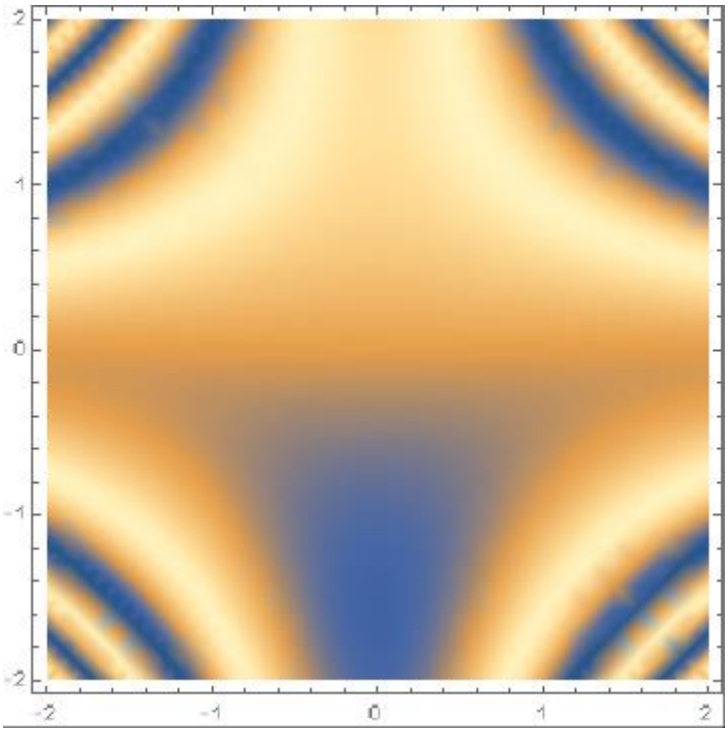

Figure (22.3): depict the alterations in energy distribution caused by the interaction between the magnetic moment of hydrogen atoms and the magnetic field generated due to the x^2y^2 geometric deformation pattern

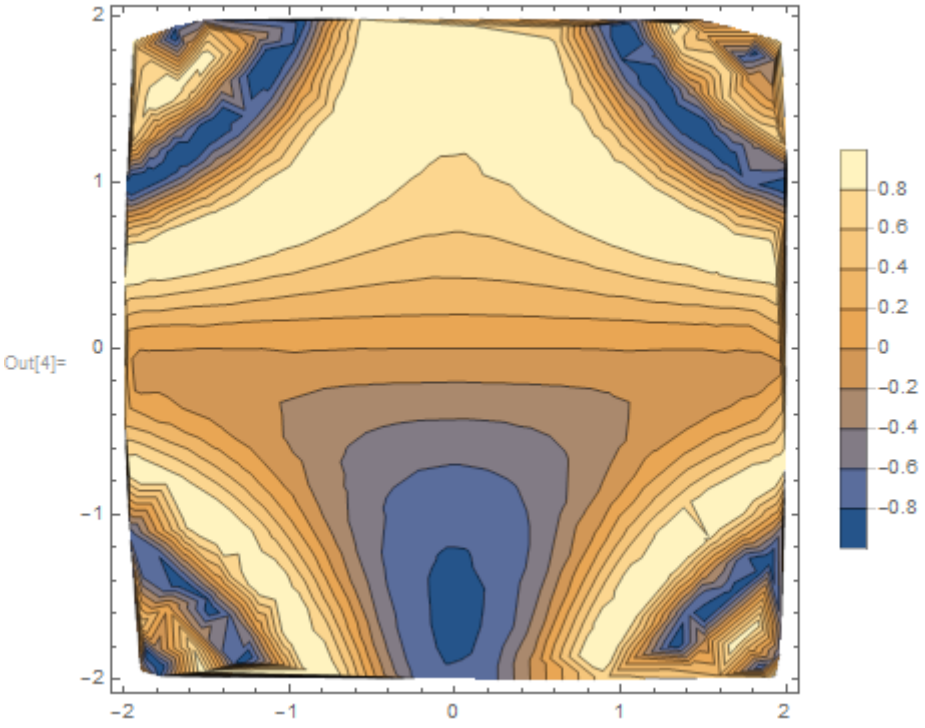

Figure (23-3) illustrates the variations in isoenergy lines arising from the interplay between the magnetic moment of hydrogen atoms and the magnetic field generated by the geometric deformation characterized by the x^2y^2pattern.

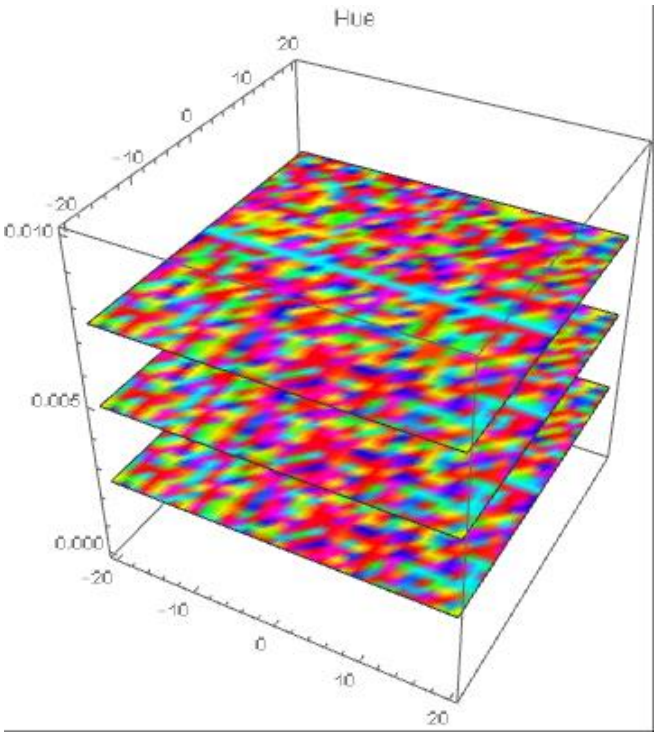

Figure (24-3) : display three cross-sections demonstrating the systematic distribution of energy in specific confined regions. This distribution arises from the interplay between the

magnetic moment of hydrogen atoms and the magnetic field generated due to the geometric deformation characterized by the x^2y^2pattern.

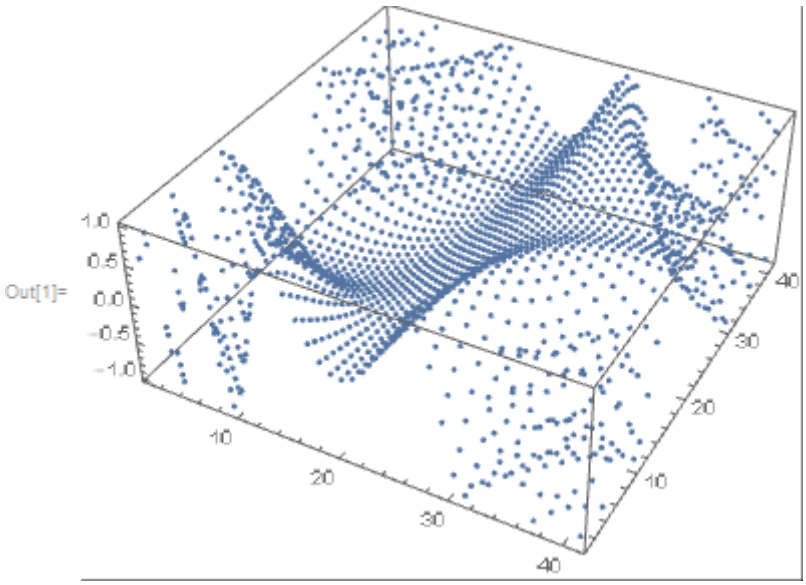

Figure (25-3): provides a simulated depiction of the distribution of hydrogen molecules across the surface of the geometric deformation.

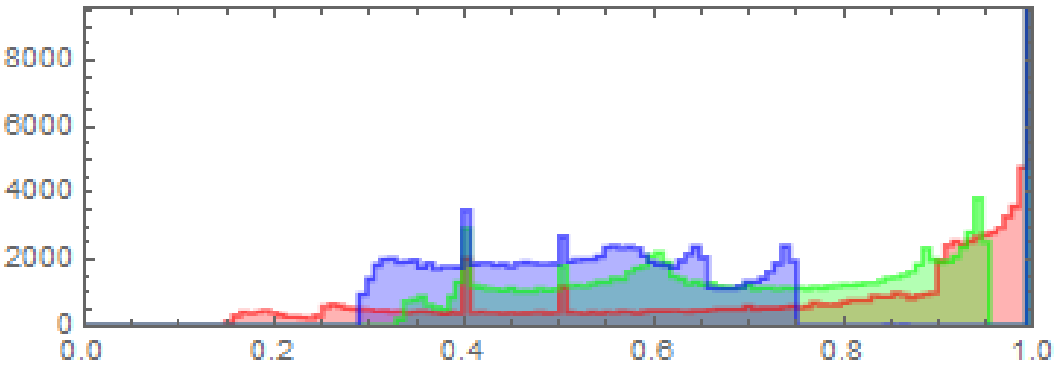

Figure (26-3) depicts the distribution of 8000 hydrogen molecules on a surface consisting of a certain number of moles of graphene atoms. The blue regions represent hydrogen molecules that adhere to the surface, the green regions indicate semi-free hydrogen molecules, and the red regions indicate hydrogen molecules that exhibit strong interaction with the graphene surface.

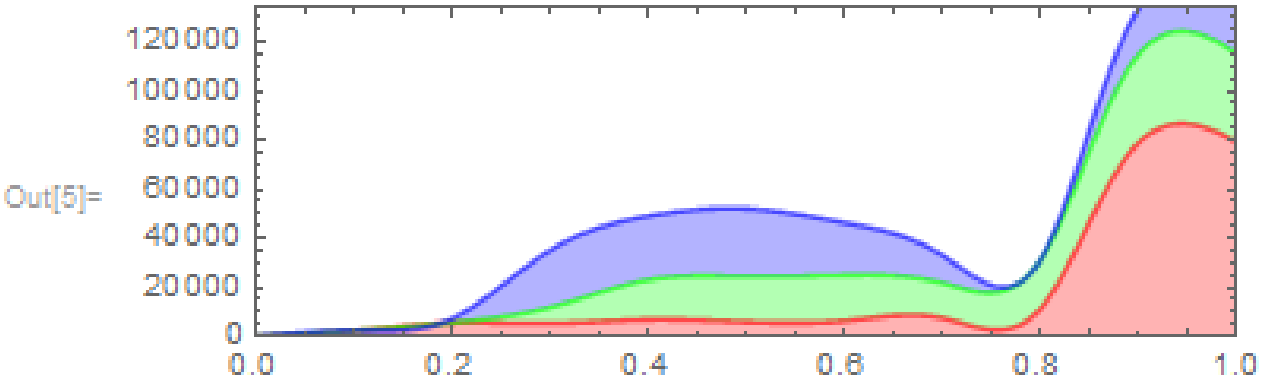

Figure (27-3): demonstrates the transformation of the preceding figure into a clearer representation when the number of hydrogen molecules is increased to 120,000 molecules.

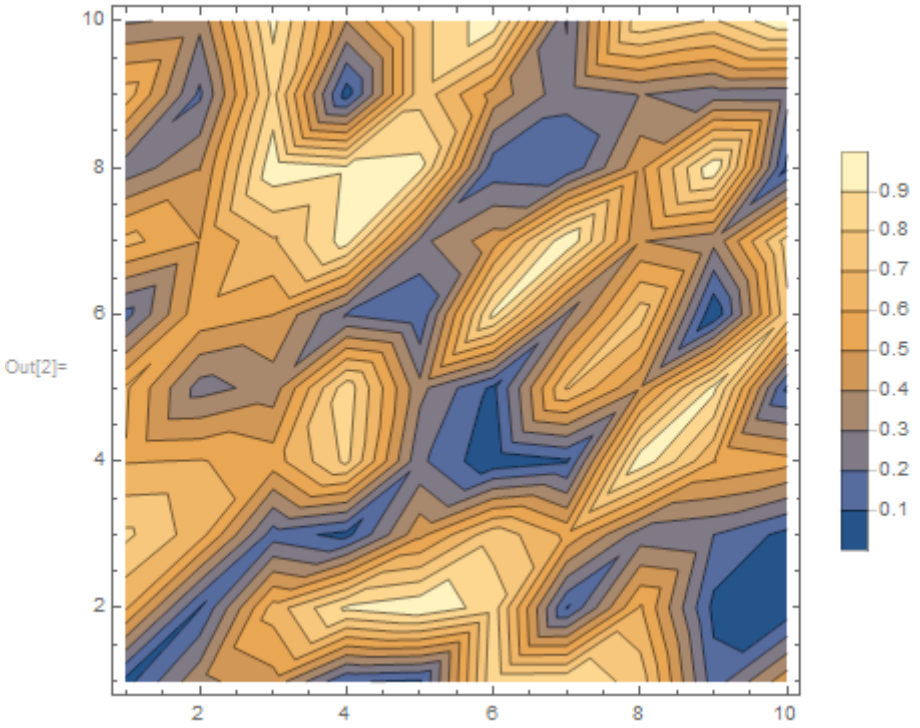

Figure (28-3) presents a simulation illustrating the distribution of reciprocal pressure across the regions generated by geometric deformations. This distribution is calculated in terms of free units.

III.3.5. Geometric distortion x + y:

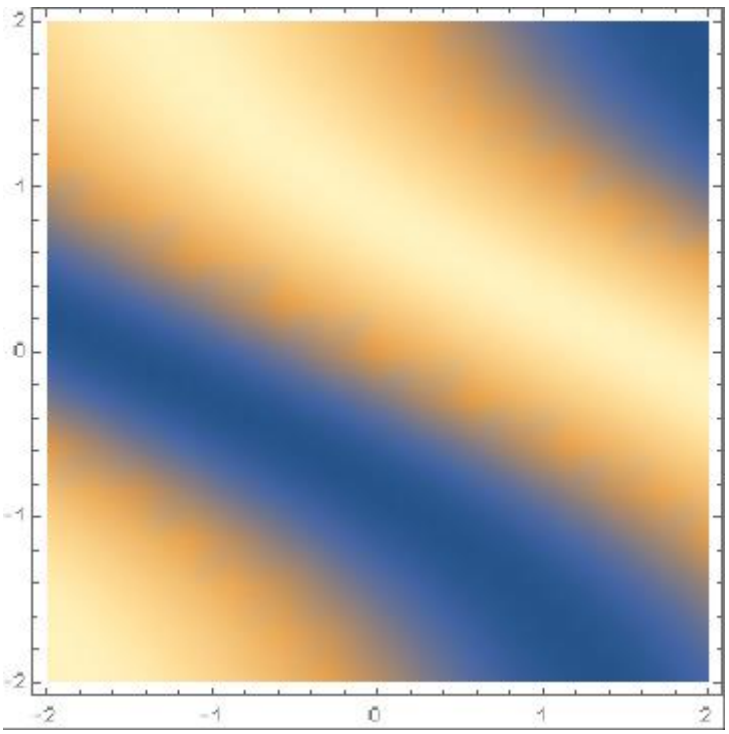

Figure (29.3): depicts the alterations in energy distribution caused by the interaction between the magnetic moment of hydrogen atoms and the magnetic field generated due to the **x + y** geometric deformation pattern

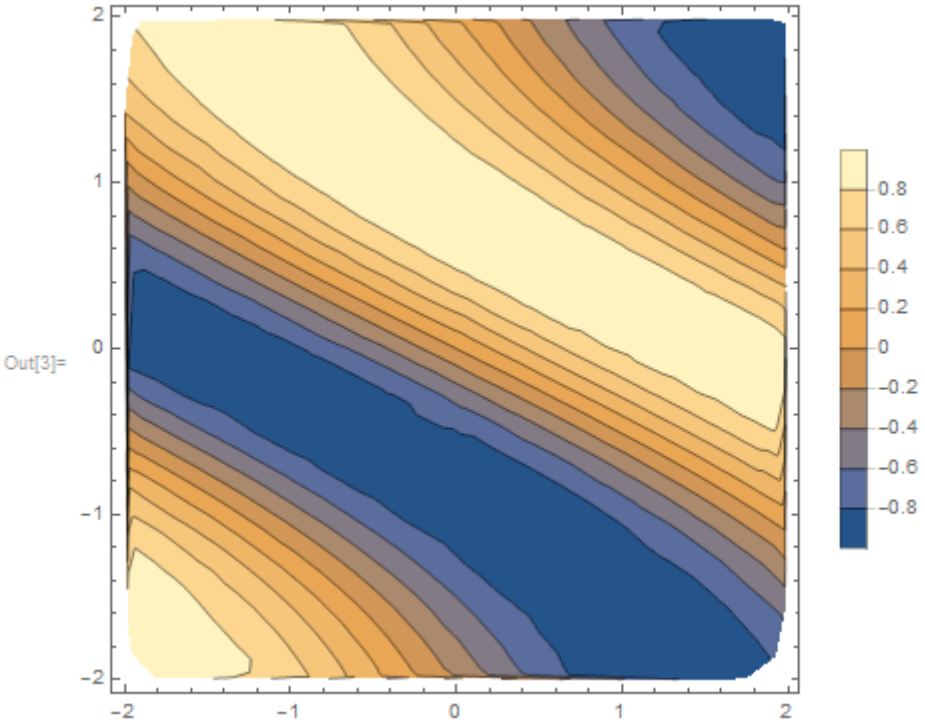

Figure (30-3) illustrates the variations in isoenergy lines arising from the interplay between the magnetic moment of hydrogen atoms and the magnetic field generated by the geometric deformation characterized by the **x** + **y**pattern.

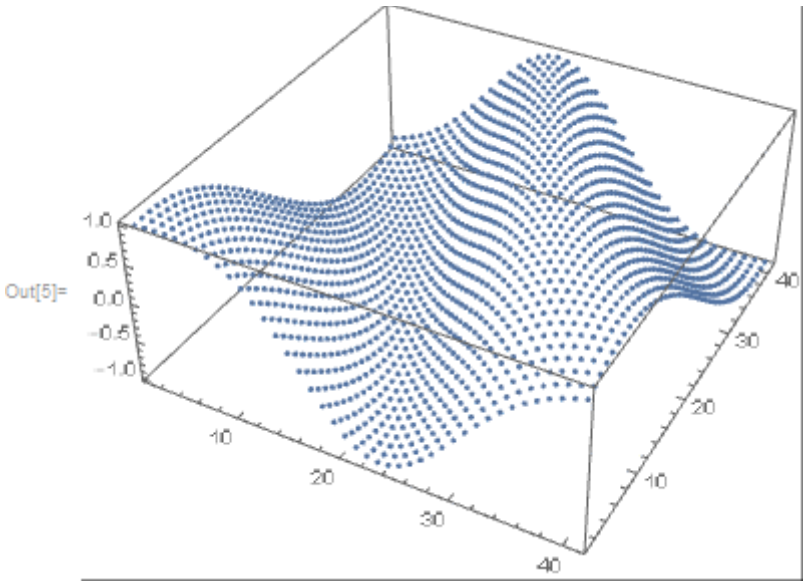

Figure (31-3) provides a simulated depiction of the distribution of hydrogen molecules across the surface of the geometric deformation.

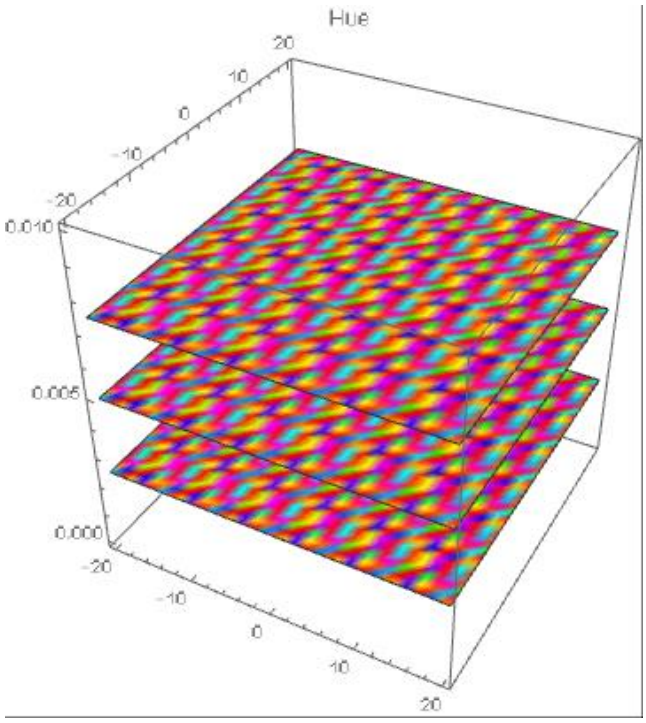

Figure (32-3) displays three cross-sections demonstrating the systematic distribution of energy in specific confined regions. This distribution arises from the interplay between the magnetic moment of hydrogen atoms and the magnetic field generated due to the geometric deformation characterized by the **x + y** pattern.

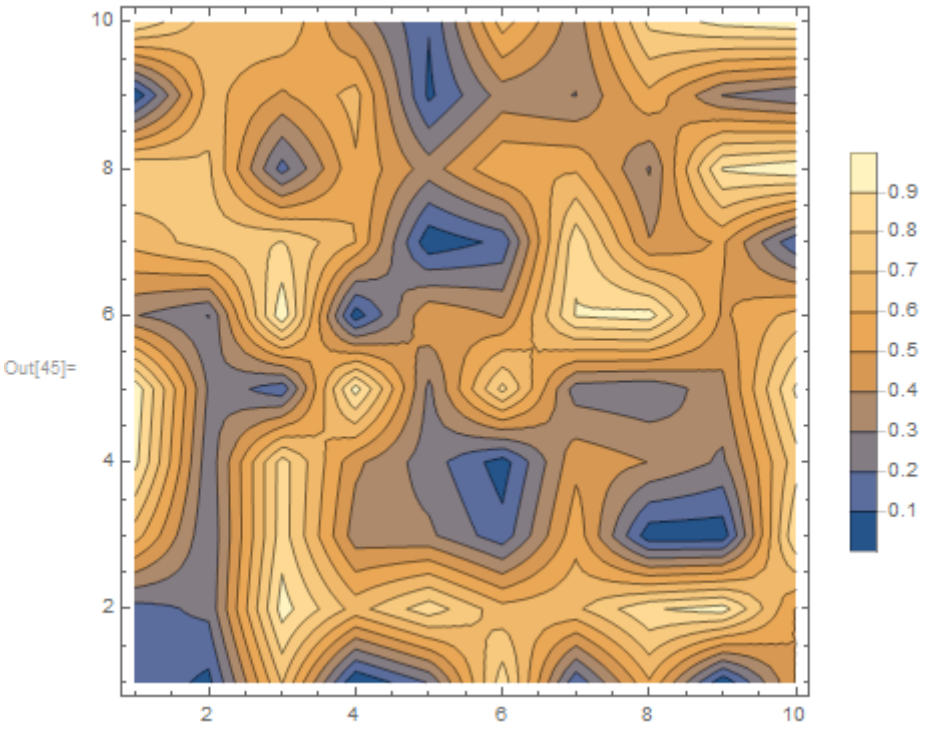

Figure (33-3) presents a simulation illustrating the distribution of reciprocal pressure across the regions generated by geometric deformations. This distribution is calculated in terms of free units.

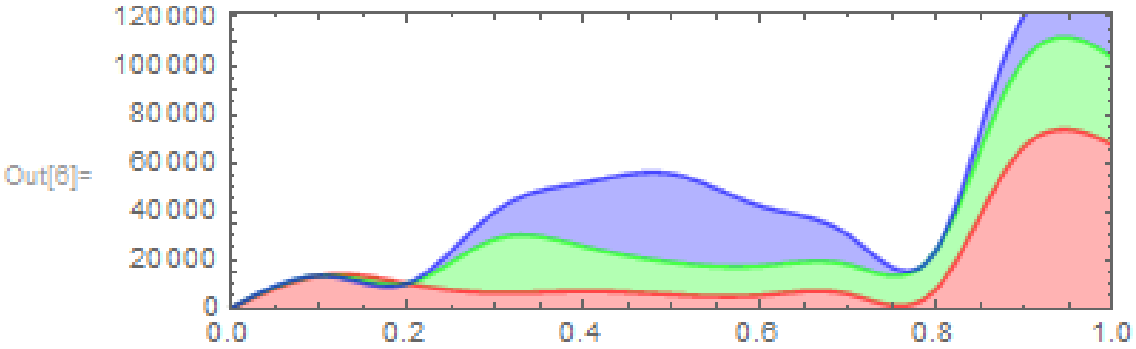

Figure (34-3) demonstrates the transformation of the preceding figure into a clearer representation when the number of hydrogen molecules is increased to 120,000 molecules.

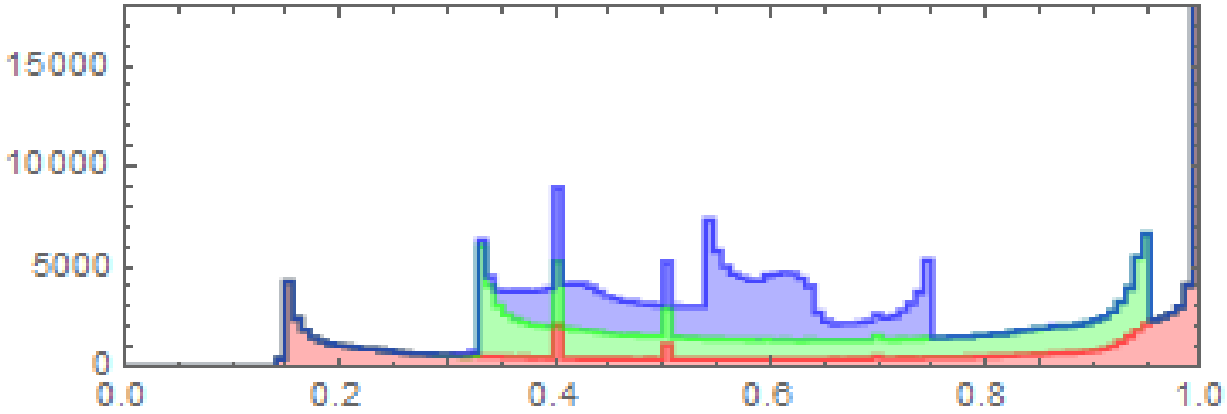

Figure (35-3) depicts the distribution of 15000 hydrogen molecules on a surface consisting of a certain number of moles of graphene atoms. The blue regions represent hydrogen molecules that adhere to the surface, the green regions indicate semi-free hydrogen molecules, and the red regions indicate hydrogen molecules that exhibit strong interaction with the graphene surface.

III.4. Discussions:

The preceding figures clearly illustrate the impact of geometric distortions on the process of hydrogen adsorption. From these figures, two significant observations can be made:

Firstly, in all of the depicted figures (3-35, 3-26, 3-20, 3-11, 3-4), the adsorption of hydrogen molecules is observed to be interrupted at approximately 0.75 molar concentration. This indicates that as the number of carbon atoms compressing the surface of graphene increases, the degrees of freedom also increase. Consequently, the influence of geometric distortions weakens the generation of magnetic fields, resulting in diminished interaction energy. Consequently, this weakened energy interaction has an impact on the capacity of hydrogen adsorption.

Secondly, based on the simulations, it is noteworthy that the geometric deformation x^2-y^2 exhibits the highest hydrogen adsorption rate at 62.5%. Comparatively, the geometric

distortions $\boldsymbol{x^2}$, $\boldsymbol{x^2y^2}$,$\mathbf{x+y}$ and $\boldsymbol{x^2+y^2}$demonstrate adsorption rates of 30%, 33.33%, 60%, and 37.5%, respectively. This can be explained by examining the energy density distribution pattern. The $\boldsymbol{x^2-y^2}$ deformation induces more pronounced geometric distortions, resulting in the generation of a stronger magnetic field and greater interaction energy, thereby enabling a higher storage capacity for hydrogen.

III.5.Conclusion:

Graphene has attracted significant scientific attention due to its exceptional properties, including strength, flexibility, and electrical conductivity. This thesis investigates the influence of magnetic fields generated by geometric distortions on graphene's surface on hydrogen storage capacity. The interplay between graphene's magnetic moment, geometric distortions, and hydrogen molecules determine whether hydrogen is stabilized or repelled from the graphene surface.

Examination of the figures presented demonstrates that hydrogen adsorption is disrupted at approximately **0.75** molar concentration. As the number of carbon atoms on the graphene surface increases, the impact of geometric distortions weakens the generation of magnetic fields, resulting in reduced energy interaction and affecting the capacity for hydrogen adsorption.

Simulation results highlight the $\boldsymbol{x^2-y^2}$ deformation as having the highest hydrogen adsorption rate at **62.5%.** Other deformations, such as$\boldsymbol{x^2}$, $\boldsymbol{x^2y^2}$,$\mathbf{x+y}$ and $\boldsymbol{x^2+y^2}$, exhibit adsorption rates of 30%, 33.33%, 60%, and 37.5% respectively. These differences can be attributed to the distribution of energy density. The $\boldsymbol{x^2-y^2}$deformation induces more significant geometric distortions, leading to a stronger magnetic field and increased interaction energy, thus enhancing hydrogen storage capacity.

References

[1]Peierls, R. (1934) 'Zur Theorie des Diamagnetismus von Leitungselektronen', Helv. Phys. Acta, 7, pp. 81-83.

[2]Landau, L. D., and Lifshitz, E. M. (1980) Statistical Physics Part I. Oxford: Pergamon.

[3]Venables, J. A., Spiller, G. D. T., and Hanbucken, M. (1984) 'Nucleation and growth of thin films', Rep. Prog. Phys., 47, pp. 399-459.

[4]Novoselov, K. S., Geim, A. K., Morozov, S. V., Jiang, D., Zhang, Y., Dubonos, S. V., Grigorieva, I. V., and Firsov, A. A. (2004) 'Electric field effect in atomically thin carbon films', Science, 306, pp. 666-669.

[5]Novoselov, K. S., Jiang, D., Schedin, F., Booth, T. J., Khotkevich, V. V., Morozov, S. V., and Geim, A. K. (2005) 'Two-dimensional atomic crystals', Proc. Natl. Acad. Sci. U.S.A., 102, pp. 10451-10453.

[6]Geim, A. K., and Novoselov, K. S. (2007) 'The rise of graphene', Nat. Mater., 6, pp. 183-191.

[7]Fasolino, A., Los, J. H., and Katsnelson, M. I. (2007) 'Intrinsic ripples in graphene', Nat. Mater., 6, pp. 858-861.

[8]Meyer, J. C., Geim, A. K., Katsnelson, M. I., Novoselov, K. S., Booth, T. J., and Roth, S. (2007) 'The structure of suspended graphene sheets', Nature, 446, pp. 60-63.

[109]9.Seibert, K., Cho, G. C., Kütt, W., Kurz, H., Reitze, D. H., Dadap, J. I., Ahn, H., Downer, M. C., and Malvezzi, A. M. (1990) 'Ultrafast electron transport in metallo-organic superlattices', Phys. Rev. B, 42, pp. 2842-2851.

[10]Novoselov, K. S., Geim, A. K., Morozov, S. V., Jiang, D., Zhang, Y., Dubonos, S. V., Grigorieva, I. V., and Firsov, A. A. (2004) 'Electric field effect in atomically thin carbon films', Science, 306, pp. 666-669.

[11] b) Technical University of Manchester (2013) 'Graphene at the University of Manchester'. Available at: http://www.graphene.manchester.ac.uk/story/ (Accessed: 2013).

[12] Chen, J., Duan, M., and Chen, G. (2012) 'Graphene-based materials for energy conversion', J. Mater. Chem., 22, pp. 19625-19628.

[13] Hernandez, Y., Nicolosi, V., Lotya, M., Blighe, F. M., Sun, Z., De, S., McGovern, I. T., Holland, B., Byrne, M., Gun'ko, Y. K., Boland, J. J., Niraj, P., Duesberg, G., Krishnamurthy, S., Goodhue, R., Hutchison, J., Scardaci, V., Ferrari, A. C., and Coleman, J. N. (2008) 'High-yield production of graphene by liquid-phase exfoliation of graphite', Nat. Nano, 3, pp. 563-568.

[14] Alzari, V., Nuvoli, D., Scognamillo, S., Piccinini, M., Gioffredi, E., Malucelli, G., Marceddu, S., Sechi, M., Sanna, V., and Mariani, A. (2011) 'Water-dispersible functionalized graphene nanosheets: interaction with human plasma proteins', J. Mater. Chem., 21, pp. 8727-8733.

[15] Nuvoli, D., Valentini, L., Alzari, V., Scognamillo, S., Bon, S. B., Piccinini, M., Illescas, J., and Mariani, A. (2011) 'The new frontiers of graphene oxide', J. Mater. Chem., 21, pp. 3428-3431.

[16] Berger, C., Song, Z., Li, T., Li, X., Ogbazghi, A. Y., Feng, R., Dai, Z., Marchenkov, A. N., Conrad, E. H., First, P. N., and de Heer, W. A. (2004) 'Ultrathin epitaxial graphite: 2D electron gas properties and a route toward graphene-based nanoelectronics', J. Phys. Chem. B, 108, pp. 19912-19916.

[17] Berger, C., Song, Z., Li, X., Wu, X., Brown, N., Naud, C., Mayou, D., Li, T., Hass, J., Marchenkov, A. N., Conrad, E. H., First, P. N., and de Heer, W. A. (2006) 'Electronic confinement and coherence in patterned epitaxial graphene', Science, 312, pp. 1191-1196.

[18] a) Hass, J., de Heer, W. A., and Conrad, E. H. (2008) 'The growth and morphology of epitaxial multilayer graphene', J. Phys. Condens. Matter, 20, p. 323202.

[18] b) Kedzierski, J., Pei-Lan, H., Healey, P., Wyatt, P. W., Keast, C. L., Sprinkle, M., Berger, C., and De Heer, W. A. (2008) 'Epitaxial graphene transistors: electrons in a well on SiC', IEEE Trans. Electron Dev., 55, pp. 2078-2085.

[19] a) Grant, J. T., and Haas, T. W. (1970) 'Surface states on epitaxial graphite', Surf. Sci., 21, pp. 76-85.

[19] b) Rosei, R., De Crescenzi, M., Sette, F., Quaresima, C., Savoia, A., and Perfetti, P. (1983) 'The structural and electronic properties of graphite', Phys. Rev. B, 28, pp. 1161-1164.

[19] c) Land, T. A., Michely, T., Behm, R. J., Hemminger, J. C., and Comsa, G. (1992) 'STM investigation of single layer graphite structures produced on Pt(111) by hydrocarbon decomposition', Surf. Sci., 264, pp. 261-270.

[19] d) Blakely, J. M., Kim, J. S., and Potter, H. C. (1970) 'Graphite monolayers on metals: growth and electronic properties', J. Appl. Phys., 41, pp. 2693-2697.

[19] e) McConville, C. F., Woodruff, D. P., Kevan, S. D., Weinert, M., and Davenport, J. W. (1986) 'Valence-band photoemission studies of the interaction of oxygen with the graphite (0001) surface', Phys. Rev. B, 34, pp. 2199-2206.

[20] Mattevi, C., Kim, H., and Chhowalla, M. (2011) 'A review of chemical vapour deposition of graphene on copper', J. Mater. Chem., 21, pp. 3324-3334.

[21] Li, X., Cai, W., Colombo, L., and Ruoff, R. S. (2009) 'Evolution of graphene growth on Ni and Cu by carbon isotope labeling', Nano Lett., 9(12), pp. 4268-4272.

[22] Compton, O. C., and Nguyen, S. T. (2010) 'Graphene oxide, highly reduced graphene oxide, and graphene: versatile building blocks for carbon-based materials', Small, 6(6), pp. 711-723.

[23] Stankovich, S., Dikin, D. A., Piner, R. D., Kohlhaas, K. A., Kleinhammes, A., Jia, Y., Wu, Y., Nguyen, S. T., and Ruoff, R. S. (2007) 'Synthesis of graphene-based nanosheets via chemical reduction of exfoliated graphite oxide', Carbon, 45(7), pp. 1558-1565.

[24] Allen, M. J., Tung, V. C., and Kaner, R. B. (2009) 'Honeycomb carbon: a review of graphene', Chem. Rev., 110(1), pp. 132-145.

[25] Xu, Y., Liu, Z., Zhang, X., Wang, Y., Tian, J., Huang, Y., Ma, Y., Zhang, X., and Chen, Y. (2009) 'Flexible graphene films via the filtration of water-soluble noncovalent functionalized graphene sheets', Adv. Mater., 21(12), pp. 1275-1279.

[26] Kim, K. S., Zhao, Y., Jang, H., Lee, S. Y., Kim, J. M., Kim, K. S., Ahn, J.-H., Kim, P., Choi, J.-Y., and Hong, B. H. (2009) 'Large-scale pattern growth of graphene films for stretchable transparent electrodes', Nature, 457(7230), pp. 706-710.

[27] Coraux, J., N'Diaye, A. T., Busse, C., and Michely, T. (2008) 'Structural coherency of graphene on Ir(111)', Nano Lett., 8(2), pp. 565-570.

[28] Sutter, P. W., Flege, J.-I., and Sutter, E. A. (2008) 'Epitaxial graphene on ruthenium', Nat. Mater., 7(5), pp. 406-411.

[29] Li, X., Cai, W., An, J., Kim, S., Nah, J., Yang, D., Piner, R., Velamakanni, A., Jung, I., Tutuc, E., Banerjee, S. K., Colombo, L., and Ruoff, R. S. (2009) 'Large-area synthesis of high-quality and uniform graphene films on copper foils', Science, 324(5932), pp. 1312-1314.

[30] Novoselov, K. S., Geim, A. K., Morozov, S. V., Jiang, D., Katsnelson, M. I., Grigorieva, I. V., Dubonos, S. V., and Firsov, A. A. (2005) 'Two-dimensional gas of massless Dirac fermions in graphene', Nature, 438(7065), pp. 197-200.

[31] Gui, G., Li, J., and Zhong, J. X. (2008) 'Band structure engineering of graphene by strain: First-principles calculations', Phys. Rev. B, 78(7), 075435. doi: 10.1103/PhysRevB.78.075435.

[32] Pereira, V. M., Castro Neto, A. H., and Peres, N. M. R. (2009) 'Tight-binding approach to uniaxial strain in graphene', Phys. Rev. B, 80(4), 045401. doi: 10.1103/PhysRevB.80.045401.

[33] Li, Y., Jiang, X. W., Liu, Z. F., and Liu, Z. R. (2010) 'Strain effects in graphene and graphene nanoribbons: the underlying mechanism', Nano Res., 3(8), pp. 545-556. doi: 10.1007/s12274-010-0015-7.

[34] Yang, L., and Han, J. (2000) 'Electronic structure of deformed carbon nanotubes', Phys. Rev. Lett., 85(1), pp. 154-157. doi: 10.1103/PhysRevLett.85.154.

[35] Harrison, W. A. (1989) 'Electronic structure and the properties of solids: The physics of the chemical bond', Dover Publications, New York.

[36] Hohenberg, P., and Kohn, W. (1964) 'Inhomogeneous electron gas', Phys. Rev. B, 136(3B), pp. B864-B871. doi: 10.1103/PhysRev.136.B864.

[37] Parr, R. G., and Weitao, Y. (1994) 'Density-functional theory of atoms and molecules', Oxford University Press, USA.

[38] Novoselov, K. S., Geim, A. K., Morozov, S. V., Jiang, D., Zhang, Y., Dubonos, S. V., Grigorieva, I. V., and Firsov, A. A. (2004) 'Electric field effect in atomically thin carbon films', Science, 306, pp. 666-669.

[39] Novoselov, K. S., Geim, A. K., Morozov, S. V., Jiang, D., Katsnelson, M. I., Grigorieva, I. V., Dubonos, S. V., and Firsov, A. A. (2005) 'Two-dimensional gas of massless Dirac fermions in graphene', Nature, 438, pp. 197-200.

[40] Streda, P. (n.d.) 'Electron Transport in Quantum Systems'. Available via http://unix12.fzu.cz/~vybornyk/physics/qtr/mat/skriptum_nbcm096.pdf.

[41] Nathan, A., Ahnood, A., Cole, M. T., Sungsik, L., Suzuki, Y., Hiralal, P., ... Milne, W. I. (2012) 'Large-area graphene electronics: materials, devices, and system integration', Proc. IEEE, 100, pp. 1486-1517.

[42] Fiori, G., Bonaccorso, F., Iannaccone, G., Palacios, T., Neumaier, D., Seabaugh, A., ... Colombo, L. (2014) 'Electronics based on two-dimensional materials', Nat. Nanotechnol., 9, pp. 768-779.

[43] Sundmaeker, H., Guillemin, P., Friess, P., & Woelffle, S. (2010) 'Vision and challenges for realising the Internet of Things', European Commission Information Society and Media, Tech. Rep., March.

[44] International Data Corporation (IDC) USA (2012) 'Worldwide smart connected device shipments'. Available at: http://www.idc.com/getdoc.jsp?containerId=prUS23398412.

[45] Yang, L., Sheldon, B. W., Webster, T. J., & Biomed, J. (2008) 'Nanostructured diamond coatings for orthopaedic applications', Mater. Res. A, 91, pp. 548-556.

[46] Grill, A. (2003) 'Diamond tribology: nanoscale wear and friction studies', Diamond Relat. Mater., 12, pp. 166-170.

[47] Lee, H., Lee, N., Seo, Y., Eom, J., & Lee, S. W. (2009) 'Surface modification for the reduced graphene oxide nanosheet for electronic device applications', Nanotechnology, 20, 325701.

[48] Hauert, R. (2004) 'A review of modified DLC coatings for biological applications', Tribol. Int., 37, pp. 991-1003.

[49] Gonçalves, G., Marques, P. A. A. P., Barros-Timmons, A., Bdkin, I., Singh, M. K., Emami, N., & Grácio, J. (2010) 'Tribological behavior of tetrahedral amorphous carbon (ta-C) coatings under different environmental conditions', J. Mater. Chem., 20, pp. 9927-9934.

[50] Rondin, L., Tetienne, J.-P., Spinicelli, P., Dal Savio, C., Karrai, K., Dantelle, G., ... Jacques, V. (2012) 'Surface-induced charge state conversion of nitrogen-vacancy defects in nanodiamonds', Appl. Phys. Lett., 100, 153118.

[51] Chemla, Y. R., Grossman, H. L., Poon, Y., McDermott, R., Stevens, R., Alper, M. D., & Clarke, J. (2000) 'Ultrafast coherent control and spectroscopy of semiconductor interband resonances: the pump-probe case', Proc. Natl. Acad. Sci. U. S. A., 97, pp. 14268-14272.

[52] Busham, B. (1990) Tribology and mechanics of magnetic storage devices. Springer.

[53] Pisana, S., Braganca, P. M., Marinero, E. E., & Gurney, B. A. (2009) 'High-sensitivity chemical sensors based on epitaxial graphene on SiC', Nano Lett., 10, pp. 341-346.

[54] Ramsden, E. (2006) Hall-Effect Sensors. Elsevier.

[55] Source: IHS iSuppli Market Research.

[56] Miremadi, B. K., Singh, R. C., Morrison, S. R., & Colbow, K. (1996) 'Carbon overcoat of magnetic thin films', Appl. Phys. A. Mater. Sci. Process., 63, pp. 271-275.

[57] Zeng, Z. Y., Yin, Z. Y., Huang, X., Li, H., He, Q. Y., Lu, G., ... Zhang, H. (2011) 'Single-layer semiconducting nanosheets: high-yield preparation and device fabrication', Angew. Chem., Int. Ed., 50, pp. 11093-11097.

[58] Li, H., Yin, Z., He, Q., Li, H., Huang, X., Lu, G., ... Zhang, H. (2012) 'Fabrication of single- and multilayer MoS2 film-based field-effect transistors for sensing NO at room temperature', Small, 8, pp. 63-67.

[59] Late, D. J., Huang, Y.-K., Liu, B., Acharya, J., Shirodkar, S. N., Luo, J., ... Rao, C. N. R. (2013) 'Sensitivity of graphene to divalent cations present in biological fluids', ACS Nano, 7, pp. 4879-4891.

[60] He, Q., Zeng, Z., Yin, Z., Li, H., Wu, S., Huang, X., & Zhang, H. (2012) 'Fabrication of flexible MoS2 thin-film transistor arrays for practical gas-sensing applications', Small, 8, pp. 2994-2999.

[61] Tombler, T. W., Zhou, C. W., Alexseyev, L., Kong, J., Dai, H. J., Lei, L., ... Wu, S. Y. (2000) 'Reversible electromechanical characteristics of carbon nanotubes under local-probe manipulation', Nature, 405, pp. 769-772.

[62] Wang, Y., Yang, R., Shi, Z. W., Zhang, L. C., Shi, D. X., Wang, E., & Zhang, G. Y. (2011) 'Raman studies of monolayer graphene: the substrate effect', ACS Nano, 5, pp. 3645-3650.

[63] Lee, Y., Bae, S., Jang, H., Jang, S., Zhu, S. E., Sim, S. H., ... Ahn, J. H. (2010) 'Wafer-scale synthesis and transfer of graphene films', Nano Lett., 10, pp. 490.

[64] Fu, X. W., Liao, Z. M., Zhou, J. X., Zhou, Y. B., Wu, H. C., Zhang, R., ... Yu, D. P. (2011) 'Direct growth of single-walled carbon nanotube film on quartz substrates', Appl. Phys. Lett., 99, pp. 213107.

[65] Bunch, J. S., Verbridge, S. S., Alden, J. S., van der Zande, A. M., Parpia, J. M., Craighead, H. G., ... McEuen, P. L. (2008) 'Impermeable atomic membranes from graphene sheets', Nano Lett., 8, pp. 2458-2462.

[66] Leenaerts, O., Partoens, B., & Peeters, F. M. (2008) 'Graphene: a perfect nanoballoon', Appl Phys Lett., 93, pp. 193107.

[67] Hrusak, J., Bohme, D. K., Weiske, T., & Schwarz, H. (1992) 'Ab initio MO calculation on the energy barrier for the penetration of a benzene ring by a helium atom', Chem Phys Lett., 193, pp. 97-100.

[68] Murry, R. L., & Scuseria, G. E. (1994) 'Theoretical evidence for a C60 "window" mechanism', Science, 263, pp. 791-793.

[69] Geim, A. K., & Novoselov, K. S. (2007) 'The rise of graphene', Nat Mater., 6, pp. 183-191.

[70] Georgiou, T., Britnell, L., Blake, P., Gorbachev, R. V., Gholinia, A., Geim, A. K., ... Haigh, S. J. (2011) 'Graphene bubbles with controllable curvature', Appl Phys Lett., 99, pp. 093103.

[71] Reserbat-Plantey, A., et al. (2014) 'Strain superlattices and macroscale suspension of graphene induced by corrugated substrates', Nano Lett., 14, pp. 5044-5051.

[72] Choi, J., et al. (2015) 'Three-dimensional integration of graphene via swelling, shrinking, and adaptation', Nano Lett., 15, pp. 4525-4531.

[73] Goldsche, M., et al. (2018) 'Tailoring mechanically tunable strain fields in graphene', Nano Lett., 18, pp. 1707-1713.

[74] Mi, H., et al. (2015) 'Creating periodic local strain in monolayer graphene with nanopillars patterned by self-assembled block copolymer', Appl. Phys. Lett., 107, pp. 143107.

[75] Yoon, D., Son, Y. W., & Cheong, H. (2011) 'Strain-dependent splitting of the double resonance Raman scattering band in graphene', Phys. Rev. Lett., 106, pp. 155502.

[76] Li, H., et al. (2015) 'Optoelectronic crystal of artificial atoms in strain-textured molybdenum disulphide', Nat. Commun., 6, pp. 7381.

[77] Pereira, V. M., & Castro Neto, A. H. (2009) 'Strain engineering of graphene's electronic structure', Phys. Rev. Lett., 103, pp. 046801.

[78] Guinea, F., Katsnelson, M. I., & Geim, A. K. (2010) 'Energy gaps and a zero-field quantum Hall effect in graphene by strain engineering', Nat. Phys., 6, pp. 30-33.

[79] Zhu, S., Stroscio, J. A., & Li, T. (2015) 'Programmable extreme pseudomagnetic fields in graphene by a uniaxial stretch', Phys. Rev. Lett., 115, pp. 245501.

[80] Neek-Amal, M., Covaci, L., & Peeters, F. M. (2012) 'Nanoengineered nonuniform strain in graphene using nanopillars', Phys. Rev. B, 86, pp. 041405.

[81] Levy, N., et al. (2010) 'Strain-induced pseudo-magnetic fields greater than 300 tesla in graphene nanobubbles', Science, 329, pp. 544-547.

[82] Hsu, C. C., Teague, M. L., Wang, J. Q., & Yeh, N. C. (2020) 'Nanoscale strain engineering of giant pseudo-magnetic fields, valley polarization, and topological channels in graphene', Sci. Adv., 6, eaat9488.

[83] Guinea, F., Geim, A. K., Katsnelson, M. I., & Novoselov, K. S. (2010) 'Generating quantizing pseudomagnetic fields by bending graphene ribbons', Phys. Rev. B, 81, 035408.

[84] Li, S. Y., Su, Y., Ren, Y. N., & He, L. (2015) 'Valley polarization and inversion in strained graphene via pseudo-Landau levels, valley splitting of real Landau', Phys. Rev. B, 91, 205437.

[85] Qi, Z., et al. (2014) 'Pseudomagnetic fields in graphene nanobubbles of constrained geometry: a molecular dynamics study', Phys. Rev. B, 90, 125419.

[86] Ryhänen, T., Uusitalo, M. A., Ikkala, O., & Kärkkäinen, A. (Eds.). (2010) 'Nanotechnologies for Future Mobile Devices', Cambridge University Press.

[87] Yang, J., Sudik, A., Wolverton, C., & Siegel, D. J. (2010) 'Chem. Soc. Rev.', 39, pp. 656.

[88] Sinigaglia, T., Lewiski, F., Santos Martins, M. E., & Mairesse Siluk, J. C. (2017) 'Int. J. Hydrogen Energy', 42, pp. 24597.

[89] Mazloomi, K., & Gomes, C. (2012) 'Renew. Sustain. Energy Rev.', 16, pp. 3024.

[90] Patel, S., Patel, P., Chodvadiya, D., Som, N. N., & Jha, P. K. (2022) 'J. Mol. Liq.', 352, 118702.

[91] Upadhyay, D., Roondhe, B., Pratap, A., & Jha, P. K. (2019) 'Appl. Surf. Sci.', 476, pp. 198.

[92] Xia, Y., Yang, Z., & Zhu, Y. (2013) 'J. Mater. Chem. A', 1, pp. 9365.

[93] DOE technical system targets for onboard hydrogen storage for light-duty fuel cell vehicles. Available: link (accessed on 20 April 2022).

[94] Liu, S. S., Sun, L. X., Zhang, Y., Xu, F., Zhang, J., Chu, H. L., et al. (2009) 'Effect of ball milling time on the hydrogen storage properties of TiF3-doped LiAlH4', International Journal of Hydrogen Energy, 34, pp. 8079-85.

[95] Marrero-Alfonso, E. Y., Gray, J. R., Davis, T. A., & Matthews, M. A. (2007) 'Hydrolysis of sodium borohydride with steam', International Journal of Hydrogen Energy, 32, pp. 4717-22.

[96] Sakintuna, B., Lamari-Darkrim, F., & Hirscher, M. (2007) 'Metal hydride materials for solid hydrogen storage: A review', International Journal of Hydrogen Energy, 32, pp. 1121-40.

[97] Zhang, H. J., Loo, Y. S., Geerlings, H., Lin, J. Y., & Chin, W. S. (2010) 'Hydrogen production from solid reactions between MAlH4 and NH4Cl', International Journal of Hydrogen Energy, 35, pp. 176-80.

[98] Norskov, J. K., Houmoller, A., Johansson, P. K., & Lundqvist, B. I. (1981) 'Adsorption and dissociation of H2 on Mg Surfaces', Physical Review Letters, 46, pp. 257-60.

[99] Yu, X. B., Wu, Z., Huang, T. Z., Cheng, J. Z., Xia, B. J., & Xu, N. X. (2004) 'Effect of surface oxide layer on activation performance of hydrogen storage alloy TiMn1.25Cr0.25', International Journal of Hydrogen Energy, 29, pp. 81-6.

[100] Haul, R. S. J., & Gregg, K. S. W. (1982) 'Sing: Adsorption, surface area and porosity', Ber. Bunsenges. Phys. Chem., 86, pp. 957.

[101] Rouquerol, J., Rouquerol, F., Llewellyn, P., Maurin, G., & Sing, K.S.W. (2013) 'Adsorption by Powders and Porous Solids: Principles, Methodology and Applications', Academic Press: Cambridge, MA, USA, ISBN 978-0-08-097036-3.

[102] Lowell, S., Shields, J.E., Thomas, M.A., & Thommes, M. (2004) 'Characterization of Porous Solids and Powders: Surface Area, Pore Size and Density', Particle Technology Series, Springer: Dordrecht, The Netherlands, ISBN 978-1-4020-2302-6.

[103] Thommes, M., Kaneko, K., Neimark, A.V., Olivier, J.P., Rodriguez-Reinoso, F., Rouquerol, J., & Sing, K.S.W. (2015) 'Physisorption of gases, with special reference to the evaluation of surface area and pore size distribution (IUPAC Technical Report)', Pure Appl. Chem., 87, pp. 1051-1069.

[104] von Helmolt, R., & Eberle, U. (2007) 'Fuel cell vehicles: Status 2007', Journal of Power Sources, 165, pp. 833-43.

[105] Eberle, U., Felderhoff, M., & Schuth, F. (2009) 'Chemical and Physical Solutions for Hydrogen Storage', Angewandte Chemie-International Edition, 48, pp. 6608-30.

[106] Eberle, U., Arnold, G., & von Helmolt, R. (2006) 'Hydrogen storage in metal-hydrogen systems and their derivatives', Journal of Power Sources, 154, pp. 456-60.

[107] Zhang, J.S., Fisher, T.S., Ramachandran, P.V., Gore, J.P., & Mudawar, I. (2005) 'A review of heat transfer issues in hydrogen storage technologies', Journal of Heat Transfer-Transactions of the Asme, 127, pp. 1391-9.

[108] Aceves, S.M., Espinosa-Loza, F., Ledesma-Orozco, E., Ross, T.O., Weisberg, A.H., Brunner, T.C., et al. (2010) 'High-density automotive hydrogen storage with cryogenic capable pressure vessels', International Journal of Hydrogen Energy, 35, pp. 1219-26.

[109] Ghosh, A., Subrahmanyam, K.S., Krishna, K.S., Datta, S., Govindaraj, A., Pati, S.K., et al. (2008) 'Uptake of H2 and CO2 by graphene', Journal of Physical Chemistry C, 112, pp. 15704-7.

[110] Elias, D.C., Nair, R.R., Mohiuddin, T.M.G., Morozov, S.V., Blake, P., Halsall, M.P., et al. (2009) 'Control of Graphene's Properties by Reversible Hydrogenation: Evidence for Graphane', Science, 323, pp. 610-3.

[111] Lin, Y., Ding, F., & Yakobson, B.I. (2008) 'Hydrogen storage by spillover on graphene as a phase nucleation process', Physical Review B, 78, pp. 2-5.

[112] Sofo, J.O., Chaudhari, A.S., & Barber, G.D. (2007) 'Graphane: A two-dimensional hydrocarbon', Physical Review B, 75, pp. 1-4.

[113] Ataca, C., Akturk, E., Ciraci, S., & Ustunel, H. (2008) 'High-capacity hydrogen storage by metallized graphene', Applied Physics Letters, 93, 043123.

[114] Ao, Z.M., Jiang, Q., Zhang, R.Q., Tan, T.T., & Li, S. (2009) 'Al doped graphene: A promising material for hydrogen storage at room temperature', Journal of Applied Physics, 105, 074307.

[115] Ao, Z.M., & Peeters, F.M. (2010) 'High-capacity hydrogen storage in Al-adsorbed graphene', Physical Review B, 81, 205406.

[116] Peng, Y., Krungleviciute, V., Eryazici, I., Hupp, J.T., Farha, O.K., & Yildirim, T. (2013) 'Methane storage in metal-organic frameworks: current records, surprise findings, and challenges', J Am Chem Soc, 135(32), pp. 11887-94.

[117] Gross, K.J. (2007) 'The PCTPro-2000–The Ultimate Tool for Gas Sorption Analysis', Material Matters, 2, pp. 26–28.

[118] SETARAM Instrumentation (October 2017) 'PCTPRO-2000', link.

[119] Cabria, I., López, M.J., & Alonso, J.A. (2005) 'J. Chem. Phys.', 123, 204721.

[120] Costanzo, F., Silvestrelli, P.L., & Ancilotto, F. (2012) 'J. Chem. Theory Comput.', 8, 1288.

[121] Mauron, P., Buchter, F., Friedrichs, O., Remhof, A., Bielmann, M., Zwicky, C.N., & Züttel, A. (2008) 'J. Phys. Chem. B', 112, 906.

[122] Faye, O., & Szpunar, J.A. (2018) 'J. Phys. Chem. C', 122, 28506.

[123] Gillan, M.J. (1987) 'Quantum-classical crossover of the transition rate in the damped double well', J. Phys. C: Solid State Phys., 20, pp. 3621–3641.

[124] Mills, G., Schenter, G.K., Makarov, D.E., & J´onsson, H. (1997) 'Generalized path integral based quantum transition state theory', Chem. Phys. Lett., 278, pp. 91–96.

[125] Kundalwal, S.I., Meguid, S.A., & Weng, G.J. 'Strain gradient induced polarization in graphene', page 5,7and8.

[126] Blechta, V. 'Study of Graphene's Properties and its Sensor Applications', Study subject: Physical Chemistry, Supervisor: Kalbac, M., J. Heyrovsky Institute of Physical Chemistry, Academy of Sciences of the Czech Republic, Prague, page 12.

[127] Kang, D.-H., Sun, H., Luo, M., Lu, K., Chen, M., Kim, Y., Jung, Y., Gao, X., Parluhutan, S.J., Ge, J., Koh, S.W., Giovanni, D., Sum, T.C., Wang, Q.J., Li, H., & Nam, D. 'Pseudo-magnetic field-induced slow carrier dynamics in periodically strained graphene', page 3.

[128] Mahamiya, V., Shukla, A., Garg, N., & Chakraborty, B. 'Influence of compressive strain on the hydrogen storage capabilities of graphene: A density functional theory study', page 10.

[129] Han, E., Fang, W., Stamatakis, M., Richardson, J.O., & Chen, J. 'Quantum Tunnelling Driven H2 Formation on Graphene', pages S7-S9.

[130] Guinea, F., Katsnelson, M.I. and Vozmediano, M.A.H., 2008. Midgap states and charge inhomogeneities in corrugated graphene. Physical Review B, 77(7), p.075422.

[131]http://en.wikipedia.org/wiki/Energy_density
[132]http://www.elizabethqueenseaswann.com/Boat_Development_Specifications/Liquid_Hydrogen_Cylinders_Mass_Storage_Ships_Hull_Calculations4000Nautical_Miles_Range.html